UNIVERSITÀ
DI PARMA

UNIVERSITA' DEGLI STUDI DI PARMA

DOTTORATO DI RICERCA IN SCIENZA E TECNOLOGIA DEI MATERIALI

CICLO XXXVIII°

Engineering supramolecular surfaces: multiple H-bonding for toughness enhancement in carbon fiber composites and functionalized receptors for multivalent nanoparticles

Coordinatore:
Prof. Mauro Riccò

Tutore:
Prof. Enrico Dalcanale

Dottoranda: Monica Milani

Anni Accademici 2022/2023 – 2024/2025

Ai miei genitori Enrica e Mario,

Ai miei nonni Francesca e Luigino.

«Nulla si crea, nulla si distrugge, tutto si trasforma»

Antoine-Laurent de Lavoisier

Ente finanziatore: progetto finanziato dall'Unione Europea - NextGenerationEU – Piano Nazionale Ripresa e Resilienza (PNRR) - Missione 4 Componente 2 Investimento 3.3 "Introduzione di dottorati innovativi che rispondono ai fabbisogni di innovazione delle imprese e promuovono l'assunzione dei ricercatori dalle imprese" – Avviso N. 352 del 09/04/2022 del Ministero dell'Università e della Ricerca;

Funder: Project funded under the National Recovery and Resilience Plan (NRRP), Mission 4 Component 2 Investment 3.3 - Call for tender No. 352 of 09/04/2022 of Italian Ministry of University and Research funded by the European Union – NextGenerationEU

This work was supported by the National Recovery and Resilience Plan (NRRP), Mission 4 Component 2 Investment 3.3 - Call for tender No. 352 of 09/04/2022 of Italian Ministry of University and Research funded by the European Union – NextGenerationEU

Table of contents

Chapter 1. "Supramolecular topological adhesion boosts delamination resistance in carbon fiber reinforced polymers"

Chapter 2. "Synthesis and characterisation of a novel guanidinium functionalized cavitand"

Chapter 3. "Synthesis of functionalized sulfopillar[6]arene for grafting on silica nanoparticles"

Abstract

The research presented in the following thesis focuses on the precise functionalization of interfaces leveraging non-covalent interaction with applications spanning from enhancing the toughness of carbon fiber reinforced materials to recognition of specific molecular targets like anionic surfactants or histones methylated residues.

In the first chapter, supramolecular topological adhesion is presented as an innovative and effective methodology to enhance interlaminar fracture toughness in carbon fiber reinforced polymers (CFRPs). Delamination resistance is improved by physically entangling phenoxy resins within an epoxy matrix and introducing sacrificial H-bond interactions via ODIN (1-(7-Oxo-7,8-Dihydro-1,8-Naphthyridin-2-yl)urea) units. The ODIN units form sextuple H-bonding dimers in the cured epoxy matrix among plies, experimentally quantified via UV-Vis spectroscopy, whose detachment hinders crack propagation. The viability of this approach was tested using various phenoxy resins with different molecular weights and with different levels of ODIN functionalization. Delamination resistance was determined through double cantilever beam (DCB) and end-notched flexure (ENF) tests, showing up to 120% and 80% increases in Mode I and Mode II fracture toughness, respectively. The limited DCB and ENF test increments observed for control adherent PKHB-PU 23% functionalized with phenylurea (PU) groups, demonstrates that the strength of topological H-bonding is pivotal to boost delamination resistance. The results indicate that this method holds great potential for improving the durability of CFRP composites, especially in applications requiring high resistance to delamination.

In Chapter 2 the design and synthesis of two novel guanidinium quinoxaline cavitand is presented. In the first compound **GUAQxCav** the guanidinium group is separated from the electron-rich cavity of the cavitand through a methylene group spacer, while in the second one **GUA2QxCav** the

guanidinium group is directly attached to one quinoxaline wall. These architectures are expected to surpass the inherent limitation of conventional anion binding by offering a powerful synergy of interaction. Specifically, the guanidinium group, which is stable across a broad pH range, is expected to provide ionic interaction with the carboxylate group. Simultaneously the π-rich and hydrophobic cavity is suitable for binding apolar surfactant's alkyl chain by stabilizing C-H···π interactions. The investigation on the binding abilities of these two cavitands are under investigation in our research laboratory.

Lastly, the research activities described in Chapter 3 were carried out as part of an international EU research project titled "ENRICH: Molecular receptors enrich methylated and acetylated peptides for ultra-sensitive proteomics to explore the hidden modified proteome in disease". Part of the work has been carried out at University of Victoria, under the supervision of prof. Fraser Hof. This chapter discusses the synthetic strategies for the synthesis of a novel sulfopillar[6]arene specifically functionalized for covalent grafting onto silica nanoparticles (SiNPs), which are specifically designed for the recognition of methylated lysine and arginine residues of histone proteins. Two distinct synthetic approaches were explored: one designed to prepare the final molecule for covalent bonding via hydrosilylation, and the other for thiourea bond formation. The thiourea approach has been implemented to overcome the problems encountered with the synthesis of sulfopillar[6]arene with terminal double bond reactive group. that prevented the isolation of the desired product and is currently under investigation in our research lab. This synthetic strategy involved the introduction of a nitro aromatic group onto the macrocycle via a Suzuki coupling reaction. Subsequently, following a de-ethoxylation and sulfation sequence, this nitro group can be reduced to an amino group. This resulting amino moiety is then available for a conjugation reaction with a functionalized SiNP bearing a thioisocyanate functional group. This synthetic strategy is currently under study in our lab.

Chapter 1

"Supramolecular topological adhesion boosts delamination resistance in carbon fiber reinforced polymers"*

*The content of this chapter has been submitted for publication to Advanced Composite and Hybrid Materials. (https://doi.org/10.1007/s42114-025-01569-7)

1. Introduction

Laminate composites are multilayer materials where each layer is composed by fibers oriented unidirectionally or stitched in matt structures. Among fiber-reinforced composites, carbon fiber reinforced polymers (CFRPs) have become the material of choice for advanced structural applications requiring superior mechanical performance and reduced weight. Their widespread adoption in aerospace, automotive, wind energy, and high-performance sporting goods is primarily attributed to their high specific strength and stiffness, excellent fatigue resistance, and inherent corrosion resistance[1]. CFRP laminates are commonly fabricated by stacking prepregs—carbon fiber sheets pre-impregnated with thermosetting matrices, typically epoxy resins—to produce tailored, anisotropic structures optimized for specific loading conditions[2]. Delamination is a predominant failure mode in CFRP laminate materials, characterized by the separation of layers (plies) due to weak interfacial bonding[3]. This loss of cohesion significantly degrades the mechanical properties of the composite, compromising both its load-bearing capacity and service life. Delamination can be initiated by factors such as manufacturing defects, geometric discontinuities (e.g., edges, corners, holes, and notches), and impact damage. It is particularly critical in complex structures like aircraft skin-stringer assemblies and tapered components. Delamination is indeed the most common failure mechanism in laminated composites[4], especially under impact or out-of-plane loading conditions.

Several approaches have been implemented to improve interlaminar fracture toughness in CFRPs: (i) matrix toughening with rubber[5], fibers[6] of nanofillers like carbon nanotubes[7,8]; (ii) interleaving, placing thermoplastic films or fiber mats at interfaces between neighboring[9] plies; (iii) Z-pinning by inserting pins perpendicular to the laminate plane[10] or stitching fibers[11] through the laminate

thickness; (iv) surface treatments of carbon fibers like fiber sizing and plasma treatment[12]; (v) optimized ply stacking sequence[13]; (vi) resin modification with reactive toughenners or hyperbranched polymers[14]. The interleaving approach has been also implemented using H-bonded supramolecular polymers as interleave additives, leading to increased interlaminar fracture toughness and partial self-healing capabilities[15].

Nevertheless, most of these strategies rely on the introduction of additional interfaces or heterogeneous interleaves between adjacent plies, which can themselves act as preferential sites for delamination or stress concentration, thus underscoring the need for an approach that enhances interlaminar adhesion without creating new interfacial discontinuities.

Topological adhesion is a potential alternative to these approaches, already employed to enhance interfacial adhesion between hydrogels[16].In this context, topological adhesion refers to linking two polymer networks, called adherends, through a third polymer, named stitch polymer. The latter diffuses into the two adherends and crosslinks into a third polymer network in situ, in topological entanglement with the adherends networks. As a result, the third polymer network joins the other two networks together like a molecular suture. However, the presence of extensive covalent crosslinking among plies has an adverse effect on the interlaminar toughness. In polymeric materials, the introduction of multiple H-bonding crosslinking can reverse this trend by boosting toughness without sacrificing mechanical strength[17]. In the specific case of CFRP, this effect should lead to an interlaminar fracture toughness increase, since the elastic modulus is governed by the carbon fiber component. Differently, physical entanglement refers to the intertwining or interlocking of polymer chains through physical interactions, without the formation of covalent networks.

Here we report an innovative method to enhance interlaminar fracture toughness in CFRPs based on supramolecular topological adhesion. The proposed approach combines the physical entanglement of phenoxy resins within the CFRP epoxy matrix with sacrificial H-bond interactions among ODIN (acronym for 1-(7-Oxo-7,8-DIhydro-1,8-Naphthyridin-2-yl)urea) units, introduced as lateral substituents in the phenoxy resin. The overall effect of this supramolecular topological entanglement among plies (Figure 1) is the amplification of interfacial toughness, leading to enhanced delamination resistance.

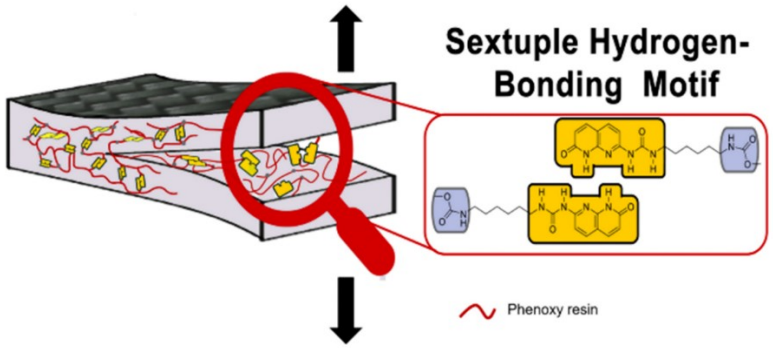

Figure 1. Sketch of the proposed supramolecular topological adhesion operation.

Phenoxy resins are commercially available amorphous thermoplastic polymers with molecular weight in the range 10.000-100.000 g/mol, miscible with epoxy resins. The pendant secondary hydroxyl groups in phenoxy resins are amenable to a variety of functionalizations. Due to their excellent mechanical properties including flexibility, toughness, adhesive and cohesive strength, as well as chemical and heat resistance, phenoxy resins are widely employed in composites and adhesives[18]. We recently introduced ODIN as sextuple H-bonding array motif, capable of self-dimerizing both in solution and in a polymeric matrix[19]. ODIN features a high self-dimerization constant measured in solution (K_{dim} = 4•10^4 M^{-1}) and a remarkable thermal stability[19]. Another

relevant property of ODIN is the different fluorescence[20] and UV-Vis[21] signature of the monomer and the dimer, allowing to quantify the dimer/monomer ratio in a polymer matrix. To be grafted on polymers ODIN is typically functionalized with an isocyanate group, which is also reactive toward the hydroxyl groups present on the phenoxy resins.

For this study, we selected a CFRP that has wide application in the automotive sector, due to its valuable mechanical properties, in terms of compression strength and for the possibility of being processed at different temperatures.

2. Methodology

2.1 Material preparation

The material chosen for the present work is a commercial prepreg, realized by CIT Toray company, C384 T700 12 K 2X2T ER450 40% Hot melt. This material is characterized by an aerial weight of dry fiber of 384 g/m2 and it is realized with a Toray T700 fiber (high strength fiber with fiber tensile modulus E= 230 GPa and strength σ = 4.9 GPa.). The resin is ER-450 and it is a toughened epoxy matrix, that can be cured in a variety of conditions, from 80°C up to 180°C. It is characterized by a maximum glass transition temperature of 210°C. After a cure cycle of 2 h at 135°C it exhibits a Tg of 160°C. This material is widely used in racing and automotive sectors. It is characterized by high mechanical properties in compression loading, while its interlaminar properties are less pronounced.

2.2 Single Lap Shear (SLS) test procedure

Preparation of tests specimens for lap shear tests according to ASTMD 5868. Two CFRP panels (150 × 200 mm) were laminated with 8 plies each and the adhesives were deposited on the surface of one plate in a section of 200 mm x 30 mm to cover the overlap length (25.4 mm for the standard used).

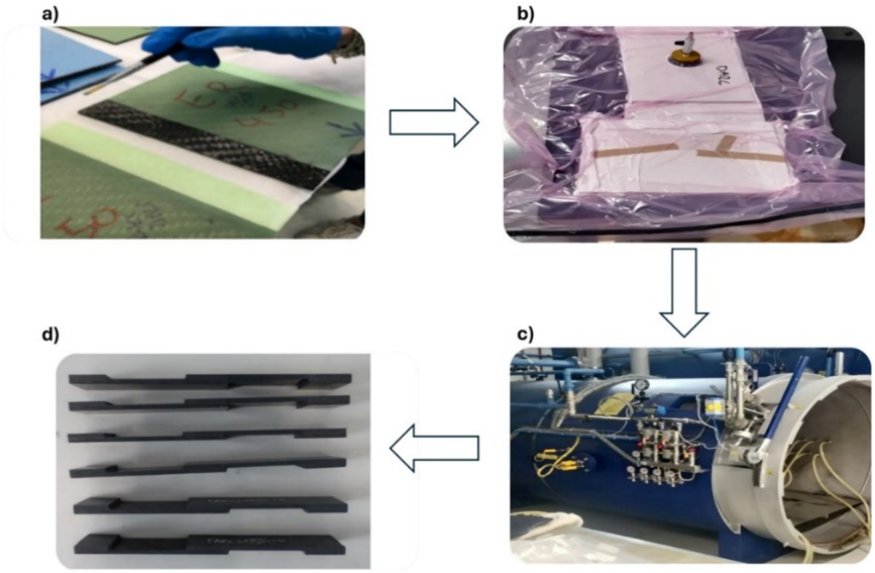

Figure 2. Process of preparation of lap shear specimens: a) application of the adhesives on the selected area of the ply, b) joint panels were placed in a vacuum bag, c) autoclave used for the curing cycle and d) lap shear specimens obtained.

The adhesive was dissolved in a mixture of chloroform and hexafluoroisopropanol (ratio 9:1, 2 mL per specimen, 250 mg of adhesive) and added with a brush (Figure 2a). After waiting 24 h to ensure solvent evaporation, the panel was laminated and cured in autoclave for 90 min 135°C, 6 bars (Figure 2b,c). After the curing phase, 6 specimens of dimension 175 mm x 25 mm x 3 mm were obtained using a robot with waterjet cutting (Figure 2d).

Lap shear tests. Lap shear tests were performed with an electromechanical testing machine MTS Insight 150 kN, with 250 kN hydraulic grips. The position of the transducer LVDT is 300 mm, with a resolution of 0.001 mm. The tensile tester is equipped with a load cell of 150 kN, with a resolution of 0.002 kN class 0.5. The test speed is: 2 mm/min.

2.3 Delamination tests

DCB specimens were prepared similarly to the SLS specimens with the only difference that the panels are totally superimposed (Figure 26A). The specimens have the following final dimensions: 150 mm total length, 25 mm width, 26 mm crack length, and were tested under a 3.0 mm/min crosshead separation rate (Figure 26B). Aluminum blocks were fixed with epoxy resin glue on the tip for the application of the load (Figure 27A). The amount of adhesive applied on the uncured plies on a joint area of 250 mm x 250 mm is 2,60 g dissolved in 30 mL of a solution of chloroform and hexafluoroisopropanol 9:1 (Figure 2a). After 24 hrs, the samples underwent a vacuum bag phase before being cured in autoclave for 90 minutes at 135 °C and 6 bars of pressure (Figure 2b,c). The specimens were obtained by cutting out the CFRP panel using a robot equipped with waterjet cutting. DCB and ENF samples were realized from the same panel. This allows us to guarantee the same functionalization and ensure higher reproducibility and conditions consistency.

ENF specimens have the following dimensions: 180 mm total length, 25 mm width, 55 mm crack length, and were tested under a 1.0 mm/min crosshead separation rate. ENF tests were carried out with 100 mm span between supports, and the specimen placed in the 3-point bending geometry as follows: 55 mm specimen half-span and 30 mm delamination length (Figure 26A, Figure 26B, Figure 27B and Figure 29).

The energy for unit length G_I was evaluated considering a crack length range of 48-80 mm for DCB, while for ENF tests, once the cracks propagate the test is concluded. The peak in the force/displacement diagram is considered representative of the above-described event. A further evaluation of the results was also realized considering the initial displacement measured by the Digital Image Correlation (DIC) camera. The experimental set up for both tests are shown in Figures S19 and S20 respectively.

The G_I that is necessary for creep propagation is calculated with the *Modified Beam Theory (MBT) Method* (ASTM D5528-13) according to equation (1):

$$G_I = \frac{3P\delta}{2B(\alpha + |\Delta|)}\left[\frac{N}{mm}\right] \quad (1)$$

where P is the applied load, δ is the displacement, B is the specimen width, a refers to the crack length and Δ is an empirical constant. A ZEISS ARAMIS 3D Camera was used to monitor the crack propagation (Figure S19 right).

Similarly, in ENF tests, G_{II} is calculated following the standard D7905/D7905M considering P as the applied load, B is the specimen width, a is the crack length and m is the compliance constant, corresponding to the slope of the regression curve calculated with the compliance calibration test, according to equation (2):

$$G_{II} = \frac{P^2}{2b} \cdot \frac{dC}{da} = \frac{3mP^2a^2}{2B}\left[\frac{N}{mm}\right] \quad (2)$$

The compliance calibration test is performed measuring the compliance of the specimen at 20 cm and 40 cm from the initial crack length. The displacement of the two adherend is monitored with ZEISS ARAMIS 3D Camera.

Results and discussion

3.1 Synthesis of the model compound 1

A model reaction between ODIN isocyanate and isopropanol was performed with the aim of setting the best reaction conditions for ODIN grafting on phenoxy resins (Scheme 3). Isopropanol was chosen as the simplest reagent to mimic the reactivity of the secondary alcohols of the phenoxy resins. The reaction was performed in DMSO to dissolve ODIN-isocyanate (**Error! Reference source not found.**), using a large excess of isopropanol to mimic the large number of secondary OHs of the phenoxy resins. DABCO (1,4-

diazabicyclo[2.2.2]octane) was added to catalyse the reaction that was kept at 70°C overnight. The reaction mixture was then cooled at room temperature and the final product was obtained in quantitative yield by precipitation with water, followed by repeated washing of the precipitate with water to remove traces of DMSO and DABCO. ODIN dimerization is suppressed in good hydrogen-bond acceptor solvents like DMSO[19]. ODIN shows two main tautomeric conformers when dissolved in DMSO-d6, as reported by Loos and coworkers[19,22]. The keto conformer **1a** is the dominant one, forming a six-membered-ring with intramolecular N-H···N H-bonding in accordance with Etter's rule[23] (Figure 11 and Figure 3, blue dots). This monomer is formed by first breaking the intermolecular hydrogen bond of the ODIN dimer and the π-π stacking and the weak intermolecular C-H···O=C hydrogen bond that permits the rotation to form a stronger N-H···N bond. The second observed conformer **1b** in DMSO-d_6 is the keto monomer without intramolecular H-bonding (Figure 10 and Figure 3 , orange dots).

3.2 General procedure for the functionalization of phenoxy resin PKHB with ODIN and PU.

Three different grades of commercial phenoxy resins having increasing Mw were selected: PKHA (Mw = 25000), PKHB (Mw = 32000) and PKHP (Mw = 52000). As shown in the lap-shear test section, PKHB is the best performing resin in terms of physical entanglement, therefore we focused on PKHB as polymer matrix for ODIN functionalization. To distinguish the influence of ODIN dimerization from the traditional hydrogen bonding network, PKHB was also functionalized using phenylureidohexyl isocyanate (PU). The corresponding PKHB-PU polymer features phenylurea dangling groups capable of standard H-bonding in the matrix.

Reaction of ODIN-isocyanate with PKHB using the conditions applied for the synthesis of 1 lead to the partial functionalization of the secondary OH groups

of the polymer (Scheme 1). Methyl ethyl ketone (MEK) is added as cosolvent to increase PKHB solubility. Two different grades of PKHB-ODIN are obtained by varying the amount of ODIN-isocyanate added: PKHB-ODIN 8% and PKHB-ODIN 13%. The degree of functionalization of the two polymers was experimentally determined by elemental analysis since nitrogen is introduced exclusively with the ODIN units (Table 3). The formation of the urethane bond leads to the appearance of a broad triplet at 7.34 ppm, (**F** signal, Figure 3 and Scheme 4) corresponding to the N-H signal of the urethane and a multiplet for the methine group of functionalized phenoxy resin at 5.19 ppm (I signal, Figure 3). The unreacted OH signal of PKHB is visible as doublet at 5.34 ppm (**M** signal, Figure 3), while the methyne groups of the unreacted phenoxy resin resonate at 4.1 ppm (**L** signal, Figure 3). The ATR FTIR spectrum of PHKB-ODIN samples shows a peak at 1710 cm^{-1} related to the stretching of the carbamate carbonyl (Figure 13). In solution, the polymer grafted ODIN assumes the same two conformations already observed in model compound **1**, as shown by the blue and orange ^{1}H NMR signal attribution in Figure 3. The relative ratio of the two ODIN conformers grafted to the polymer is 7:1 in favor of the blue conformer.

For a proper comparison of the effect of ODIN multiple H-bonding dimerization pattern on the supramolecular topological entanglement, PKHB was derivatized with phenylureidohexylcarbamate groups (PU), capable of forming bifurcated H-bonds between the carbonyl acceptor of one urea unit and the two NH donors of another one (Scheme 1b). The functionalization conditions are the same as PKHB-ODIN, using phenylureidohexyl isocyanate as reactant (Scheme 4). In the case of PKHB-PU the percentage of functionalization of the phenoxy resin is higher (23% for PKHB-PU vs 13% for PKHB-ODIN). Also in this case, the amount of functionalization is quantified via nitrogen EA (see Supporting information for complete characterization).

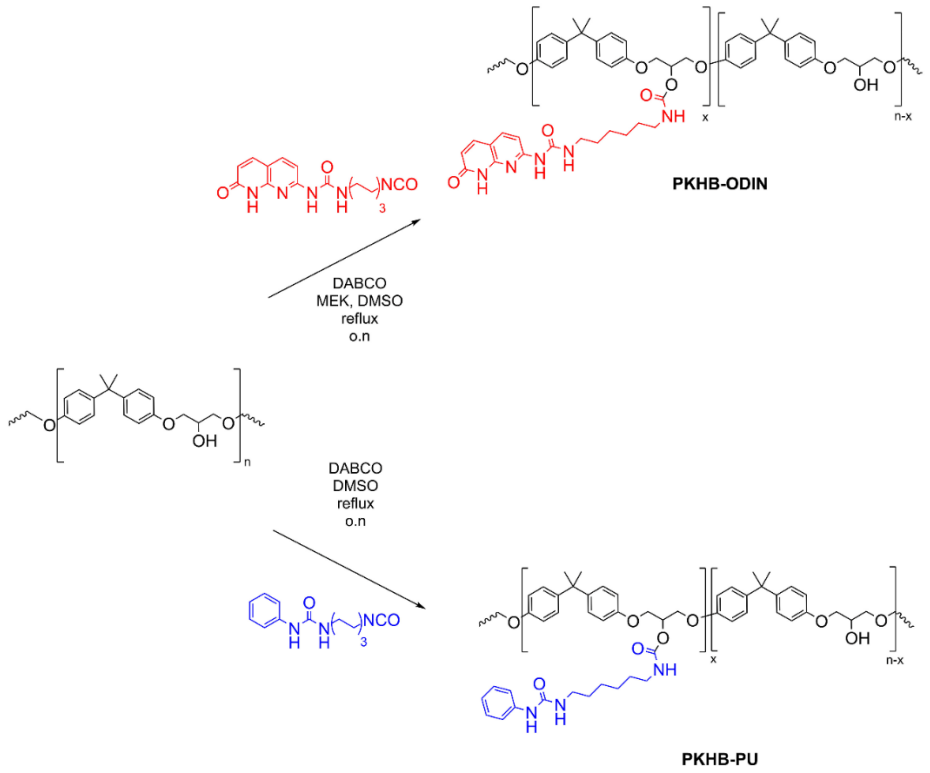

Scheme 1. a) functionalization of PKHB with ODIN-isocyanate (0.08<x<0.13); b) functionalization of PKHB with phenylureidohexyl isocyanate (x = 0.23).

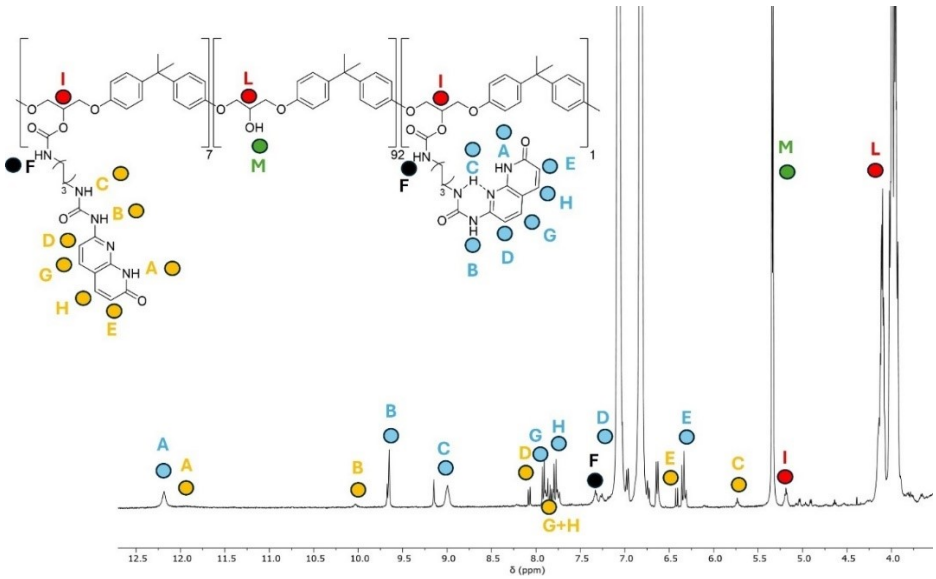

Figure 3. Selected portion of the ^{1}H NMR (DMSO-d_6, 298K, 600 MHz) of PKHB-ODIN 8%.

3.3 Viscoelastic properties of PKHB-ODIN and PKHB-PU

Viscoelastic properties of PKHB-ODIN and PKHB-PU were studied by means of dynamic mechanical thermal analysis (DMTA). Pristine PKHB exhibits its main relaxation, with T_α at 92°C, close to its glass transition (T_g) measured at 86°C by differential scanning calorimetry (DSC, Figure 15). The presence of H-bonding moieties causes an increase in the relaxation temperature, dependent on the crosslinking density. Indeed, T_α is shifted to 101°C for PKHB-ODIN 8% and 108°C for PKHB-ODIN 13%, while for PKHB-PU 23% it is further increased to 115°C (Figure 4). These temperatures agree with T_g measured via DSC at 105, 106 and 111°C for PKHB-ODIN 8%, PKHB-ODIN 13% and PKHB-PU 23%, respectively (Figure 6). For all materials, no stable plateau is observed above the glass transition, as there is no covalent crosslinking. Instead, the storage

modulus plots slowly decrease with increasing temperature, reflecting the weakening of H-bonding between polymer chains (Figure 4). The decay rate of the storage modulus is lower for PKHB-ODIN compared to PKHB-PU and pristine PKHB, reflecting the higher binding energy associated to the sextuple H-bonding.

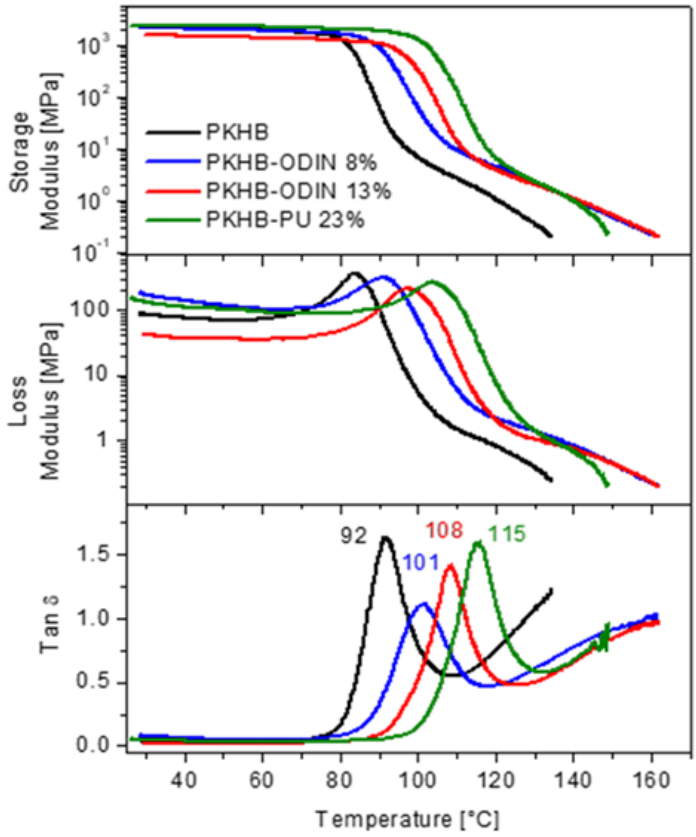

Figure 4. DMTA plots (storage modulus, loss modulus and tanδ) for PKHB and ODIN/PU functionalized counterparts.

The viscoelastic properties of PKHB-ODIN were further investigated as described in the Supporting Info. Above their glass transition, PKHB-ODIN exhibit fast relaxation kinetics (Figure 16), with limited differences as a function

of ODIN %, reflecting the shift in Tα. The response over longer time across the range of the glass transition temperature was studied by creep tests at 100°C under a low stress (100 kPa) to confirm that higher ODIN grafting decreases the rate of creep relaxation (Figure 17a). Non-isothermal creep tests were also carried out, to evaluate the temperature at which the mechanical relaxation becomes apparent under static conditions (Figure 17b). Under these testing conditions a moderate shrinking was observed for both PKHB-ODIN formulations above their glass transitions, reflecting the memory shape effect typical of weakly crosslinked polymer systems. With increasing temperature, the elongation of the specimen under the static load dominates, suggesting that the equilibrium of ODIN dimers is rapidly shifted towards the dissociated form in the temperature range above 100°C.

3.4 Single Lap Shear (SLS) tests

For this study we selected a CFRP that has valuable mechanical properties in terms of compression strength, but whose interlaminar properties are characterized by not very high values. See Methodology Section and Supporting Info for details.

Preliminary adhesion tests according to the single lap shear (SLS) configuration were conducted to evaluate the effect of physical and supramolecular topological entanglement on the adhesion between two plies. In detail, two CFRP panels of 150x200 mm area were laminated with 8 plies each and the adhesives were deposited on the surface of one plate in a section of 200x30 mm to cover the overlap length (25.4 mm for the used ASTM D5868 standard, see Methodology section for details) to realize single superposition joints. Chemical solution deposition was chosen to apply the adhesive on the ply surface. All pristine phenoxy resins and PKHB-PU are soluble in chloroform. Solubilization of PKHB-ODIN requires the presence of an H-bond donor cosolvent to break the sextuple H-bond dimerization crosslinking among polymer chains. We

selected hexafluoro-isopropanol as cosolvent since it has a boiling point close to that of chloroform (58°C vs. 61°C), so they evaporate almost simultaneously after deposition. Both functionalized and non-functionalized resins were dissolved in a 9:1 solution of chloroform and hexafluoro-isopropanol and applied manually by means of a brush on the 30 mm x 200 mm joint area of one of the two prepreg panel plies. The amount of adherent applied in each case is 15% w/w of the total amount of epoxy resin present per area of application. The solvent was left evaporating for one day at room temperature, after which the second panel overlapped in the joint area. The joint panels were placed in a vacuum bag to remove air and subjected to the standard curing cycle in autoclave (90 min, 135°C, 6 bar) (Figure 2c). From each panel, six single lap shear specimens were cut and five of them were tested. The adhesion properties of the bonded joints were investigated with single lap shear test configuration, following the ASTM D 5868 – 01 Standard Test Method for Lap Shear Adhesion for Fiber Reinforced Plastic (FRP) Bonding1 standard method. The single lap shear test consists in applying a displacement at fixed speed, resulting in increasing stress until the specimen, secured by two clamps, breaks. The shear strength τ is obtained by dividing the maximum load by the area of application of the specimen (Figure 18).

The results of SLS test on the three different molecular weight phenoxy resins are summarized in Table 1 (see Figure 19-23 for the SLS curves) and compared to the reference specimen without added adhesive. All the specimens tested showed a cohesive rupture (shown in Figure 24 for PKHB-ODIN 13%). Both PKHA and PKHB show a substantial improvement in SLS shear strength with respect to the reference, while PKHP produced a small decrease.

	Mw	SLS [MPa]	Standard deviation	Improvement
PKHA	25000	16.6	± 1.00	9.2%
PKHB	32000	17.2	± 1.00	13.2%
PKHP	52000	14.7	± 1.00	-3.4%
Reference	\	15.2	± 0.68	\

Table 1. SLS test results on three different molecular weight phenoxy resin, compared to the pristine standard (average value of 5 specimens for each sample).

The data reported in Table 1 indicates that the Mw of the phenoxy resin significantly affects physical entanglement. Accordingly, PKHB has the appropriate Mw to diffuse into the ply composite matrix. PKHB was therefore selected for ODIN functionalization. Six lap shear specimens were prepared for each grade of ODIN functionalized PKHB (8% and 13%) and for PKHB-PU 23%. Five of them were mechanically tested following the ASTM 5868 standard method and one kept for further analyses.

	SLS [MPa]	Standard Deviation	Improvement (Rif. Reference)	Improvement (Rif. PKHB)
Reference	15.2	± 0.68	\	\
PKHB	17.2	± 1.00	13.1%	\
PKHB-ODIN 8%	18.5	± 1.23	21.7%	7.5%
PKHB-ODIN 13%	18.3	± 1.04	20.4%	6.4%
PKHB-PU 23%	14.8	± 0.44	-2.6%	-13.9%

Table 2. SLS test results on PKHB at different levels of ODIN functionalization, compared to the pristine and to the PKHB specimens (average value of 5 specimens for each sample).

The results of SLS tests are reported in Table 2 (see Figure 5 and Figure 22-23). Figure 5 shows that the five specimens relative to PKHB-ODIN 13%, all tested at room temperature, are characterized by the same stiffness and the damage of the joint area starts around 15 MPa. The specimens show a small delamination (kinks in the curve), regaining the same stiffness until failure, that occurs at

around 18-20 MPa. This behaviour indicates that the interface, even if it starts to damage, is able to carry the applied load without modifying the overall mechanical properties (the slope of the stress-displacement curve is the same before and after delamination). The linear aspect of the stress-displacement curves indicates a fragile behaviour, thus the system under the applied load is not plastically deforming. The presence of ODIN leads to an average 7% increase in SLS with respect to pristine PKHB and to a 21% with respect to reference specimens. By comparison, the control material PKHB-PU 23% exhibits a 13.9% reduction, a clear indication that only multiple H-bonding systems have enough strength to improve SLS in CFRP. The SLS results for PKHB-ODIN 8% and 13% are comparable within the experimental error, indicating that the amount of ODIN in PKHB above 8% does not improve shear strength. We selected PKHB-ODIN 13% as the best candidate for specific delamination tests.

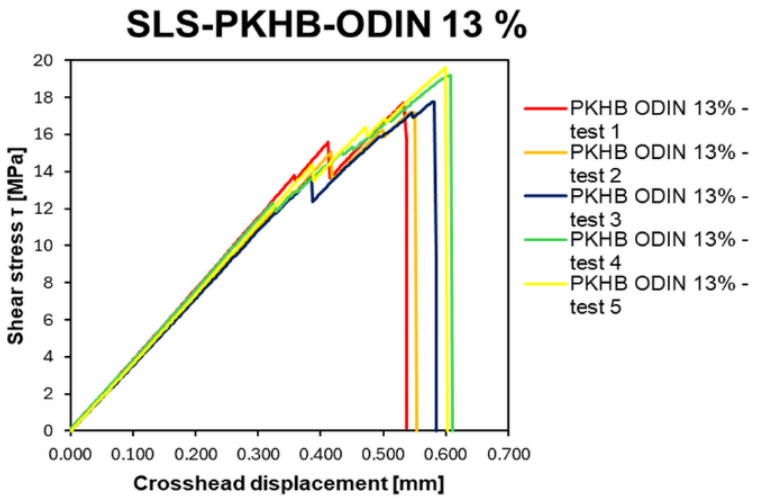

Figure 5. Load - displacement curves for five specimens jointed with PKHB-ODIN 13%.

3.5 Double Cantilever Beam (DCB) and End Notched Flexure (ENF) delamination tests

There are three different tests to evaluate delamination or interlaminar fracture toughness, based on the direction where the stress is applied to the material. Mode I of delamination is applied when stress is perpendicular to the crack propagation plane, that is tested according to Double Cantilever beam (DCB) configuration, Mode II when stress occurs parallel to this plane, tested according to End Notch Flexure (ENF), and Mode III when out of plane shear is applied (Figure 25). Considering standard composite component loading configurations, Mode I and Mode II fracture toughness tests are the most important to mimic the potential failure of the component due to peeling situations (Mode I) and interlaminar failure (Mode II). For this reason, Mode III loading configuration was not considered in the present study. DCB test is performed following the ASTM D5528-01 protocol (Standard Test Method for Mode I Interlaminar Fracture Toughness of Unidirectional Fiber-Reinforced Polymer Matrix Composites), the ENF test is applied following ASTM D7905/D7905M-19 (Standard Test Method for Determination of the Mode II Interlaminar Fracture Toughness of Unidirectional Fiber-Reinforced Polymer Matrix Composites) procedure (Figure 26-29). Samples were prepared by laminating two adherends made of 8 plies of CFRP, applying the solution with phenoxy resin PKHB with and without the specified above functionalization with the same % in weight of single lap shear configuration. As already explained for single lap shear specimens, the solvent was left evaporating for one day at room temperature, after which the second adherend was overlapped in the joint area. DCB and ENF samples present an initial artificial crack, with initial length a_0=25 mm and a_0=55mm respectively, that was realized thanks to a polyethylene release film with thickness t=0.15 mm (Figure 26). The joint panels were placed in a vacuum bag to remove air and subjected to the standard

curing cycle in autoclave (90 min, 135°C, 6 bar) (Figure 2). From each panel, four DCB and four ENF specimens were cut and tested. DCB samples are opened thanks to a specific fixture by applying a constant crosshead of the testing machine that tends to open the joint perpendicularly to the lamination phase. The crack propagation and evolution are measured via digital image correlation (DIC). ENF tests are performed loading the coupons on a three-point bending flexural configuration and observing the crack propagation. Different from what previously explained for DCB, in the case of Mode II testing, once the cracks propagate, a load drop is observed, and the test is concluded. In Mode II cracks propagate in a more sudden and uncontrolled way. Further details about the test realization are reported in the Methodology section. Also, for this test DIC was used to measure crack propagation.

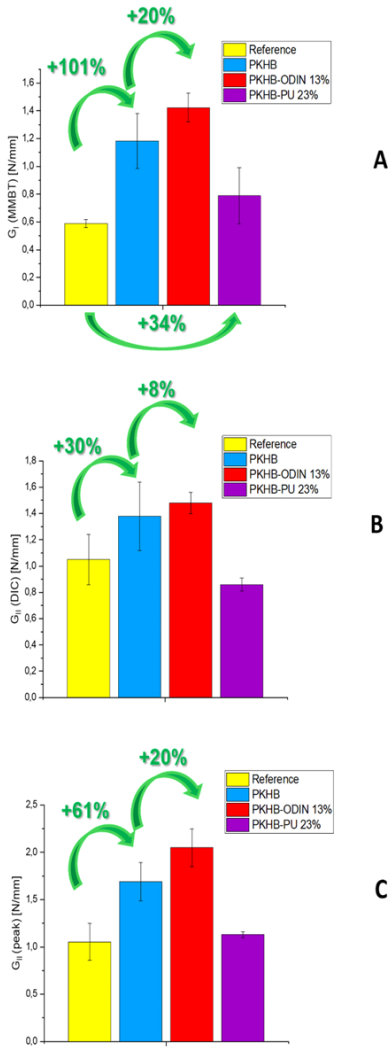

Figure 6. A) DCB G_I values for the reference material T700 C384 ER450 40% (yellow bar), the medium-molecular weight phenoxy resin PKHB (blue bar), PKHB-ODIN 13% (red bar) and PKHB-PU 23% (purple bar). B) ENF-DIC G_{II} values for the reference material, PKHB, PKHB-ODIN 13%, PKHB-PU 23% calculated from the initial point of delamination determined with DIC camera, C) ENF-PEAK G_{II} values for the reference material, PKHB, PKHB-ODIN 13%, PKHB-PU 23% calculated from the point of

delamination determined with a drop in the load curve determined by the testing machine.

The DCB and ENF procedures were applied to CFRP samples with the following adherends: phenoxy resin PKHB, PKHB-ODIN 13% and PKHB-PU 23%. The histograms of Figure 6 illustrate the results. All experimental data are reported in Figure 7, Figure 32-36 and Table 4 for DCB and Figure 8, Figure 37-38 and Table 5 for ENF. Considering the effect of the functionalization on the G_I measured values, the addition of PKHB alone results in an increment of G_I of more than 100% with respect to the reference sample[24], which increases to 120% (1.423 ± 0.185 N/mm, Table 4) using PKHB-ODIN 13% as adherent. By employing PKHB-PU 23% the G_I enhancement is reduced to 34% (Figure 5A). The observed trend can be explained as follows: the physical entanglement by PKHB is able to enhance significantly the energy required to propagate the crack in Mode I configuration and its effect is further amplified by the supramolecular topological entanglement given by ODIN dimerization within the epoxy matrix. The reduced increment observed for PKHB-PU 23% (Figure 5A) demonstrates that what is important is the strength of topological H-bonding rather than its number. Thus, the ODIN-functionalized phenoxy chains of PKHB connect the interfaces of the chosen CFRP materials realizing a network that reduces crack propagation both via physical entanglement and multiple H-bond cross-linking. As a crack propagates, the polymer chains at the crack front are stretched, transmit stress from the crack front into the bulk, and break the sacrificial ODIN H-bonds.

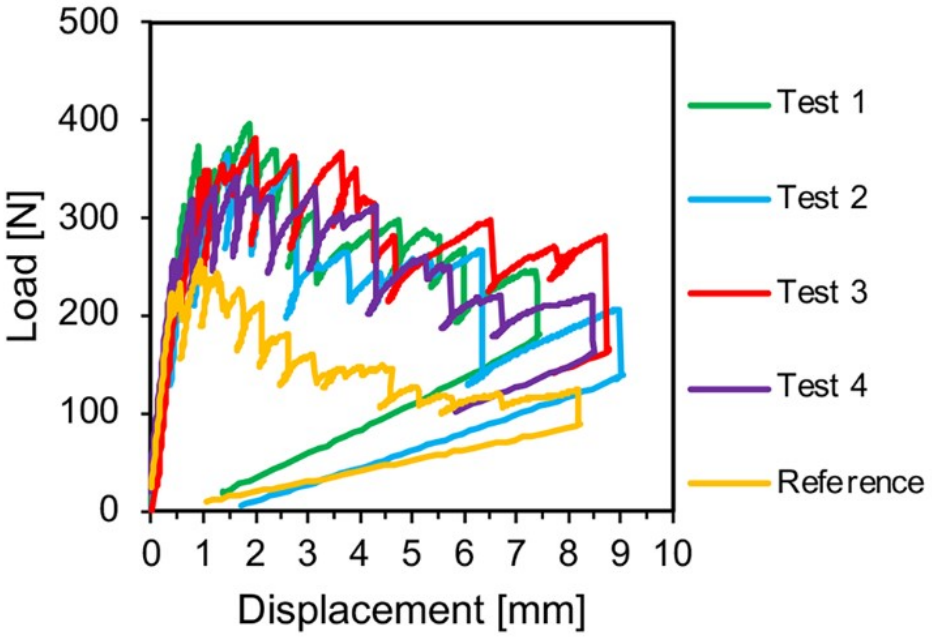

Figure 7. Load - displacement curves for PKHB-ODIN 13% specimens (colored lines) compared to average data of 4 reference specimens without any adhesive (yellow line).

The positive effect of both physical and topological entanglement is further confirmed by G_{II} energy calculated values via ENF test (Figure 8). The point of delamination in the ENF tests has been determined in two ways: initial displacement measured by the Digital Image Correlation (DIC) camera and the drop in the load curve determined by the electromechanical testing machine. The first set of data is the most conservative, while the second one gives a more realistic picture of the real behavior. Accordingly, the results reported in Figure 6B and 6C differ significantly, but in both cases the positive trend in delamination resistance is confirmed.

In detail, physical entanglement leads to a 30% G_{II} increase with DIC analysis compared to a 61% increase via load curve drop (2.05 ± 0.20 N/mm, Table 3). Topological entanglement adds a further 8% G_{II} improvement with DIC and leads to a remarkable 20% increment via load curve drop. Also in this case,

PKHB-PU 23% shows either a negative trend or a reduced increment, confirming the trend already observed in DCB tests.

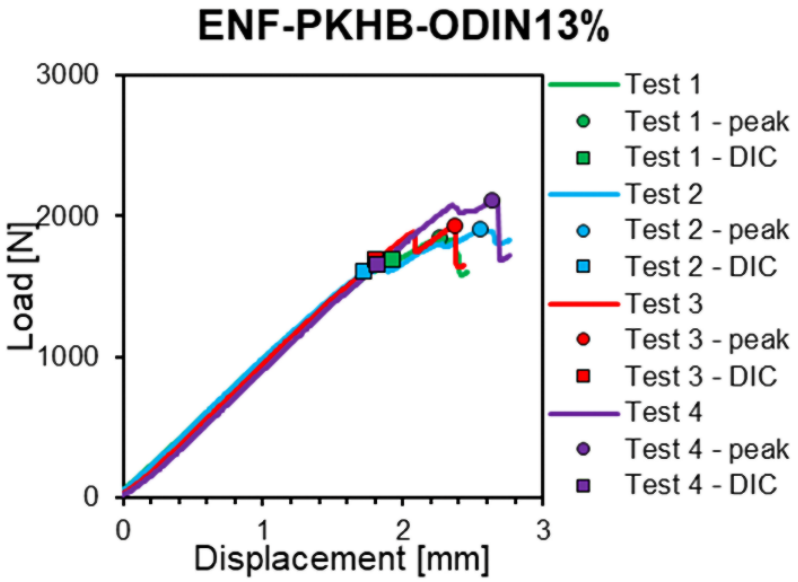

Figure 8. Resistance curves for PKHB-ODIN 13% specimens. The colored dots represent the point of crack propagation monitored by the MTS machine, while the colored circles represent the point of delamination determined by the DIC camera.

ENF results confirm the behavior observed with DCB tests, however the increments are smaller. The increment is less evident in this configuration because Mode II is a shear loading configuration in which the interfacial layers are expected to move the one with respect to the other, as it is reported in Figure 25. The crack propagation is quite rapid and, in this case, physical and topological entanglements that keep the two interfacial layers together are orthogonal to the shear plane and subjected as well to shear forces. Even if their presence changes the interface state, they are less efficient in postponing the crack development.

As shown by the error bars reported in Figure 6, dispersion in G_I and G_{II} data is not small. This is normal for these types of tests, since the crack propagation is a

phenomenon involving several plies interfaces and the calculation of the G_I and G_{II} values are affected by several sources of errors that are due to the parameters used (see equations in the Supporting Info).

The fracture surface of the propagation region in DCB and ENF specimens was evaluated by SEM. The morphologies of the DCB fracture surfaces of the reference composite compared to PKHB-ODIN 13% modified composite samples are illustrated in Figure 41. The reference material shows brittle failure with intact carbon fibers, while the PKHB-ODIN 13% modified composite exhibits a rougher surface, reflecting an increased fracture path and ductile failure of the matrix. The surface of the latter is mainly characterized by the matrix in which signs of crack propagation can be evidenced. Similar features are observed in the ENF specimens, as shown in Figure 42.

In the case of ENF-PKHB-ODIN 13%, the fracture surface shows multidirectional cracks with a less regular configuration since the loading direction is different and the crack propagation more instable.

4. Quantification of the ODIN dimer formation in PKHB-ODIN and in the epoxy matrix

The key issue of assessing the amount of ODIN present in the dimeric form in the CFRP matrix was addressed via UV-Vis measurements (see Supporting Info for methodology, Figure 39), given the different signature of the monomer and the dimer both in solution[21] and in polymeric matrices.[20]

The grade of ODIN dimerization in various polymeric matrices was evaluated on the basis of a thin film (thickness around 100-200 µm) UV-Vis absorption. The ratio between the two peaks at 340 and 360 nm changes with the degree of dimerization: the peaks have the same height when the molecule is only in his monomeric form, while the blue shifted peak is predominant when dimers are present.[21]

The ratio between the two peaks at 340 nm (A_1) and 360 nm (A_2) changes with the degree of dimerization: in DMSO solution ODIN is 100% monomer and the A_2/A_1 ratio is 1.01. On the other hand, ODIN is 100% dimer in $CHCl_3$ with a A_2/A_1 ratio of 0.61.[21] We estimated the monomer % either by using a linear combination of DMSO and $CHCl_3$ solution spectra to fit the ODIN spectra in various resins or by using the following formula (3):

$$\%(Monomer) = \frac{\frac{A_2}{A_1} - \frac{A_2^{CHCl_3}}{A_1^{CHCl_3}}}{\frac{A_2^{DMSO}}{A_1^{DMSO}} - \frac{A_2^{CHCl_3}}{A_1^{CHCl_3}}} \times 100 = \frac{\frac{A_2}{A_1} - 0.6}{0.41} \times 100 \qquad (3)$$

obtaining the same results. Applying both methods to the spectra reported in Figures 9 and S31, we calculated that the percentage of ODIN dimer in PKHB-ODIN 13% resin is ~35%, while in the PKHB-ODIN 13% dispersed (15% w/w) in the epoxy resin is ~15%.

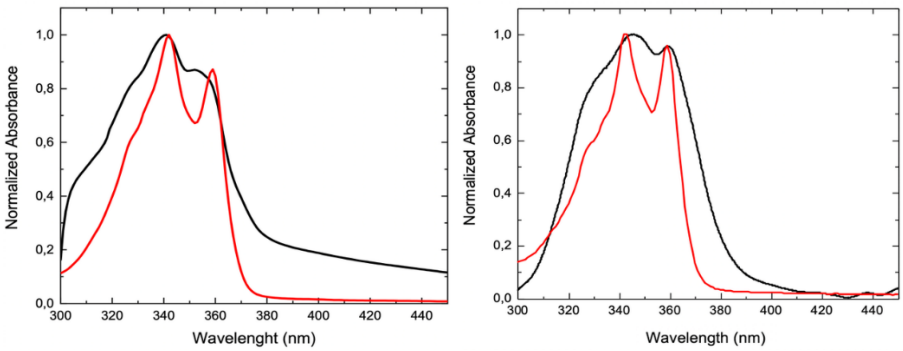

Figure 9. Absorption spectrum of solid PKHB-ODIN-13% (black line, left panel) and PKHB-ODIN-13% dispersed (15% w/w) in epoxy-resin (black line, right panel). The red lines are the respective linear combinations of monomer and dimer spectrum used to fit the experimental spectrum and extract the dimer percentage (See Supporting Info for more details).

We would like to emphasize the novelty and relevance of this analysis to experimentally prove and quantify the presence of H-bonding networks in

polymeric matrices. Extension of this methodology to other polymers is ongoing.

5. Conclusions

We present a new supramolecular approach to overcome the long-standing issue of low interlaminar adhesion in CFRPs. Supramolecular topological entanglement has proven to be a reliable route to boost interlaminar fracture toughness in CFRP composites via the combination of physical entanglement of PKHB phenoxy resin and topological network of sacrificial ODIN dimers. Two are the major factors responsible for the observed improvement in delamination resistance: (i) the Mw of the phenoxy resin for the physical entanglement, which affects the polymer chain diffusion in the uncured epoxy matrix of the plies; (ii) the amount of ODIN dimer in the cured epoxy matrix, which hinders crack propagation by rising energy dissipation. The two factors have been effectively coupled by functionalizing part of the secondary OHs of the phenoxy resin with ODIN units.

The positive effects of the PKHB-ODIN-13% application are larger for Mode I than Mode II loading configuration: an outstanding increase up to 120% in peeling resistance with respect to pristine material is measured by DCB, while a remarkable 80% improvement in interlaminar resistance is obtained in the ENF-peak mode. This difference can be explained as follows: the physical entanglement that affects the polymer chain diffusion in the epoxy matrix is much more efficient if the crack propagates perpendicularly to the PKHB chains, thus finding a physical obstacle difficult to overcome. In the case of Mode II configuration, interlaminar properties are enhanced, but once the crack finds a weak point, its propagation suddenly takes place.

Mechanical data and the result interpretation are further reinforced if DSC and DMA data are considered. The presence in PKHB of ODIN and PU dangling chains pushes T_g of the adhesive toward higher values, helping the interface in

responding in a more efficient way to the crack propagation, in analogy with previously reported correlation between T_g of the adhesive and joint resistance.[25] Considering DMA results, the decay rate of the storage modulus in temperature is lower for PKHB-ODIN compared to PKHB-PU and pristine PKHB, showing that the higher binding energy associated with the sextuple H-bonding is able to slow down the decay of mechanical properties acting as a source of toughening.

The DCB and ENF improvements due to the presence of ODIN roughly match with the ODIN dimer content in the epoxy matrix. Albeit a direct correlation cannot be proven, the presence of sacrificial multiple H-bonding motifs in the polymer matrix exerts a significant role in enhancing delamination resistance in CFRPs. This interpretation is substantiated by the control tests conducted on specimens featuring PKHB-PU 23% as adherent: the observed DCB and ENF results are significantly lower than those of PKHB-ODIN 13%, indicating that the mere presence of H-bonding does not automatically turn into an improvement of interlaminar fracture toughness.

The technological appeal of this innovative solution is very high as it can be used in critical areas where locally stronger delamination resistance is needed, without affecting the overall behavior of the material or increasing the weight of the final components. For example, this approach can be implemented for critical joints subjected to homologation tests for racing cars components.

Acknowledgements This work benefited from the equipment and framework of the COMP-HUB Initiative, funded by the Departments of Excellence program of the Italian Ministry for Education, University and Research (MIUR, 2023–2027). Centro Interdipartimentale di Misure “G. Casnati” of the University of Parma is acknowledged for the use of NMR and MS facilities. T. Martinoni and A. Angione are acknowledged for their support in mechanical tests carried out

at Dallara Automobili S.p.A. A. Slobodeniuc of Elantas Europe srl is acknowledged for acquiring SEM images.

Author contribution M.M.: Investigation, Visualization. S.D.: Investigation. F.B.: Investigation. A.B.: Investigation. A.L.: Methodology, Validation. A.F.: Investigation, Data curation, Methodology. A.P.: Data curation, Resources, Methodology. R.P.: Data curation, Project administration, Writing – review & editing. C.P.: Conceptualization, Supervision, Writing – review & editing. E.D.: Conceptualization, Supervision, Funding acquisition, Writing – review & editing. All authors reviewed the manuscript.

Funding This work was supported by the National Recovery and Resilience Plan (NRRP), Mission 04 Component 2 Investment 1.5 – NextGenerationEU, Call for tender n. 3277 dated 30/12/2021. Project title: Ecosystem for sustainable transition in Emilia-Romagna. Award Number: 0,001,052 dated 23/06/2022, within Spoke1 activities "Materials for sustainability and ecological transition" CUP D93C22000460001. E. D. and A. F. acknowledge the support of PNRR – M4C2 – I1.1 – PRIN 2022 REPRONET (2022TCJRCA). A. L. and A. B. acknowledge the support of IPHOQS "Integrated Infrastructure Initiative in Photonic and Quantum Sciences", (IR0000016, CUP B53C22001750006). M. M. thanks Dallara Automobili SpA for support of her scholarships.

6. Supporting information

6.1 Methods

6.1.1 General.

Nuclear magnetic resonance (NMR). NMR spectra were recorded on a Bruker Advance 400 (400 MHz). Chemical shifts are reported in parts per million (ppm). 1H-NMR chemical shifts are given in reference to the residual solvent peak (2.50 ppm for deuterated dimethyl sulfoxide (DMSO-d_6).

Infrared spectroscopy (IR). Infrared absorption spectroscopy analyses were performed with a Perkin Elmer FT-IR Spectrum Two instrument in the mode of Attenuated Total Reflectance (ATR) using powder samples. The background was subtracted from every spectrum recorded.

Elemental Analysis (EA). Elemental analyses were recorded on a CHNS Thermo Fisher FlashSmart. The nitrogen content was determined by means of thermal conductivity (TC) and volumetric analysis.

Differential scanning calorimetry (DSC): Test were carried out on a TA Instruments Q20 differential scanning calorimeter, using samples of ca. 7 mg into sealed aluminum pans, under nitrogen flow. The heating rate was 10°C/min between 25 °C and 200 °C, followed by cooling (10°C/min) and second heating with the same conditions. Glass transition temperature was determined as the midpoint of the transition on the second heating. Thermogravimetric analysis (TGA):Test were carried out on a TA Instruments TGA Discovery (Q5000) using about 10 mg samples, heated at 10°C/min between 50 °C and 800 °C, under air or nitrogen flow.

Compression molding. Before analysis, the received materials were dried in oven at 100°C under vacuum for at least an entire night prior to being molded for the analysis that required it. All samples

were molded between Teflon plates with an appropriate spacer. They were preheated for 3 minutes and hot pressed under 1 ton for another 3 minutes at 200°C for PKHB-ODIN and 150°C for PKHB-PU from compression-molded plates (Carver C12, laboratory press) unless otherwise specified. *Dynamic mechanical analysis (DMTA).* DMTA analyses were carried out on bars (7 x 1 mm^2 nominal cross-section, 30 mm length) cut from compression-molded plates, tested in tensile mode on a TA Instruments Q800. Tests were done on heating ramp (2°C/min) between room temperature and 170°C, at and 1 Hz frequency in strain-controlled mode, deformation amplitude at 0.05% and 0.01 N preload. The minimum load allowed (additional end-of test criterion) was set at 0.2 MPa, to prevent possible dripping. All samples were conditioned at 23°C and 50% of relative humidity for at least 48h before analyses. Main relaxation temperature (T_α), associated with the transition between glassy state and rubbery state, was taken at the maximum of tanδ plot.

Double Cantilever Beam (DCB) tests and End Notched Fracture (ENF) tests. DCB and ENF tests were performed with an electromechanical testing machine MTS Insight 150 kN, with 250 kN hydraulic grips. The position of the transducer LVDT is 300 mm, with a resolution of 0.001 mm. The tensile tester is equipped with a load cell of 150 kN, with a resolution of 0.002 kN class 0.5. A ZEISS ARAMIS 3D Camera was used to monitor the crack propagation.

UV-Vis absorption. UV-Vis absorption measurements were performed with two different experimental setups. The PerkinElmer Lambda650 double beam spectrophotometer was used to measure absorption spectra of PKHB-ODIN-13% sample and to measure the absorption spectra of ODIN in DMSO and CHCl3 solution. Absorbance measurements of PKHB-ODIN-13% dispersed (15% w/w) in epoxy-resin were performed using a customized spectrophotometric setup to precisely assess the spatial homogeneity of solid thin films. A wide-spectrum fiber lamp that combines deuterium and halogen

light sources (DH-2000-BAL, Ocean Insight) was used to illuminate the samples. The light from the fiber output was collected using a 20x microscope objective and focused to produce a beam diameter below 2 mm on the sample surface. The transmitted light was collected with a second 20x microscope objective and directed to the fiber input of an in-fiber spectrometer (Ocean Optics USB4000). The sample was mounted on an XY motorized linear translational stage with a spatial resolution below 100 μm to enable precise sampling of homogeneity. Each spectrum is the result of an average of 100 spectra collected from respectively the white lamp, the light transmitted by the sample, and the dark signal. The absorbance of the sample was then calculated using the following expression:

$$A = -log\frac{(I_t - I_b)}{(I_o - I_b)}$$

where I_t is the light transmitted through the sample, I_b is the background (dark) signal and I_o the incident intensity.

To account for the absorption contribution of the polymeric matrix, the absorbance of the bare resin was measured then subtracted from the sample after correcting for thickness variations.

SEM micrographs. SEM micrographs were acquired on a Thermo Scientific Phenom XL instrument equipped with Back Scattering Detector (BSD). The experimental settings are indicated in each figure.

6.1.2 Synthesis

Unless otherwise specified, chemicals and solvents were purchased from Sigma-Aldrich and used

as received. All solvents employed were laboratory grade and used as received.

Synthesis of *1-(6-Isocyanatohexyl)-3-(7-oxo-7,8-dihydro-1,8-naphthyridin-2-yl)urea* ODIN isocyanate

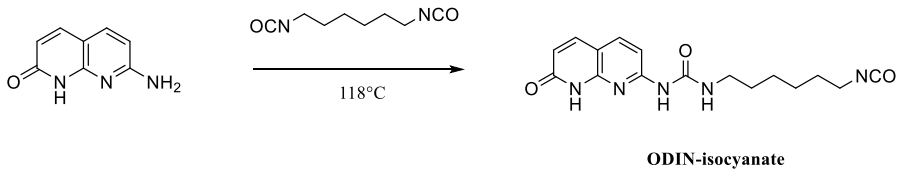

Scheme 2. preparation of ODIN-isocyanate.

Naphthyridine (50 g, 0.31 mol, 1 equiv) and hexamethylene diisocyanate (500 mL, 3.1 mol, 10 equiv) were combined and stirred. The resulting slurry was heated for 15 h at a temperature of 118 °C (temperature of oil bath). After cooling to room temperature, the solid was filtered over a Buchner funnel and washed with hexane and acetone until the wash was colorless. The solid residue was dried under vacuum at 60 °C, yielding the product as a tan powder with minor impurities (72.7 g, 71% yield).

^{1}H NMR (400 MHz, DMSO-d_6) δ: 12.18 (s, 1H, Ar–N*H*), 9.65 (s, 1H, Ar–N*H*–CO–NH), 8.99 (s, 1H, N*H*–CO–NH–Ar), 7.91 (d, *J* = 8.4 Hz, 1H), 7.78 (d, *J* = 9.4 Hz, 1H), 6.84 (d, *J* = 8.5 Hz, 1H), 6.34 (d, *J* = 9.4, 1.8 Hz, 1H), 3.39–3.31 (m, 2H), 3.20 (dd, *J* = 6.7 Hz, 2H), 1.62–1.48 (m, 4H), 1.43–1.19 (m, 4H).

MS (ESI) *m*/*z*: $[M + H]^+$ calc for $C_{17}H_{23}N_5O_4$ (ODIN isocyanate reacted with methanol), 362.18; found, 362.26.

IR, ῡ (cm-1): 3390 (N-H stretching), 2926 (C-H stretching), 2938 (C-H stretching), 2262 (N=C=O stretching), 1660 (C=O stretching, urea e lactam), 1594 (N-H bending, urea), 1533 (C-N stretching), 1242 (C-O stretching).

Synthesis of *isopropyl (6-(3-(7-oxo-7,8-dihydro-1,8-naphthyridin-2-yl)ureido)hexyl)carbamate (1)*

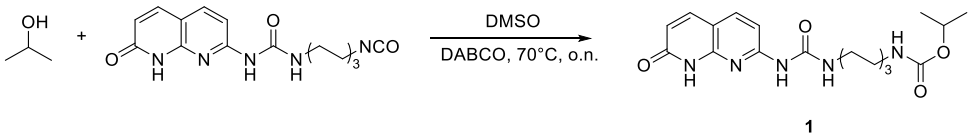

Scheme 3. Reaction between isopropanol and ODIN-isocyanate to give model compound 1.

1-(6-isocyanatohexyl)-3-(7-oxo-7,8-dihydro-1,8-naphthyridin-2-yl)urea (100 mg, 0.23 eq) was dissolved in 1 mL of dry DMSO, then 2-propanol (10 mL, 100 eq.) and two drops of dibutyltin dilaurate were added to the reaction mixture. The mixture was stirred at 70°C for one night. The product was precipitated in water and washed with water.

^{1}H NMR (600 MHz, DMSO-d_6): δ 12.13 (s, 1H, Ar−N*H*), 9.61 (s, 1H, Ar−NH−CO−N*H*), 8.94 (t, 5.9 Hz, 1H, NH−CO−N*H*), 7.87 (d, *J* = 8.6 Hz, 1H), 7.73 (d, *J* = 9,5 Hz, 1H), 6.91 (t, *J*=8.5 Hz, 1H), 6.81 (d, *J* = 5.9 Hz, 1H, N*H*−CO), 6.30 (d, *J* = 5,9 Hz, 1H), 4.68 (q, *J* = 6,18 Hz, 1H), 3.16 (d, *J* = 6.4 Hz, 2H), 2.90 (d, *J* = 6.4 Hz, 2H), 1.58 – 1.13 (m, 8H), 1.10 (d, *J* = 6.2 Hz, 4H).

IR υ̃(cm^{-1}): 3312 (N-H stretching), 3225 (N-H stretching), 2926 (C-H stretching), 2853 (C-H stretching), 1657 (C=O stretching), 1609 (N-H bending, urea), 1513 (C-N stretching).

Synthesis of *1-(6-isocyanatohexyl)-3-phenylurea (2)*

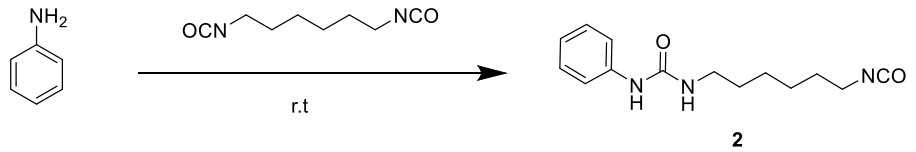

Scheme 4. Preparation of PU-isocyanate.

In a dry two-neck flask, aniline (1 g, 0.011 mol) and hexamethylene diisocyanate (HDI, 20 mL, 0.12 mol) were added and the reaction mixture was maintained at room temperature under stirring for four hours. Then, cyclohexane was added to promote product precipitation. The precipitate was filtered and washed with cyclohexane to remove excess HDI; the obtained white solid was dried in a vacuum oven at 40°C for two hours (yield 91%).

^{1}H NMR (600 MHz, DMSO-d_6) δ (ppm): 8.39 (s, 1H, N*H*-C=O-NH), 7.36 (d, *J* = 7.6 Hz, 2H, CH_{Ar}), 7.22 – 7.17 (m, 2H, CH_{Ar}), 6.87 (t, , *J* = 7.3 Hz, 1H), 6.09 (t, J = 5.6 Hz, 1H, NH-C=O-N*H*), 3.35(m, 2H, CH_2-NCO), 3.06 (td, J = 6.9, 5.7 Hz, 2H, C=O-NH-CH_2), 1.56 (p, *J* = 6.7 Hz, 2H, CH_2-CH_2-NCO), 1.43 (p, *J* = 7.0 Hz, 2H, NH-CH_2-CH_2), 1.36 – 1.26 (m, 4H).

IR, υ(cm^{-1}): 3319 (N-H stretching), 2933 (C-H stretching), 2958 (C-H stretching), 2262 (N=C=O stretching), 1648 (C=O stretching), 1596 (N-H bending, urea), 1551 (C-N stretching).

General procedure for the synthesis of PKHB-ODIN 8 and 13%

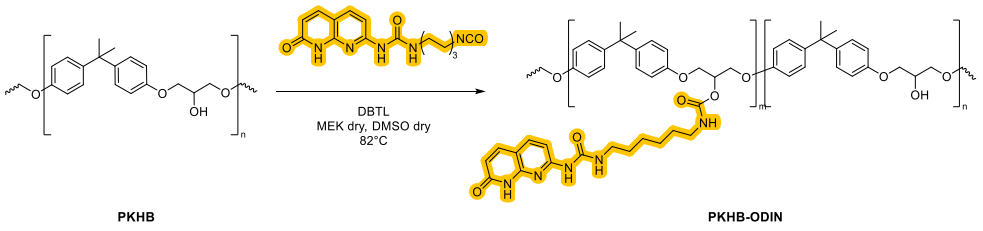

Scheme 5. Preparation of PKHB-ODIN.

5g of PKHB (18.0 mmol) were dissolved in 50mL of methyl ethyl ketone (MEK) at 50°C, then DABCO (20 mg, 180 µmol) were added to the reaction mixture. Then 1.19g (8%) or 2.38g (13%) of 1-(6-isocyanatohexyl)-3-(7-oxo-7,8-dihydro-1,8-naphthyridin-2-yl)urea (corresponding to 3,61 mmol, 7.22 mmol ,10.8 mmol respectively) dissolved in 10, 20 mL respectively of DMSO were added under magnetic stirring. After 24 hrs in refluxing MEK, 300 mL of water are added to the solution. The resulting yellow precipitate was filtered, washed with water

several times and dried in vacuum oven at 10^{-2} Torr and 60 °C for 24 h and then characterized via ^{1}H NMR (Fig. S3).

^{1}H NMR PKHB-ODIN (600 MHz, DMSO-d_6) δ ppm: 12.13 (s, Ar–N*H*), 9.62 (s, C=O-N*H*-C=N), 8.95 (s, N*H*-CO-NH-Ar), 7.91 (d, *J* = 8.5 Hz, C$H_{\text{Ar-ODIN}}$), 7.78 (d, *J* = 9.6 Hz, C$H_{\text{Ar-ODIN}}$), 7.34 (m, O-C=O-N*H*), 7.07 (d, *J* = 8.2 Hz, $CH_{Ar,PKHB}$,), 6.82 (d, *J* = 8.2 Hz, $CH_{Ar,PKHB}$), 6.64 (d, *J* = 8.5 Hz, C$H_{\text{Ar-ODIN}}$), 6.34 (d, *J* = 9.6 Hz, C$H_{\text{Ar-ODIN}}$), 5.34 (d, *J* = 5.3 Hz, O*H*), 5.19 (m, CH_2-C$H_{\text{PKHB-ODIN}}$-CH_2), 4.19-4.06 (m, CH_2-$CH_{PKHB-ODIN}$-CH_2, CH2-CH_{PKHB}-CH_2), 4.05-3.87 (m, CH_2-CH_{PKHB}-CH_2), 3.20 (m, C=O-NH-CH_2), 2.96 (m, CH_2-NH-C=O-O), 1.54 (s, CH_3), 1.42 – 1.16 (m, NH-CH_2-(CH_2)$_4$-CH_2-NH).

IR, ῡ (cm^{-1}): 3300 (O-H stretching), 2929 (C-H stretching), 1655 (NH(C=O)O stretching), 1233 (CO stretching, ether), 1034 (C-O stretching).

EA PKHB-ODIN 8%: Theoretical C 75.99%, H 7.28%, N 1.59%; Found C 74.68%, H 7.01%, N 1.69%.

EA PKHB-ODIN 13%: Theoretical C 74.01%, H 6.94%, N 2.42%; Found C 72.52%, H 7.02%, N 2.39%.

General procedure for the synthesis of PKHB-PU 23%

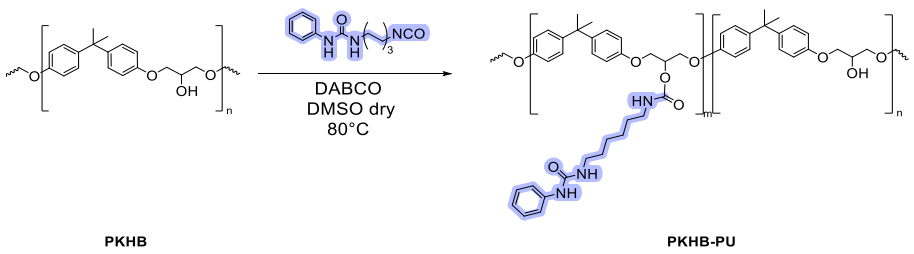

Scheme 6. Preparation of PKHB-PU

5g of PKHB (18.0 mmol) were dissolved in 50 mL of dry DMSO at 80°C, then DABCO (20 mg, 180 µmol) is added to the reaction mixture. Then phenyl urea isocyanate (1.88 g, 7.21 mmol) is added to the reaction mixture under magnetic stirring. After 24 hrs at 80°C the polymer is precipitated by adding 300 mL of

water are added to the solution. The resulting white precipitate was filtered and dried in vacuum oven at 10^{-2} Torr and 60 ◦C for 24 h and then characterized via ^{1}H NMR (400 MHz, DMSO-d_6).

^{1}H NMR (400 MHz, DMSO-d_6) δ (ppm): 8.38 (s, Ar-N*H*-*C*=*O*), 7.32 (d, *J* = 7.7 Hz, CH-$_{\text{Ar-PU}}$-H_{orto}), 7,29 (t, J=3,52 Hz, C=O-N*H*) 7,14 (m, $CH_{\text{Ar-PU}}$-H_{meta}), 7.02 (d, *J* = 7.8 Hz, $CH_{Ar,PKHB}$), 6.93 (d, J=8.4 Hz, $CH_{\text{Ar-PU}}$-H_{para}), 6.81 (d, *J* = 7.8 Hz, $CH_{Ar,PKHB}$), 6.05 (bs, N-*H*-C=O-O), 5.34 (d, J=5.3 Hz, O*H*), 5.14 (m, CH_2-$CH_{\text{PKHB-PU}}$-CH_2), 4.10 (m, CH_2-$CH_{PKHB-PU}$-CH_2), 4.05 (m, CH_2-CH_{PKHB}-CH_2) 4.00 – 3.87 (m, CH_2-CH-$CH_{2\ PKHB}$), 2.99 (m, C=O-NH- CH_2), 2.92 (m, CH_2-NH-C=O-O), 1.50 (s, CH_3), 1,47-1.16 (m, NH-CH_2-$(CH_2)_4$-CH_2-NH).

IR, ῡ (cm-1): 3300 (O-H stretching), 2965 (C-H stretching), 1655 (NH(C=O)O stretching), 1237 (C=O stretching, ether), 1040 (C-O stretching).

EA PKHB-PU 23%: Theoretical C, 73.97%; H, 7.15%; N, 2.80%; Found C, 72.36%, H 7.28%, N 2.96%.

Elemental analyses	**%C**	**%H**	**%N**	**%S**
PKHB-ODIN 8% Theoretical	75.99%,	7,28%	1.59%	0%
PKHB-ODIN 8% Found	74.68%,	7.01%	1.69%;	0%
PKHB-ODIN 13% Theoretical	74.01%	6.94%	2.42%;	0%
PKHB-ODIN 13% Found	72.52%	7.02%	2.39%	0%
PKHB-PU 23% Theoretical	73.97%	7.15%	2.80%	0%
PKHB-PU 23% Found	72.36%	7.28%	2.96%	0%

Table 3. Theoretical and experimental C, H, N, S elemental analyses of the synthetized polymers. The S elemental analysis was done to exclude the presence of residual DMSO in the final products.

6.1.3 ^{1}H-NMR spectra

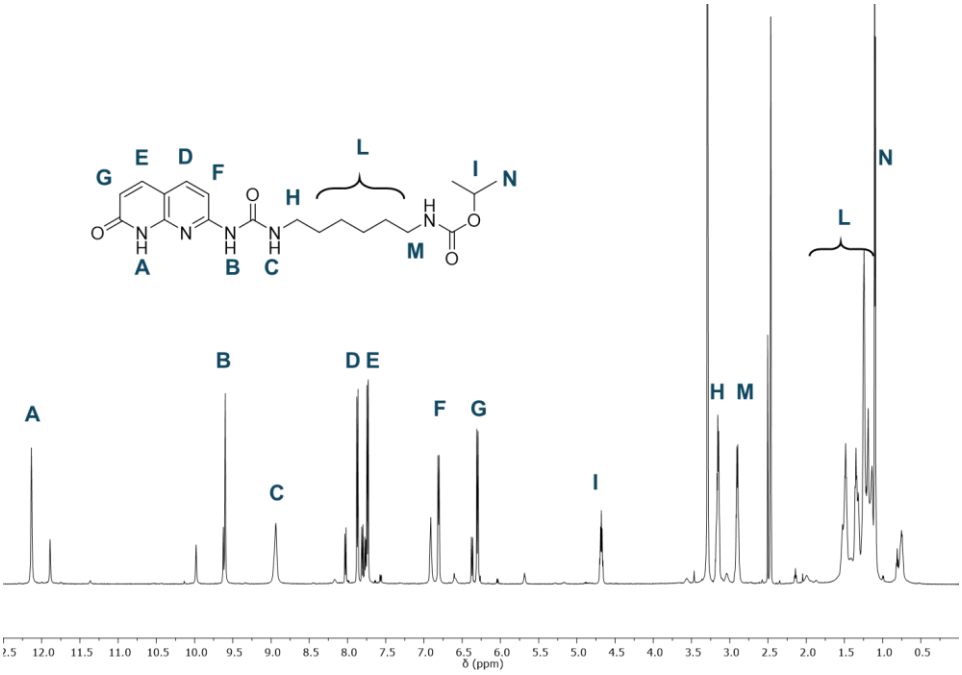

Figure 10. ^{1}HNMR (DMSO-d_6, 600 MHz, 25°C) of **(1)**.

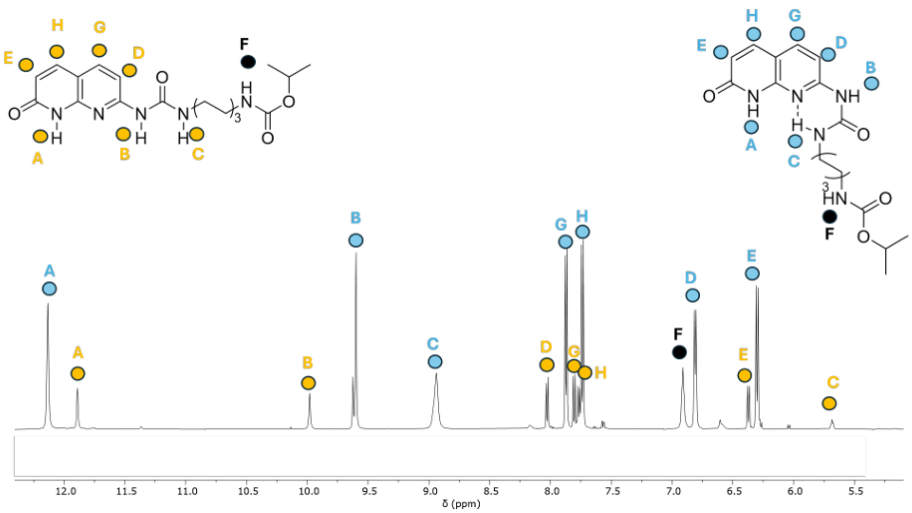

Figure 11. Expansion of the 1H NMR spectrum of model compound **1** in DMSO-d_6, with the resonances assigned to the two keto tautomers: **1a** (blue dots) and **1b** (orange dots). Ratio **1a/1b = 4:1.**

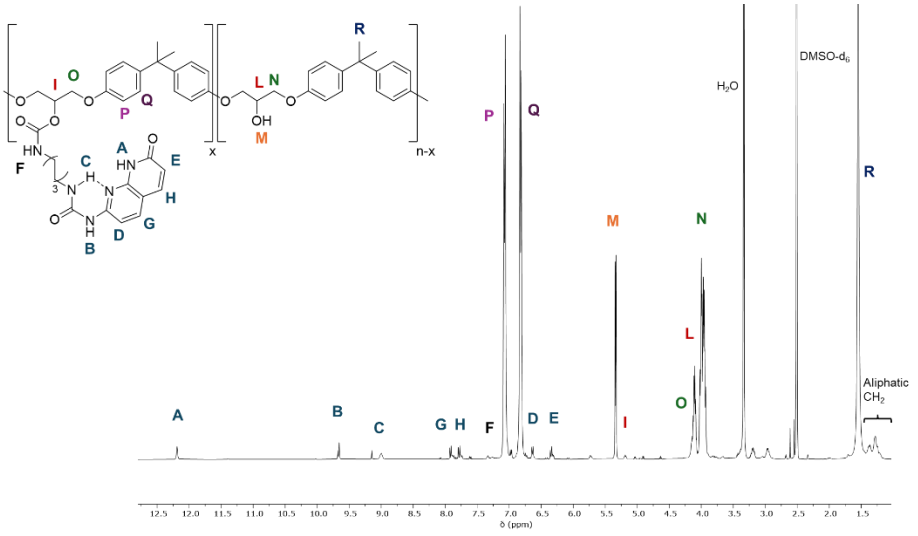

Figure 12. [1]HNMR (DMSO-d_6, 600 MHz, 25°C) of PKHB-ODIN 8%.

6.1.4 ATR FT-IR spectra

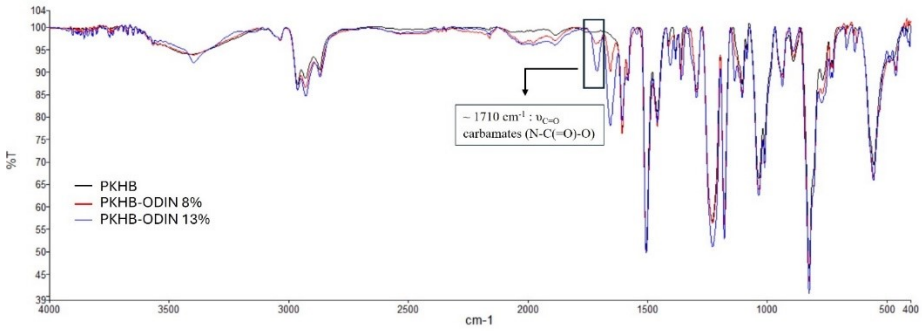

Figure 13. Comparison of ATR spectra of PKHB (black line), PKHB-ODIN 8% (red line), PKHB-ODIN 13% (blue line).

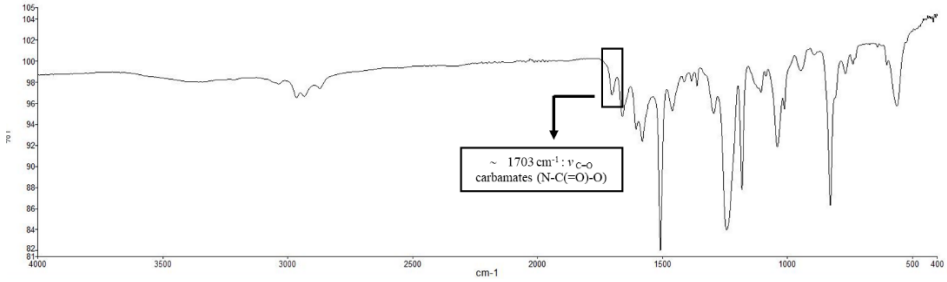

Figure 14. ATR FT-IR spectra of PKHB-PU 23%.

6.1.4 DSC analysis

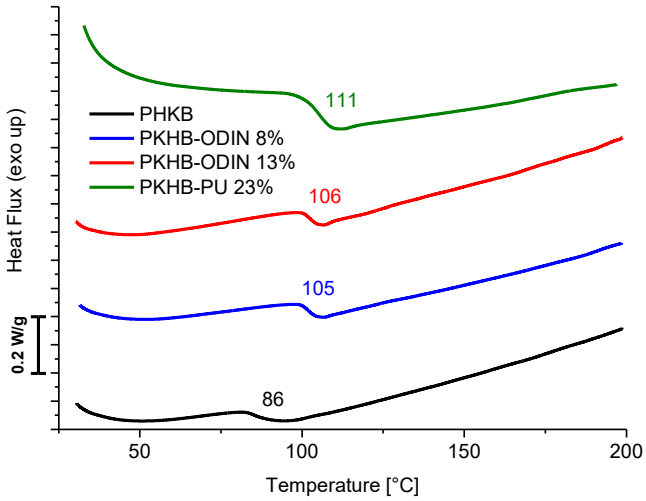

Figure 15. DSC curves of PKHB (black trace), PKHB-PU (green trace) PKHB-ODIN 8% (blue trace) and PKHB-ODIN 13% (red trace).

6.1.6 Viscoelastic properties

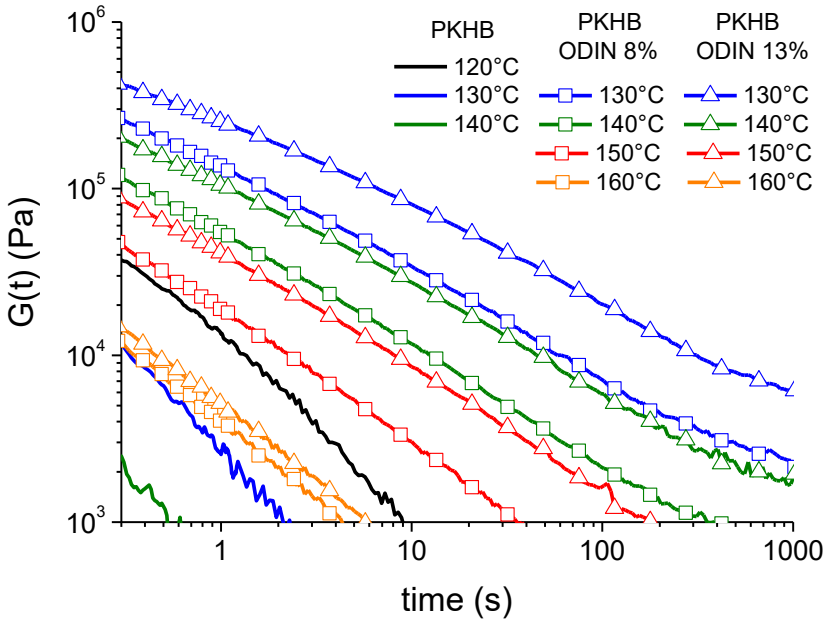

Figure 16. Stress relaxation of PKHB ODIN vs pristine PKHB.

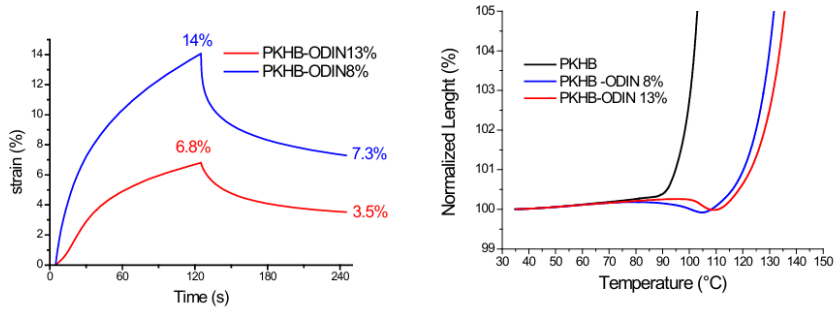

Figure 17. Isothermal creep for PKHB ODIN at 100°C under 100 KPa static load (a, left) and non-isothermal creep (b, right).

6.1.7 Single Lap Shear (SLS) tests

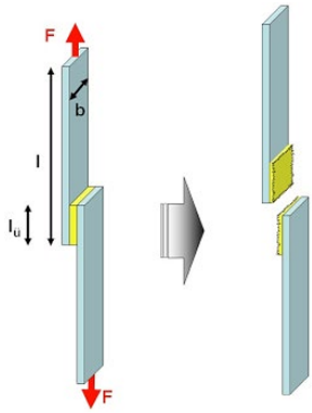

$$\tau = \frac{F}{A} = \frac{N}{mm^2} = MPa$$

Where $A = b \cdot l_u$

Figure 18. Single Lap Shear test configuration and shear strength definition.

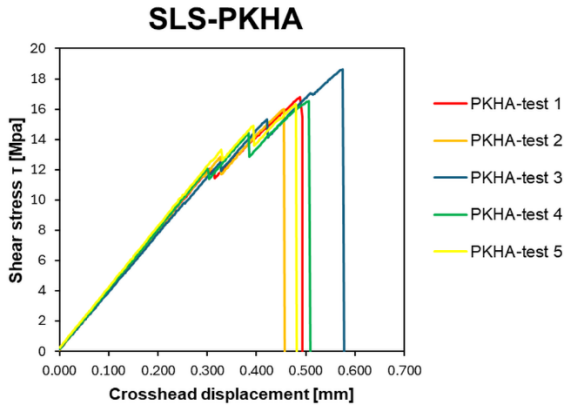

Figure 19. Stress and strain curves for specimens jointed with PKHA.

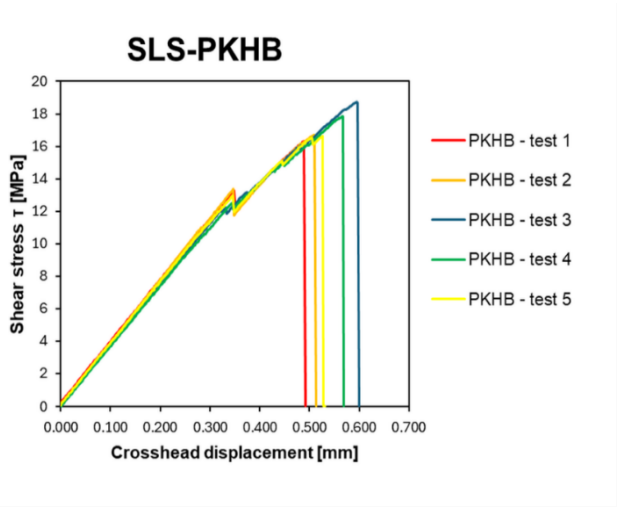

Figure 20. Stress and strain curves for specimens jointed with PKHB.

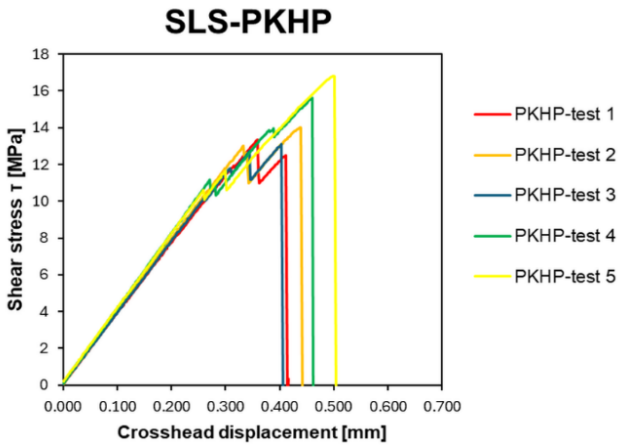

Figure 21. Stress and strain curves for specimen jointed with PKHP.

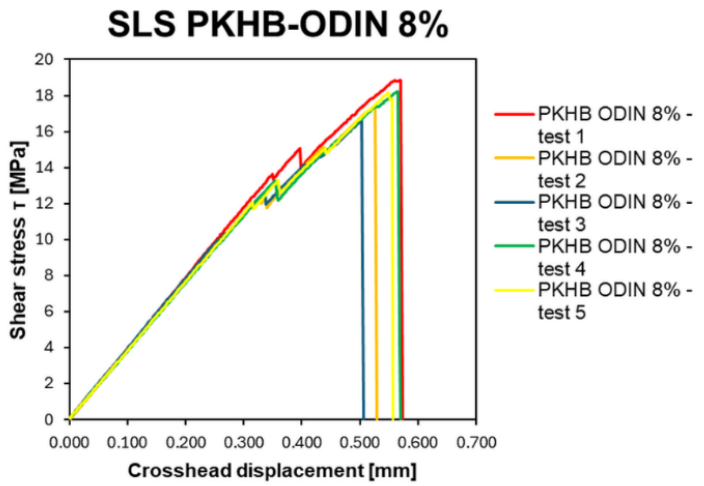

Figure 22. Stress and strain curve for specimens jointed with PKHB-ODIN 8%.

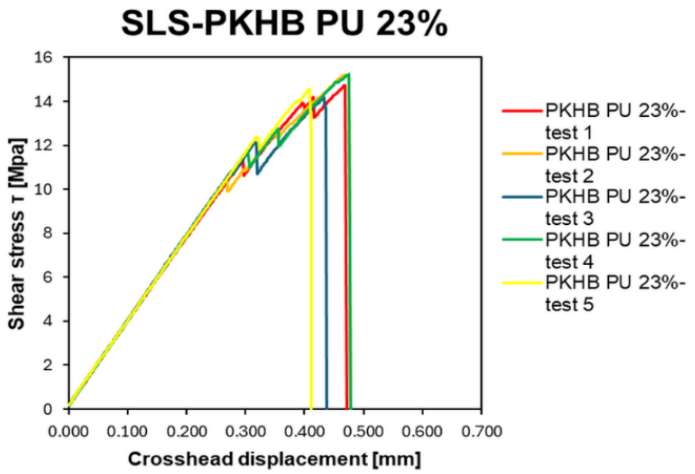

Figure 23. Stress and strain curves for specimens jointed with PKHB-PU 23%.

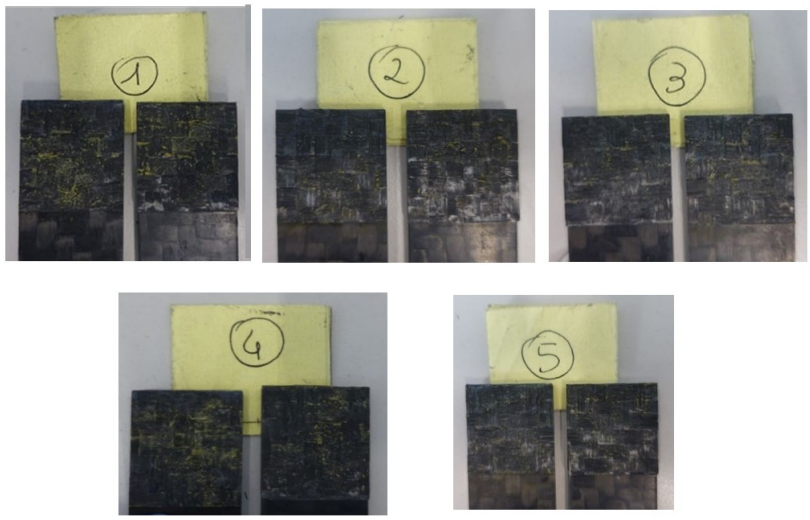

Figure 24. Photographs of cohesive rupture of SLS specimens of PKHB-ODIN 13%

6.1.8 Delamination tests

Mode I Opening | Mode II In plane shear | Mode III Out of plane shear

Figure 25. Delamination modes in CFRP composites.

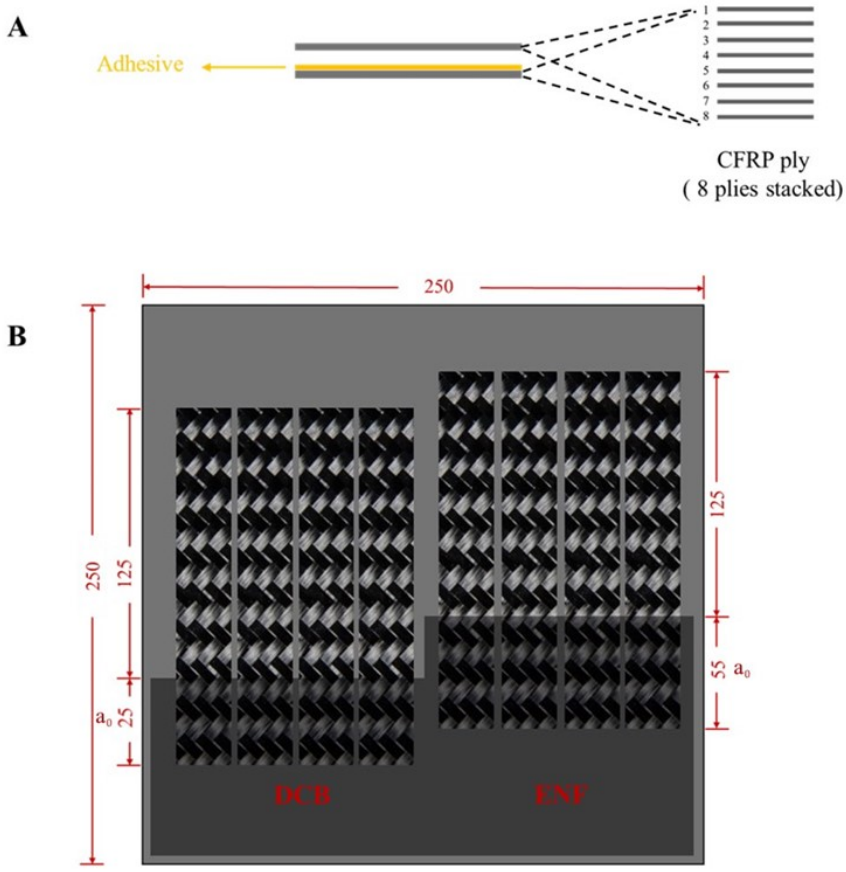

Figure 26. Stacking sequence of plies/mats for DCB and ENF panels production: (A) Reference laminates and modified laminates with the adhesives applied to the last interface of one ply. (B) Dimensions (in mm) of CFRP panels and specimens for DCB and ENF tests. The dark grey area indicates where the release of film 0.15 mm thick is applied.

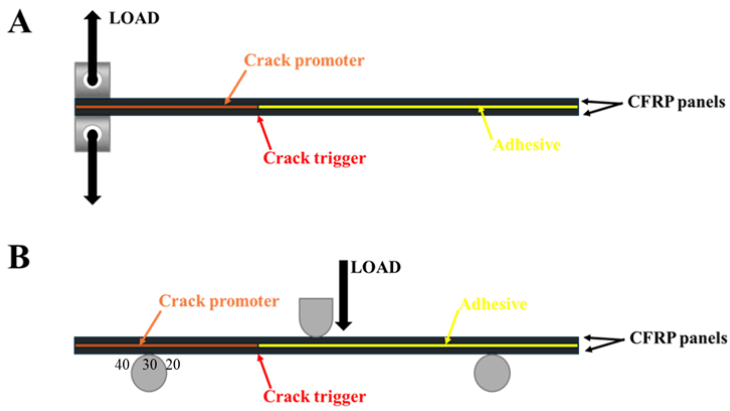

Figure 27. Schematic representation of specimens for the interlaminar fracture toughness evaluation in DCB A) and ENF (B).

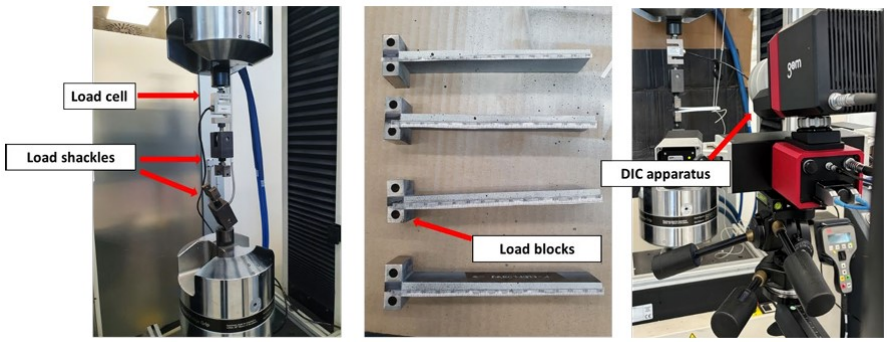

Figure 28. Experimental set-up of DCB tests, its specimen and DIC camera used to monitor the crack propagation.

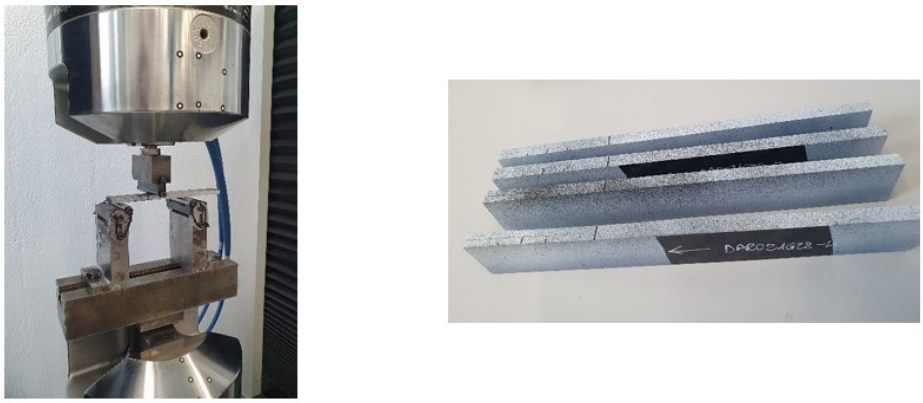

Figure 29. ENF tests setup and specimen geometry used for this test. In the image on the right, the end of the initial crack a_0 = 55 mm is evidenced by the black line to help in observing the crack propagation, that results in a misalignment of the reference line.

The standard procedure followed in the lab is to monitor the crack propagation starting from the artificial crack (realized with a release film). Every 5mm advance of the crack (observed in real-time from the DIC screen) a discharge-load cycle is carried out which will then be used if necessary to determine by correlation with finite element analysis the stiffness of the specimen. The loading and unloading curves shall be performed at the following crack deflection values: 20 mm; 25 mm; 30 mm; 35 mm; 40mm; 50 mm; 55 mm; 60 mm; 65 mm. At the end of the test (after about 50 mm of propagation of the crack, then when it has reached 70 mm on the millimeter scale) the sample is discharged at a speed of 2mm/min and the test is concluded. The data used for reprocessing are those extracted in .csv format from the DIC file, containing: transverse displacement (δ, obtained by marker); Force values and time. In particular, the force displacement curve is used for the next steps. By manual observation of the DIC images, the pairs of points deemed to be of interest are extracted from the curve and associated with the corresponding visually measured crack length (a). The choice of points of interest is made by avoiding the points following significant propagations of the crack and using, where

possible, those immediately preceding them. This usually improves the quality of results. Starting from this data set, the four analytical procedures proposed by the legislation are followed:

1) Modified beam theory (MBT): $G_I = \frac{3P \cdot \delta}{2 \cdot b \cdot a}$, where P = load; δ = displacement crosshead; b=gauge width; a=crack length.

2) Modified beam theory, corrected (MMBT): $G_I = \frac{3P \cdot \delta}{2b(a+|\Delta|)}$ where Δ is a correction to the delamination length obtained by linear regression from graph $C^{1/3}$-a, where C is the compliance obtained as δ/P.

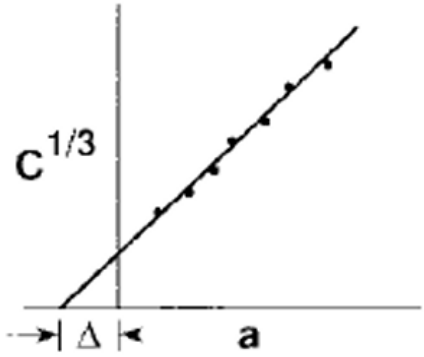

Figure 30. Graphical interpretation of the MMBT correction. 3) Compliance calibration (CC): $G_I = \frac{nP \cdot \delta}{2 \cdot b \cdot a}$, where n is the slope of the log(C)-log(a) graph obtained by linear regression.

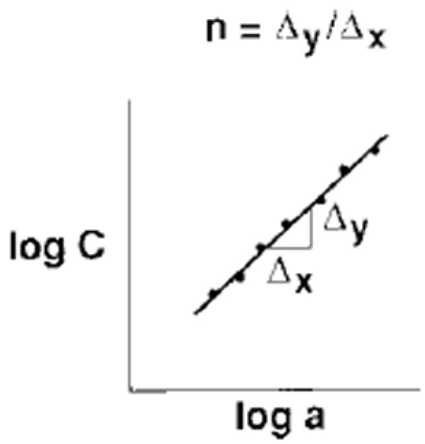

Figure 31. Graphical interpretation of the CC method.

4) Modified compliance calibration (MCC): $G_{II} = \frac{3P \cdot 2C^{2/3}}{2A1 \cdot b \cdot h}$ where h=thickness of the test piece; A1=slope of curve a/h-$C^{1/3}$.

For each test piece a curve called r-curve is then generated, with the displacement of the traverse δ on the X axis and the tenacity at fracture G_I measured in N/mm on the ordinate's axis.

The calculation of the average value of G_{IC} is carried out on the points of this curve, observing the following indications: in cases where the curve shows a plateau area, only points belonging to that region are used; where the plateau zone is not present, the mean is calculated on all points except the first (propagation from the crack apex with a form generated by the release agent due to the lack of pre cracking phase). During the procedure validation campaign, it was observed that the reprocessing method giving the most reliable results is the MMBT. The value taken as reference for G_{IC} is therefore that obtained by this method.

6.1.9 Double Cantilever Beam (DCB) and End Notched Fracture (ENF) results

DCB tests

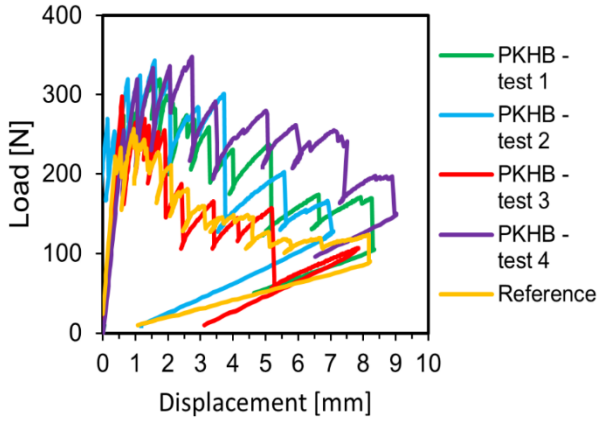

Figure 32. Load - displacement curves for PKHB specimens (colored lines) compared to average data of 4 reference specimens without any adhesive (yellow line).

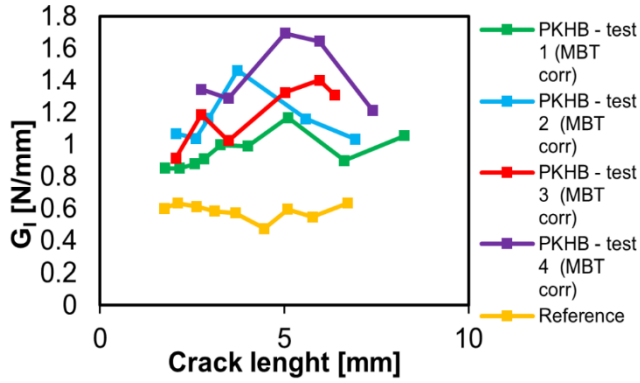

Figure 33. Resistance curves of PKHB adhesive compared to the reference.

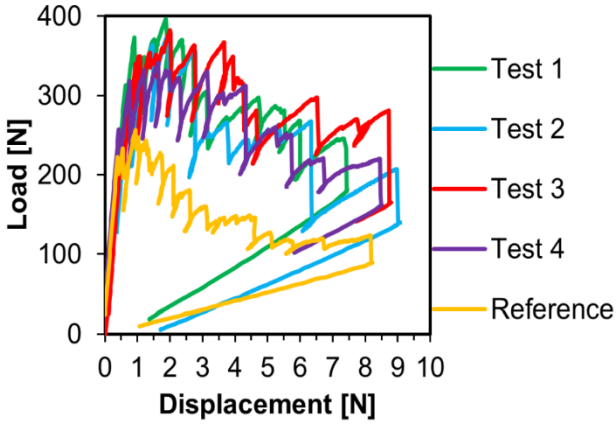

Figure 34. Resistance curves of PKHB-ODIN 13% adhesive compared to the reference.

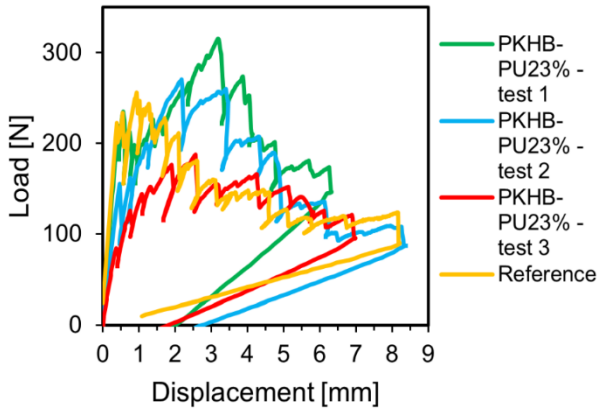

Figure 35. Load - displacement curves for PKHB-PU 23% specimens (colored lines) compared to average data of 4 reference specimens without any adhesive (yellow line).

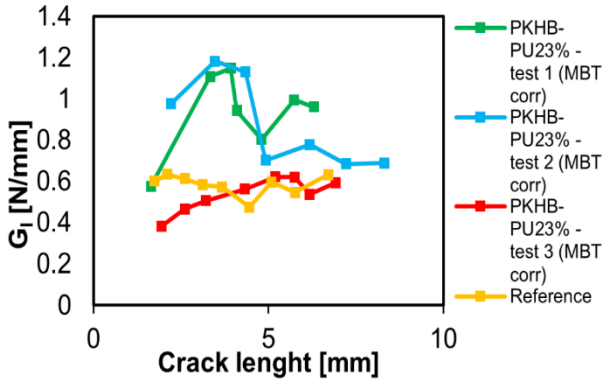

Figure 36. Resistance curves of PKHB-PU 23% adhesive compared to the reference.

Reference	Test 1	Test 2	Test 3	Test 4	Average [N/mm]	Standard Deviation [N/mm]
G_I (MMBT) [N/mm]	0.551	0.582	0.603	0.617	0.588	0.029
PKHB	**Test 1**	**Test 2**	**Test 3**	**Test 4**	**Average [N/mm]**	**Standard Deviation [N/mm]**
G_I (MMBT) [N/mm]	0.954	1.152	1.191	1.435	1.183	0.197
PKHB-ODIN 13%	**Test 1**	**Test 2**	**Test 3**	**Test 4**	**Average [N/mm]**	**Standard Deviation [N/mm]**
G_I (MMBT) [N/mm]	1.467	1.267	1.667	1.291	1,423	0.185
PKHB-PU 23%	**Test 1**	**Test 2**	**Test 3**	**Test 4**	**Average [N/mm]**	**Standard Deviation [N/mm]**
G_I (MMBT) [N/mm]	0.932	0.876	0.557	/*	0,788	0.203

Table 4. DCB test results for Reference specimens, PKHB, PKHB-ODIN 13% and PKHB-PU23% specimens. The values of GI are calculated with the Modified Beam Theory Method. The fourth specimen measurement of PKHB-PU 23% was discharged due to the loss of the load point displacement by the DIC camera.

ENF tests

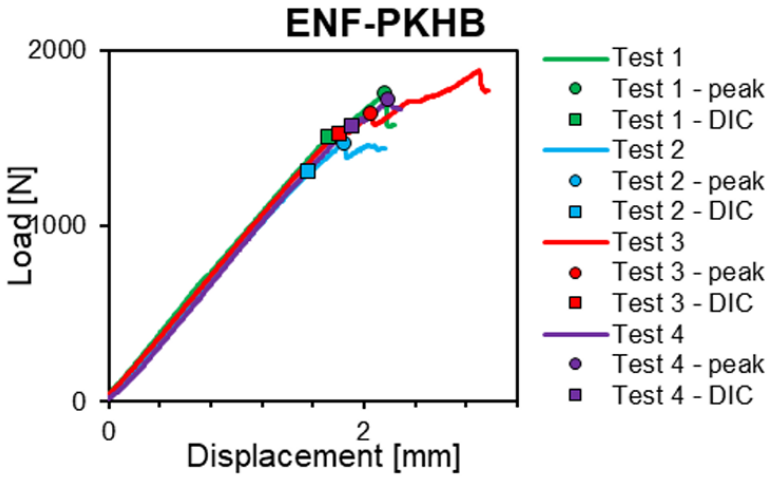

Figure 37. Resistance curves for PKHB specimens. The colored dots represent the point of crack propagation monitored by the MTS machine, while the colored circles represent the point of delamination determined by the DIC camera.

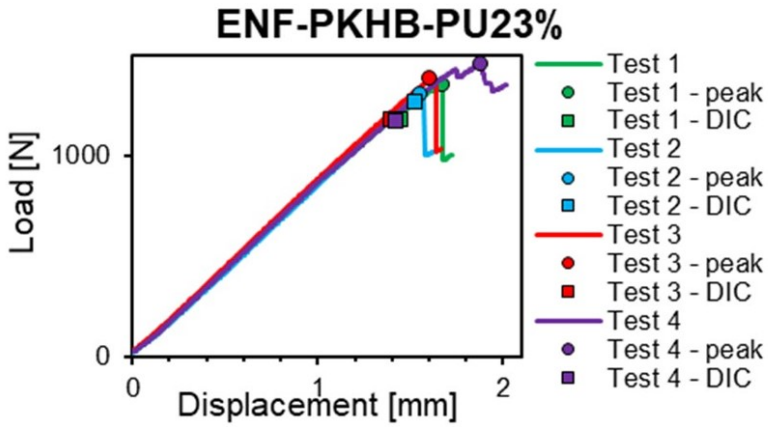

Figure 38. R-curves for PKHB-ODIN PU 23% specimen. The colored dots represent the point of crack propagation monitored by the MTS machine, while the colored circles represent the point of delamination determined by the DIC camera.

Reference	Test 1	Test 2	Test 3	Test 4	Average [N/mm]	Standard Deviation [N/mm]
G_{II} (peak) [N/mm]	0.97	0.97	0.93	1.34	1,05	0.19
G_{II} (DIC) [N/mm]	0.96	0.96	0.94	1.34	1.05	0.19
PKHB	**Test 1**	**Test 2**	**Test 3**	**Test 4**	**Average [N/mm]**	**Standard Deviation [N/mm]**
G_{II} (peak) [N/mm]	1.72	1.38	1.70	2.02	1.70	0.20
G_{II} (DIC) [N/mm]	1.27	1.09	1.45	1.69	1.37	0.20
PKHB-ODIN 13%	**Test 1**	**Test 2**	**Test 3**	**Test 4**	**Average [N/mm]**	**Standard Deviation [N/mm]**
G_{II} (peak) [N/mm]	1.84	1.91	2.03	2.42	2.05	0.20
G_{II} (DIC) [N/mm]	1.54	1.37	1.54	1.48	1.48	0.02
PKHB-PU 23%	**Test 1**	**Test 2**	**Test 3**	**Test 4**	**Average [N/mm]**	**Standard Deviation [N/mm]**
G_{II} (peak) [N/mm]	1.13	1.00	1.14	1.27	1.13	0.04
G_{II} (DIC) [N/mm]	0.86	0.93	0.83	0.82	0.86	0.01

Table 5. ENF test results for Reference specimens, PKHB, PKHB-ODIN 13% and PKHB-PU 23% specimens. G_{II} (peak) refers to the G_{II} values calculated considering the load that corresponds to a drop in the load curve, while G_{II} (DIC) refers to the G_{II} values calculated considering the load corresponding to the first pixel dealignment of the adherends observed with the DIC camera.

6.1.10 UV-Vis analysis

The absorption spectra of PKHB-ODIN 13% samples and PKHB-ODIN 13% dispersed (15% w/w) in epoxy-resin samples have an intrinsic contribution from the absorption of the polymeric matrix; the absorbance of the bare resin was measured and then subtracted from the sample after correcting for thickness variations, the results have been reported in Figure S31. Absorption spectra of PKHB-ODIN 13% and PKHB-ODIN 13% dispersed (15% w/w) in epoxy-resin have been fitted with a linear combination of the absorption spectra of ODIN in DMSO (100% monomer) and ODIN in CHCl3 (100% dimer). The results are reported in Figure S32: The dashed spectra in both panels represents the absorption spectra of ODIN molecule in pure monomeric form (dashed blue line) and in pure dimeric form (dashed gray line) respectively. Such conditions correspond respectively to the absorption spectrum of ODIN in DMSO and CHCl3 solution. The red lines are the linear combination of monomer and

dimer spectra that constitute the optimal fit to the experimental spectra. Linear combination allowed us to estimate that PKHB-ODIN 13% contains roughly the 35% of dimer form of ODIN, while for PKHB-ODIN 13% dispersed (15% w/w) in epoxy resin the percentage of dimeric form is reduced to 15%.

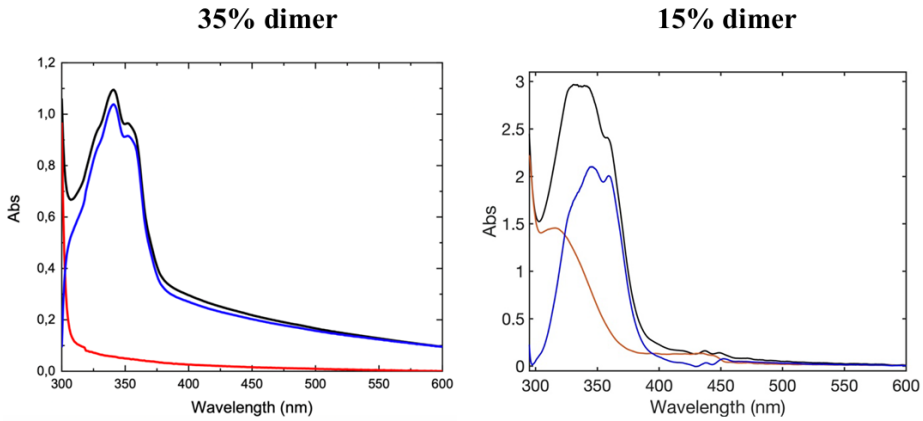

Figure 39. Absorption spectrum of PKHB-ODIN 13% (black line, left panel) and PKHB-ODIN 13% dispersed (15% w/w) in epoxy-resin (black line, right panel). The red lines are the absorption spectra of the resin substrates: PKHB (red line, left panel) and PKHB dispersed (15% w/w) in epoxy resin. The blue lines are the corrected absorption spectra: a) PKHB-ODIN 13% corrected for the PKHB absorption (left panel); b) PKHB-ODIN 13% dispersed (15% w/w) in epoxy-resin corrected for the PKHB dispersed (15% w/w) in epoxy-resin absorption.

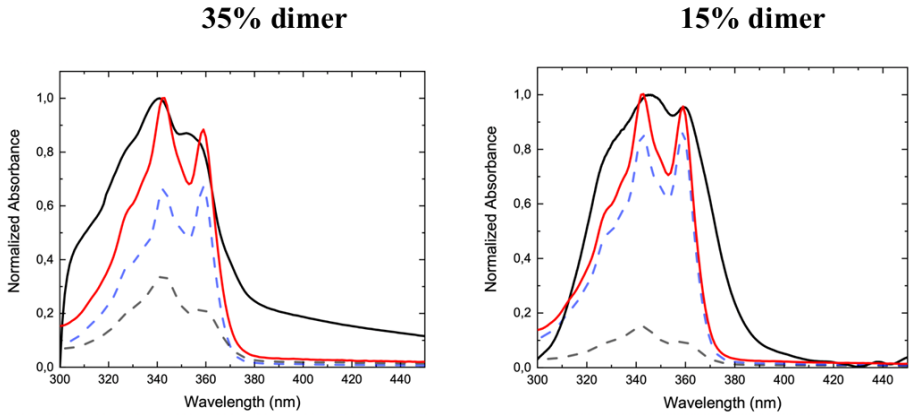

Figure 40. Experimental spectra of PKHB-ODIN 13% and PKHB-ODIN 13% dispersed (15% w/w) in epoxy-resin are reported as black lines respectively in left panel and right panel. The blue dashed spectra in both panels represents the absorption spectrum of ODIN in DMSO, while dashed gray line represents the spectrum in CHCl3. The red lines are the linear combinations of blue and grey spectra that constitute the optimal fit to the experimental spectra (black lines).

6.1.11 SEM micrographs of DCB and ENF specimens

DCB(a)

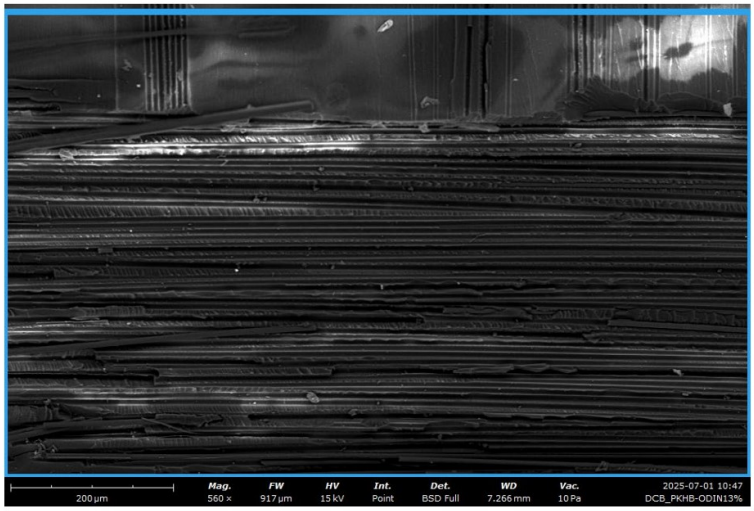

DCB (b)

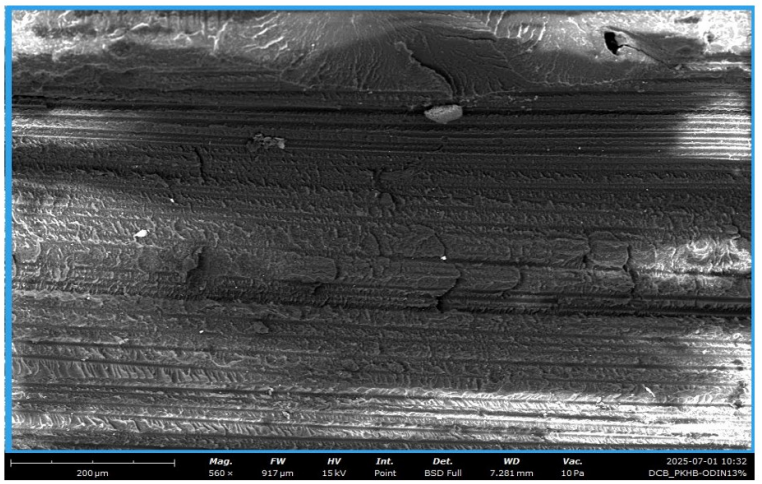

Figure 41. SEM micrographs of DCB failure surface of (a) reference specimen and (b) PKHB-ODIN 13% specimen.

ENF (a)

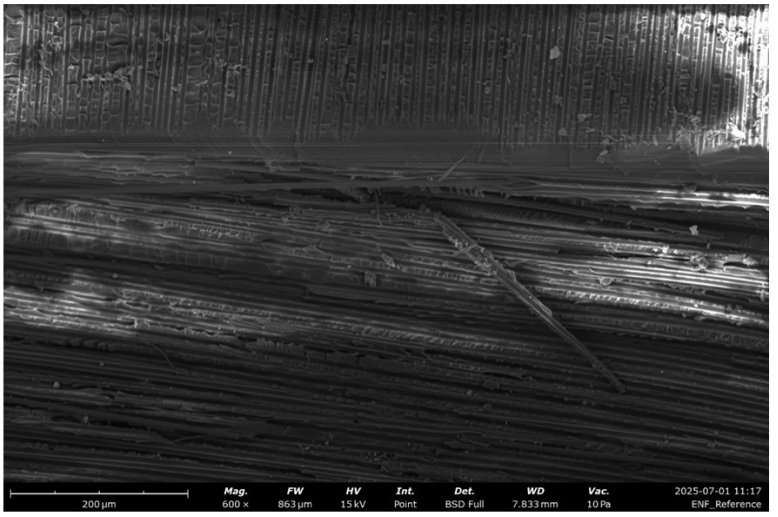

ENF (b)

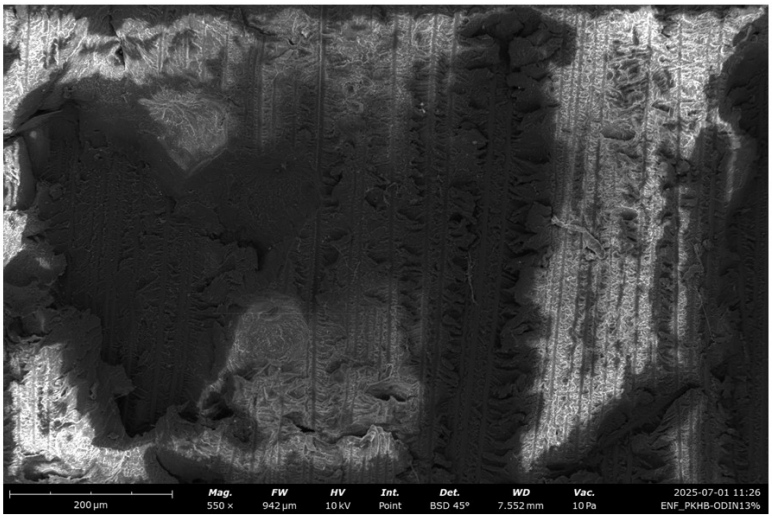

Figure 42. SEM micrographs of ENF failure surface of (a) reference specimen and (b) PKHB-ODIN 13% specimen.

7. References

[1] Senol H., Ulus H., Al Nadhari A, Topal S, Yildiz M (2025) Ameliorating tensile and fracture performance of carbon fiber-epoxy composites via atmospheric plasma activation: Insights into damage modes through in-situ acoustic emission inspection. Composites: Part A 195:108929. https://doi.org/10.1016/j.compositesa.2025.108929.

[2] Chawla KK, Composite Materials, Science and Engineering Third Edition, ISBN 978-0-387-74364-6, DOI 10.1007/978-0-387-74365-3 Springer New York.

[3] Wu X-F, Yarin AL (2013) Recent progress in interfacial toughening and damage self-healing of polymer composites based on electrospun and solution-blown nanofibers: An overview. J Appl Polym Sci 130:2225-2237. https://doi.org/10.1002/app.39282.

[4] Sridharan S. (2008), Delamination Behaviour of Composites. ISBN 978-1-84569-244-5 Elsevier.

[5] Bagheri R, Marouf BT, Pearson RA (2016) Toughening of Epoxy Nanocomposites: Nano and Hybrid Effects. Polym Rev 56:70–112. https://doi.org/10.1080/15583724.2015.1086368

[6] Maccaferri E, Mazzocchetti L, Benelli T, Brugo TM, Zucchelli A, Giorgini L (2022) Self-Assembled NBR/Nomex Nanofibers as Lightweight Rubbery Nonwovens for Hindering Delamination in Epoxy CFRPs. ACS

Appl Mater Interf 14:1885-1899. https://doi.org/10.1021/acsami.1c17643.
[7] Wang Y, Pillai SKR, Che J, Chan-Park MB (2017) High Interlaminar Shear Strength Enhancement of Carbon Fiber/Epoxy Composite through Fiber- and Matrix-Anchored Carbon Nanotube Networks. ACS Appl Mater Interf 9:8960-8966. https://doi.org/10.1021/acsami.6b13197
[8] Kaynan O, Hosseini E, Zakertabrizi M, Motta De Castro E, Pérez LM, Jarrahbashi D, Asadi A (2023) Multifunctionality through Embedding Patterned Nanostructures in High-Performance Composites Adv Mater 35:2300948. https://doi.org/10.1002/adma.202300948.
[9] Sasidharan S, Anand A (2023**)** Interleaving in Composites for High-Performance Structural Applications. Ind Eng Chem Res 62:16−39. https://doi.org/10.1021/acs.iecr.2c03061.
[10] Liu W, Sang C, Jin K, Hou J, Yin M (2024) Experimental investigations into damage mechanism in the low-velocity impact and tension-after-impact testing of z-pin reinforced curved CFRP composite. Polym Compos 45:5051-5067. https://doi.org/10.1002/pc.28109.
[11] Hong H, Bae KJ, Jung H, Oh Y, You N-H, Lee J-C, Yu J (2022) Preparation and characterization of carbon fiber reinforced plastics (CFRPs) incorporating through-plane-stitched carbon fibers. Compos Struct 284:115198. https://doi.org/10.1016/j.compstruct.2022.115198.
[12] Liu J, Xue Y, Dong X, Fan Y, Hao H, Wang X (2023) Review of the surface treatment process for the adhesive matrix of composite materials. Int J Adhes Adhes 126:103446. https://doi.org/10.1016/j.ijadhadh.2023.103446.
[13] Al-Furjan MSH, Shan L, Shen X, Zarei MS, Hajmohammad MH, Kolahchi R (2022) Influence of carbon fiber failure mode caused by TiO_2 coating on the high temperature tensile strength of carbon fiber reinforced 7075 Al alloy composites. JMR&T 19:2930-2959. https://doi.org/10.1016/j.jmrt.2023.08.191.
[14] Xiong M, Xiong L, Xiong K, Liu F (2023) A new strategy for improvement of interface and mechanical properties of carbon fiber/epoxy composites by grafting graphene oxide onto carbon fiber with hyperbranched polymers via thiol-ene click chemistry. Polym Compos 44:5490-5498. https://doi.org/10.1002/pc.27503.
[15] Kostopoulos V, Kotrotsos A, Tsatzalis S, Loutas T, Bosman AW (2016) Toughening and healing of continuous fibre reinforced composites by supramolecular polymers. Compos Sci Technol 128:84-93. https://doi.org/10.1016/j.compscitech.2016.03.021.
[16] Yang J, Bai R, Chen B, Suo Z (2020) Hydrogel Adhesion: A Supramolecular Synergy of Chemistry, Topology, and Mechanics. Adv Funct Mater 30:1901693. https://doi.org/10.1002/adfm.201901693.
[17] Wen YW, Li M, Fan LF, Rong MZ, Zhang MQ (2024) Imparting Ultrahigh Strength to Polymers via a New Concept Strategy of

Construction of up to Duodecuple Hydrogen Bonding among Macromolecular Chains. Adv Mater 36:2406574. https://doi.org/10.1002/adma.202406574.

[18] Soavi G, Portone F, Battegazzore D, Paravidino C, Arrigo R, Pedrini A, Pinalli R, Fina A, Dalcanale E (2023) Phenoxy resin-based vinylogous urethane covalent adaptable networks. React Funct Polym 191:105681. https://doi.org/10.1016/j.reactfunctpolym.2023.105681.

[19] Tellers J, Canossa S, Pinalli R, Soliman M, Vachon J, Dalcanale E (2018) Dynamic cross-linking of polyethylene via sextuple hydrogen bonding array. Macromolecules 51:7680-7691. https://doi.org/10.1021/acs.macromol.8b01715.

[20] D'Auria S, Pedrini A, Ferraboschi I, Vachon J, Sissa C, Pinalli R, Dalcanale E (2023) Two-photon microscopy as a visual tool for polymer compatibilization monitoring: the PE-EVOH case. Soft Matter19: 1900-1906. https://doi.org/10.1039/D2SM01577C.

[21] Bertocchi F, Marchetti D, Doria S, di Donato M, Sissa C, Gemmi M, Dalcanale E, Pinalli R, Lapini A (2024) Tuning the Optical Properties Through Hydrogen Bond-assisted H-aggregate Formation: The ODIN Case. Chem Eur J 30:e202302619. https://doi.org/10.1002/chem.202302619.

[22] Golkaram M, Boetje L, Dong J, Suarez LEA, Fodor C, Maniar D, van Ruymbeke E, Faraji S, Portale G, Loos K (2019) Supramolecular Mimic for Bottlebrush Polymers in Bulk. ACS Omega 4:16481-16492. https://doi.org/10.1021/acsomega.9b02126.

[23] Etter MC (1990) Encoding and decoding hydrogen-bond patterns of organic compounds. Acc Chem Res 23:120-126. https://doi.org/10.1021/ar00172a005.

[24] Comparable increments have been obtained by adding 10% phenoxy resins to the epoxy resin component of CFRP prepregs: a) Van Velthem P., Ballout W., Horion J., Janssens YA, Destoop V., Pardoen T.; Bailly C. (2016) Morphology and fracture properties of toughened highly crosslinked epoxy composites: A comparative study between high and low Tg tougheners. Compos-B, 101, 14-20. http://dx.doi.org/10.1016/j.compositesb.2016.06.076. b) Van Velthem P, Gabriel S, Pardoen T, Bailly C, Ballout W (2021) Synergy between Phenoxy and CSR Tougheners on the Fracture Toughness of Highly Cross-Linked Epoxy-Based Composites. Polymers 13, 2477. https://doi.org/10.3390/polym13152477.

[25] Yildrin C, Ulus H, Sas HS, Topal S, Yildiz M (2025) Assessing the fracture and dynamic mechanical performance of CF/PEKK joints bonded with epoxy-based adhesive film for aerospace applications: Impact of thermal and cycling hygrothermal conditions. Compos-A: Appl Sci Manuf 190, 108659. https://doi.org/10.1016/j.compositesa.2024.108659.

Chapter 2

"Synthesis and characterisation of novel guanidinium functionalized cavitand"

1. Introduction

1.1 The Challenge of molecular recognition through ionic interaction in Supramolecular Chemistry

Supramolecular chemistry, the study of non-covalent interactions, is central to developing advanced functional materials and chemical sensors. A persistent challenge within this field is the design of robust synthetic receptors capable of selective and high-affinity binding to anionic guests that possess highly polar, negatively charged head group and a substantial non-polar, lipophilic tail or portion. Some of this molecules are industrial anionic surfactants[1] like sodium lauryl sulphate sodium stearate, sodium dodecyl or alkoxybenzene sulphonates and sodium lauroyl sarcosinate and biological species like the sodium salt of lysophosphatidic acid (LPA) (Figure 1).

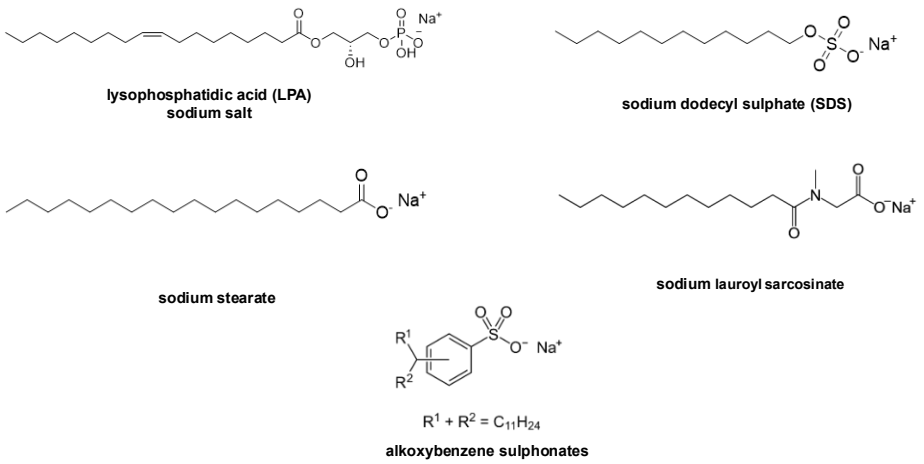

Figure 1. Anionic amphiphilic substances that possessed a negatively charged polar head and a lipophilic tail.

The field of anion binding faces several challenges when designing systems to successfully capture negatively charged ions[2]. Firstly, anions are typically larger

than their isoelectronic cation counterparts. This results in a lower charge density (a low charge-to-radius ratio) making them inherently more difficult to bind than cations[3]. Additionally, solvent choice requires careful consideration, as anions are often highly solvated. In the context of anion recognition, the Hofmeister serie[4] (Figure 2) is helpful for predicting anion desolvation energies. Anions to the left of chloride are known as kosmotropic; being well-hydrated, they incur high desolvation penalties and thus preferentially bind in non-polar solvents. Sulphate ions SO_4^{2-}, phosphate PO_3^{2-} or carboxylate anions COO^- are kosmotropic. However, the chain length of the R group bonded to the anionic ions increases its hydrophobic character, which tends to shift its behaviour toward being more chaotropic (water-structure breaking), as the non-polar part interferes with the water structure. Chaotropic anions are weakly hydrated, allowing them to bind preferentially to synthetic receptors in polar solvents.

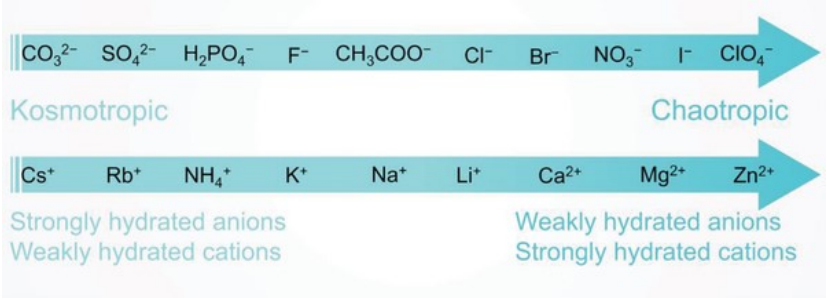

Figure 2. General order of kosmotropic and chaotropic anions/cations in the Hofmeister series. Figure adapted from reference[5].

Furthermore, anion binding is pH-sensitive, as anions can protonate at lower levels, which significantly reduces the strength of the interaction. Finally, since anions display a variety of geometries, achieving shape complementarity between the host and the guest—a factor essential for strong binding—is often difficult when aiming to bind a range of different anions.

The synthetic receptor designed for targeting anionic surfactants must simultaneously present a positive or hydrogen-bond-donating binding pocket to engage the anionic head via strong electrostatic or H-bonding interactions, and a suitably sized and preorganized hydrophobic cavity to accommodate the non-polar tail[6,7]. This dual-point binding is critical as it exploits the favourable hydrophobic effect (entropically driven) to boost the overall affinity, synergistically enhancing the selectivity provided by the specific polar interactions (entalpy-driven).

1.2 Quinoxaline cavitands

Resorcin[4]arenes based cavitands, introduced by Cram and co-workers[8], are exceptionally versatile platforms for supramolecular engineering. These compounds, generally referred as quinoxaline cavitands (QxCav), are obtained by the fourfold bridging of corresponding resorcinarene scaffolds with 2,3-dichloroquinoxalines derivatives.

Quinoxaline cavitands possess a well-defined and electron-rich cavity, that can be modified in shape or precisely functionalized to tune its complexation abilities towards neutral molecules through π–π and C-H··π interactions, for example for the complexation of aromatic molecules like BTEX and polycyclic aromatic hydrocarbons (PAHs)[9–11].

Furthermore, these systems exhibit a reversible conformational switch between a closed vase conformation (C_{4v} symmetry) and an open extended kite conformation (C_{2v} symmetry). The interconversion is influenced by many factors such as: I) solvent size and polarity[12], II) temperature[12], III) pH[13], IV) metal coordination and redox properties[14,15]. (Figure 3**).** For example, the vase conformation is prevalent in solution at room temperature or above, while the kite conformation is prevalent at -60°C due to solvation effects (the solvation

entropic term become more significant at lower temperatures). Moreover, the addition of trifluoroacetic acid (TFA) to a solution of QxCav induced the conformational change to the open kite form as consequence of the Coulomb repulsion between the protonated quinoxaline nitrogen atoms[16].

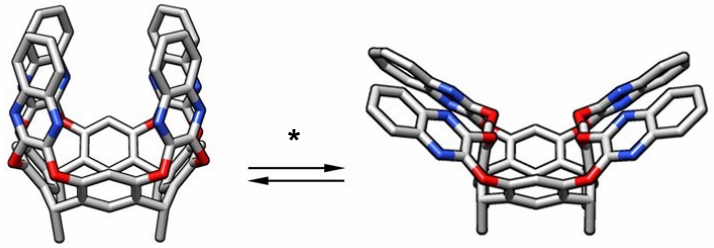

Figure 3. Schematic illustration of a quinoxaline cavitand switching from a closed vase conformation (left) to an open kite conformation (right).*The interconversion can be influenced with a change of temperature or pH or through metal coordination or redox processes.[17]

Due to their capacity to reversibly bind hydrophobic species via hydrophobic interactions, quinoxaline cavitands are potential candidates for the uptake of anionic surfactants. The inherent challenge of anionic surfactant binding is met by a dual recognition mechanism: the electron-rich hydrophobic cavity specifically binds the lipophilic tail of the surfactant, while a positively charged functional group at the upper rim of a quinoxaline can selectively engage the anionic head group through electrostatic interaction.

The guanidinium group is particularly effective for targeting anionic species[18]. This functional group adopts a planar conformation and remains protonate over a wide range of pH (pka = 12.5 c.a). These characteristics make it particularly

useful for recognizing and complexing anionic species with Y-shaped or tetrahedral geometry (e.g carboxylate or phosphate anions), exploiting the chelate effect (Figure 4).

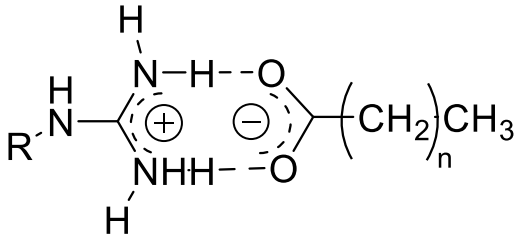

Figure 4. Interaction between a guanidinium group alkyl carboxylate anion.

In the past years the introduction of guanidinium functional group in the design of the molecular receptors is a strategy successfully used. For example, in the field of functionalized calix[4]arene, guanidinocalixarenes were synthesized by Casnati group[19] for the purpose of binding to negatively charged substrates through electrostatic interactions e.g acting like artificial phosphodiesterases by catalyzing the hydrolysis of a RNA model compound, 2-hydroxypropyl p-nitrophenyl phosphate (HPNP).

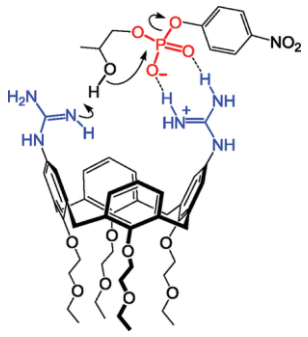

Figure 5. Scheme of the bifunctional general acid−base catalysis in the transesterification of HPNP. Figure adapted from reference[19].

Another study[20] showed a guanidinocalix[5]arene for the detection of perfluorinated alkyl substances (PFAS), specifically for perfluorooctane sulfonate (PFOS) and perfluorooctanoic (PFOA) in contaminated water. The association constant of the receptor for PFOA is calculated via fluorescent indicator displacement assay (IDA) and it is of (1.7 ± 0.3) ·10^7 M^{-1} in buffered water with HEPES (Figure 6).

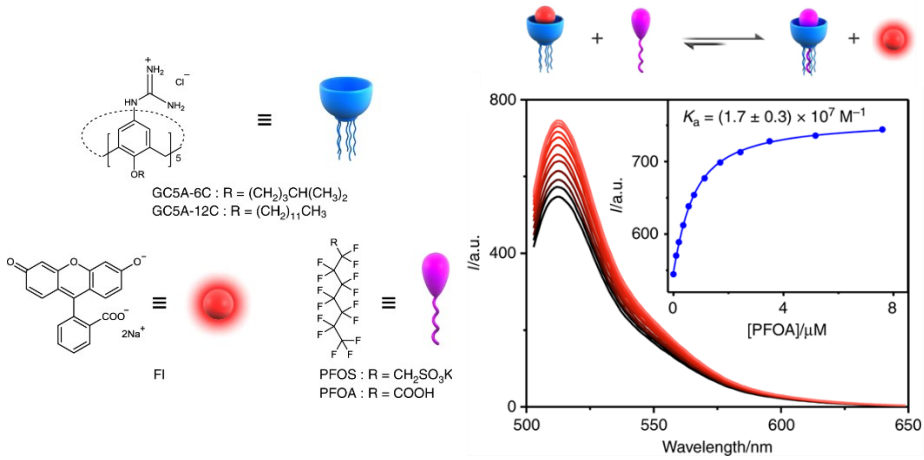

Figure 6. Chemical structures of the calixarene hosts synthetized in the study and the perfluorinated pollutants (PFOS and PFOA) studied. Schematic rapresentation of the IDA principle and competitive titration of GC5A-6C•Fl (0.4/0.5 μM) with PFOA (up to 7.6 μM). (Inset) The related titration curves of PFOA fit according to a 1:1 competitive binding model. All experiments were conducted in HEPES buffer at 25 °C, λ_{ex} = 500 nm, and λ_{em} = 513 nm. Data represented a mean ± s.d. (n = 3 independent experiments).

In 2016 Rebek[21] showed the application of a water-soluble cavitands as molecular chaperones to achieve the selective hydrolysis of long-chain diesters in an aqueous environment to give the corresponding alcohols. The cavitands function by catalysing the hydrolysis of an aliphatic diester leading to the formation of an included diol complex (Figure 7, right) in a folded J-shape conformation.

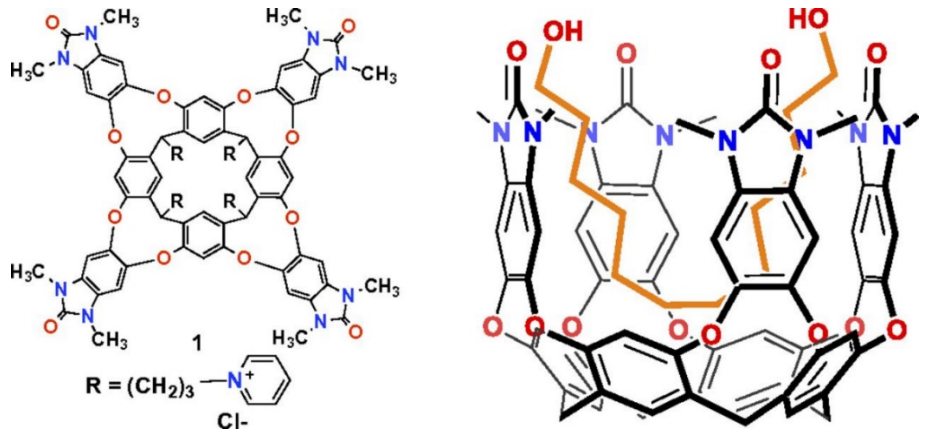

Figure 7. Chemical structure of the deep cavitand presented in the study[21]. Chemical structure of the cavitand in the receptive conformation as a complex with folded 1,12-dodecanediol in a J-shape; the R groups have been truncated.

2. Aim of the project

In this chapter, the design and synthesis of two quinoxaline cavitands with a guanidinium group at the upper rim **GUAQxCav** and **GUA2QxCav** is presented (Figure 8).

To date, this represents the firs example of a quinoxaline cavitand functionalized with a guanidinium group at the upper rim. This architecture is expected to surpass the inherent limitation of conventional anion binding by offering a powerful synergy of interaction. Specifically, the guanidinium group, which is stable across a broad of pH range, is expected to facilitate selectively and geometrically complementarity ionic interaction with the carboxylate group. Simultaneously the π-rich and hydrophobic cavity is suitable for encapsulate surfactant's alkyl chain by stabilizing C-H···π interactions.

In the first compound **GUAQxCav** the guanidinium group is separated from the electron-rich cavity of the cavitand through a methylene group while in the second one **GUA2QxCav** the guanidinium group is directly attached to one

quinoxaline wall. The synthesis of **GUAQxCav** was accomplished through a multistep protocol outlined in (Figure 9) and obtained with an overall yield of 20% starting from **QxCav**. The synthesis of **GUA2QxCav** by deprotection of the precursor Boc-protected compound **11** (Figure 16) is currently under study in our research lab.

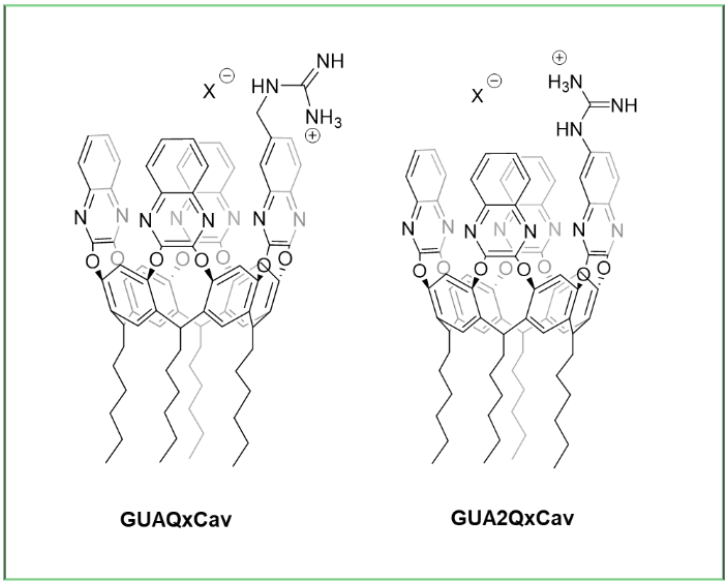

Figure 8. Chemical structure of the two target compounds **GUAQxCav** and **GUA2QxCav.** X=Cl for compound **GUAQxCav**.

3. Results and discussion

3.1 Synthetic strategy 1

The target molecule **GUAQxCav** was obtained through a convergent synthesis illustrated in Figure 9. The synthesis was initiated from the well-known compound QxCav, which synthesis[8] is extensively documented in the literature and will not be detailed here. QxCav was selectively modified by removing a

single quinoxaline wall, producing intermediate **1,** following a previously reported procedure[22].

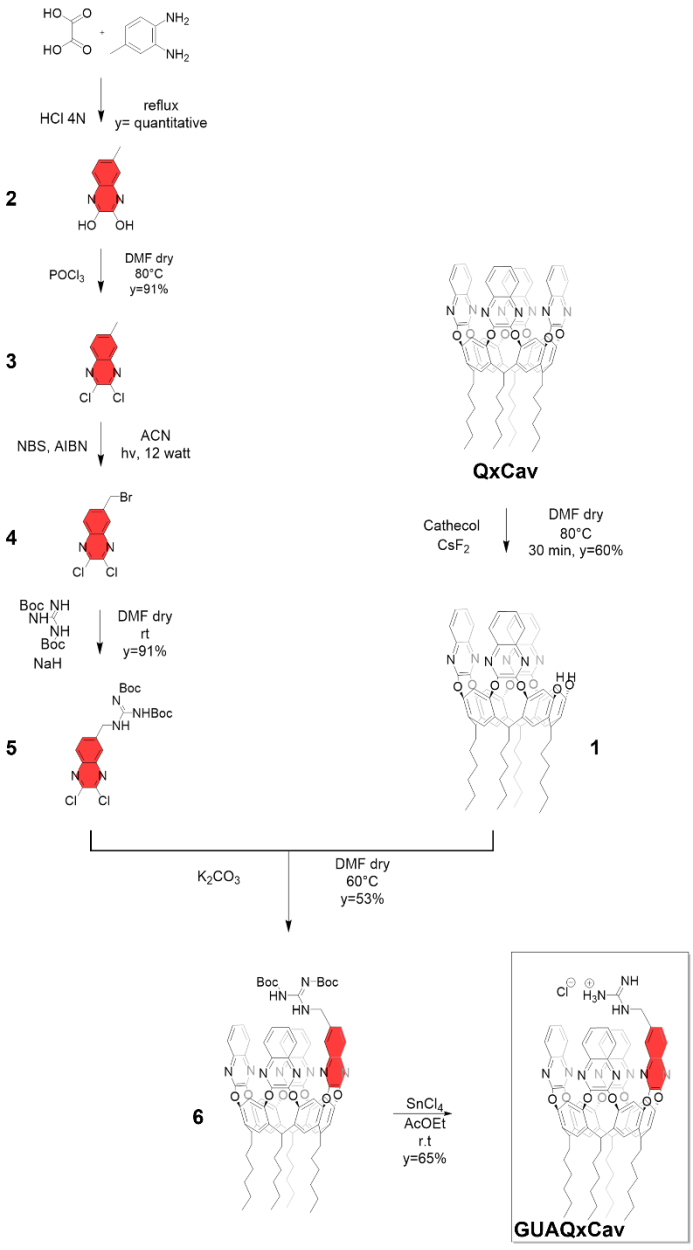

Figure 9. Synthetic strategy to obtain the target molecule **GUAQxCav**.

The 2,3-dihydroxy-6-methylquinoxaline, obtained by condensation of oxalic acid and diamino toluene, has been chlorinated with $POCl_3$ following the procedure described in literature[23] to give **3** with a yield of 91%. Then, 2,3-dichloro-6-methylquinoxaline **3** was brominated in benzylic position with NBS and AIBN in acetonitrile upon irradiation from a 12 Watt LED. This procedure avoids the usage of toxic solvents like CCl_4 that are usually involved in Wohl-Ziegler benzylic bromination reactions[24,25]. Since the polarity of brominated compound **4** is similar to that of reagent **3**, the separation is difficult and inefficient. Therefore, the reagent and the product are not separated, and the mixture is allowed to react in the subsequent reaction step. Through the acquisition of a spectrum in deuterated chloroform (Figure 21), we were able to confirm the presence of product **4** and calculate the molar ratios between the two existing species to set-up the quantities and molar ratios of the reagents necessary for the subsequent transformation. The content of intermediate **4** in the **3+4** mixture is 85% molar, calculated via ^{1}HNMR integration. The intermediate **5** was obtained by reacting in a SN_2-type of reaction the mixture of 2,3-dichloro-6-methylquinoxaline **3** and 2,3-dichloro-6-bromo-methylquinoxaline **4** in anhydrous DMF. The pure 2,3-dichloro-6-bis-Boc-guanidin-methylquinoxaline was purified by flash column chromatography with a yield of 91% and characterized by NMR analysis (Figure 10) and ESI mass spectrometry.

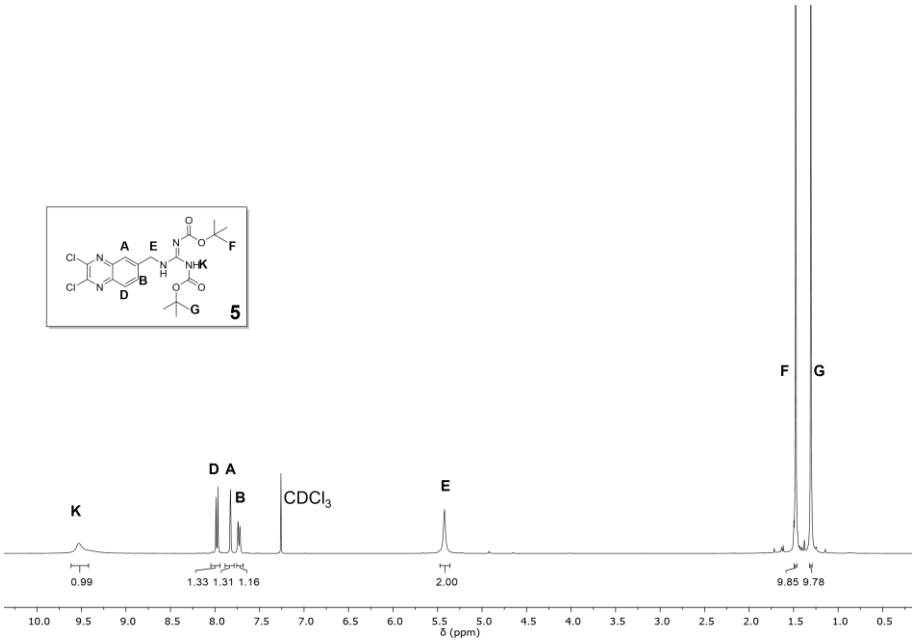

Figure 10. ^{1}HNMR (400 MHz, $CDCl_3$, 25 °C) intermediate **5**.

The NMR signals **F**, **G** and **K** are particularly indicative of the effective substitution of the Bis-Boc guanidine group and will also be present, with an analogous shape, on the cavitand featuring the functionalized quinoxaline **6**. The remaining signals are related to the aromatic hydrogens and the methylene hydrogens in α-position to the bis-boc guanidine. Quinoxaline **6** was reacted with compound **1** in a nucleophilic aromatic substitution reaction with potassium carbonate in dry DMF to give the Boc-protected cavitand **6** with a yield of 53%. The presence of the product is confirmed through NMR spectroscopy and ESI-MS (MeOH). From the proton NMR in deuterated DMSO (Figure 11) is possible to see the diagnostic singlet signals **G** and **F** of the Boc groups and the signal corresponding to the methylene protons **E** and **E'** that confirmed the functionalisation of the upper rim of the cavitand.

In particular because of the planar chirality of the cavitand, the two protons **E** and **E'** are diasterotopic and their coupling constant in deuterated acetone is of J=16.2 Hz.

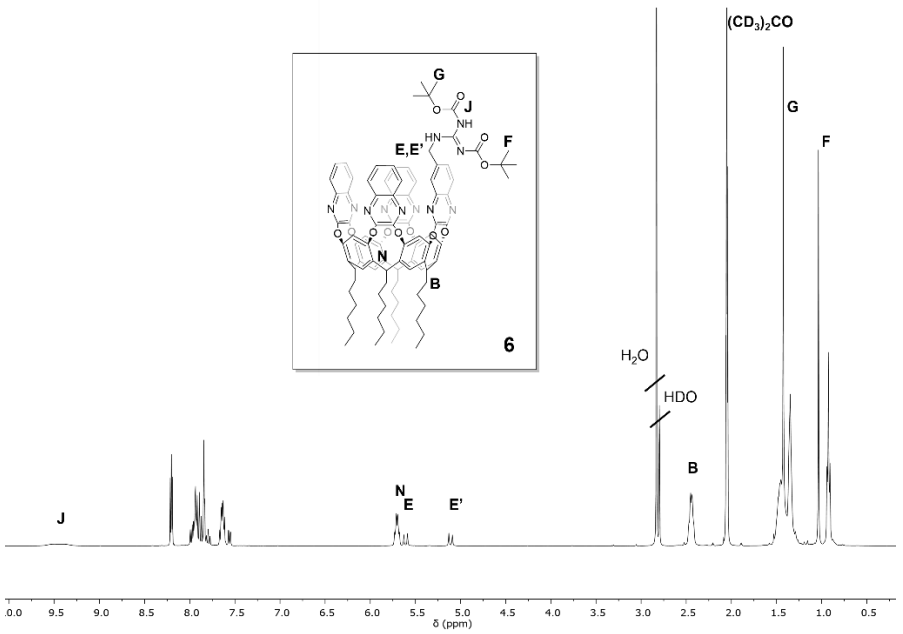

Figure 11. ^{1}HNMR (400 MHz, acetone-d_6, 25 °C) intermediate **6.**

In order to study the optimal deprotection conditions of the cavitand **6** a model compound was prepared.

3.1.1 Deprotection of the model compound 5a.

The model compound **5a** mimicking a quinoxaline wall with a guanidinium unit, is obtained by reacting the quinoxaline **5** with catechol with potassium carbonate in dry DMSO with a yield of 67% (Figure 12).

.

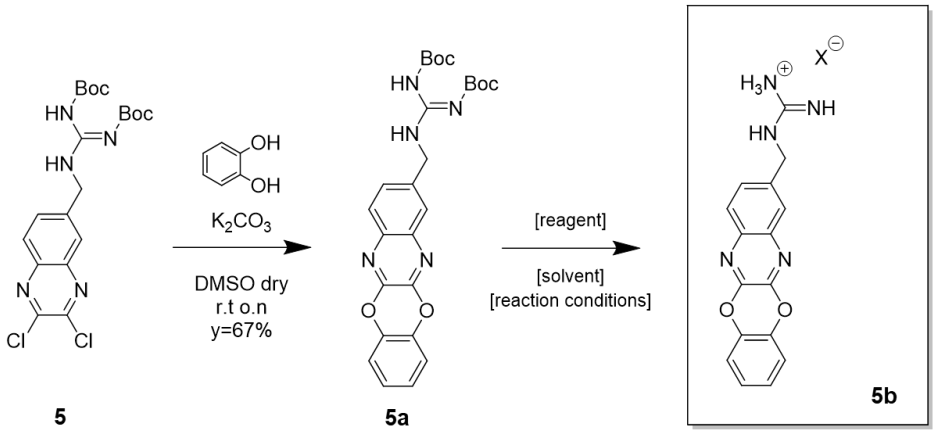

Figure 12. Synthetic scheme to obtain the model compound **5a**. The optimal deprotection conditions to get compound **5b** are studied.

To obtain the final deprotected product **5b** two reaction conditions were tested. The first one employed the use of anhydrous $SnCl_4$ in ethyl acetate and yielded the product as white solid with a yield of 65%. The proton NMR in deuterated acetone (Figure 13) confirmed the success of the reaction: the signals relative to the Boc group are not present. The doublet of the methylene protons **E** is due to its coupling with the N-*H* proton of the guanidinium group (J= 5.6Hz). The second procedure employed HCl 1M in dioxane and lead to the breakage of the ether bond between the aromatic portion of the quinoxaline and catechol.

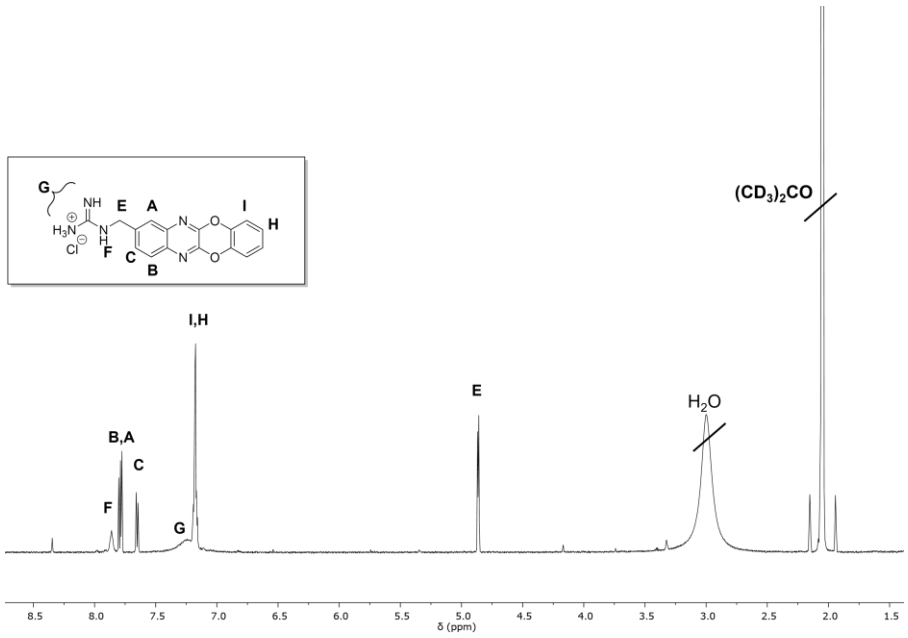

Figure 13. ^{1}HNMR (400 MHz, acetone-d_6, 25 °C) of the product **5b**.

The deprotection of the cavitand **6** was performed with the same reaction conditions of the model compound **5a**, with $SnCl_4$ in ethyl acetate. The product was isolated with a yield of 65% as a white solid and was characterized with NMR spectroscopy and MALDI-TOF mass spectroscopy. From the proton NMR in deuterated acetone (Figure 14), we can see that the shape of the signals of guanidinium group are very similar in shape and chemical shift to the one of the model compound **5b** (Figure 13). The 5.7 ppm resonance of protons **N** relative to the methine bridges is diagnostic of the vase conformation of cavitand **6** in solution. Protons **E** and **E′** that correspond to the methylene group of the guanidinium give a doublet of doublets due to the planar chirality of the cavitand.

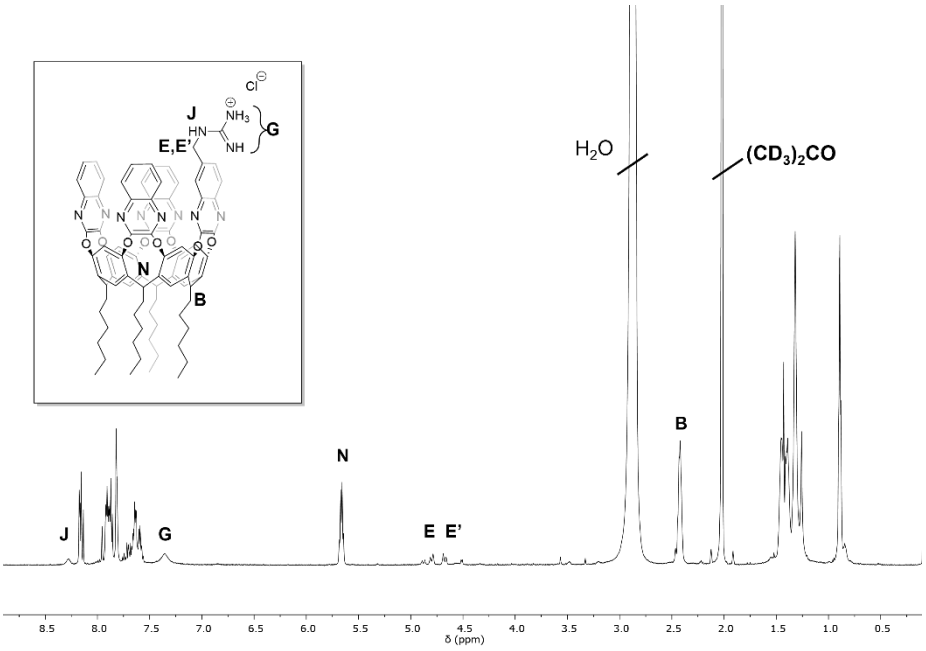

Figure 14. ^{1}HNMR (400 MHz, acetone-d_6, 25 °C) of the product **GUAQxCav**.

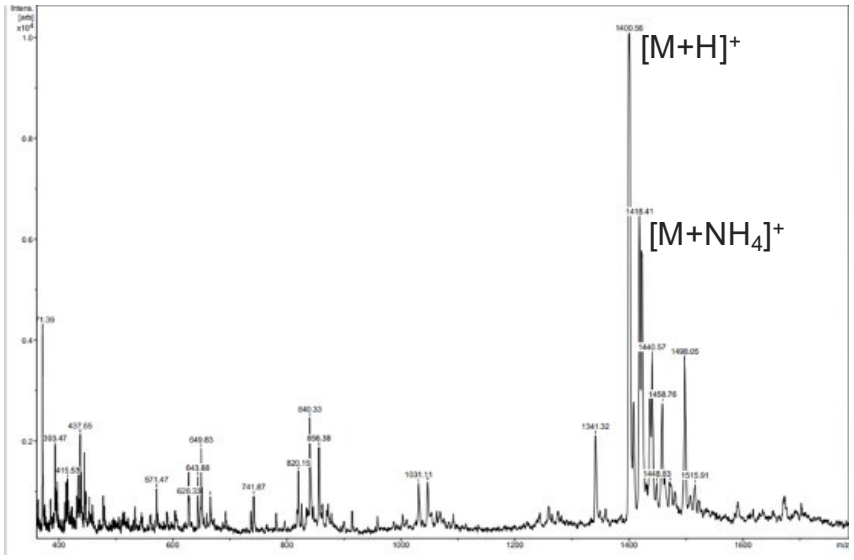

Figure 15. MALDI-TOF (positive ions) of **GUAQxCav**. theoretical m/z: Theoretical $[M+H]^+$: 1400.67 sperimental m/z: 1400.56.

3.2 Synthetic strategy 2

The synthetic strategy to obtain **GUA2QxCav** is described in Figure 16.

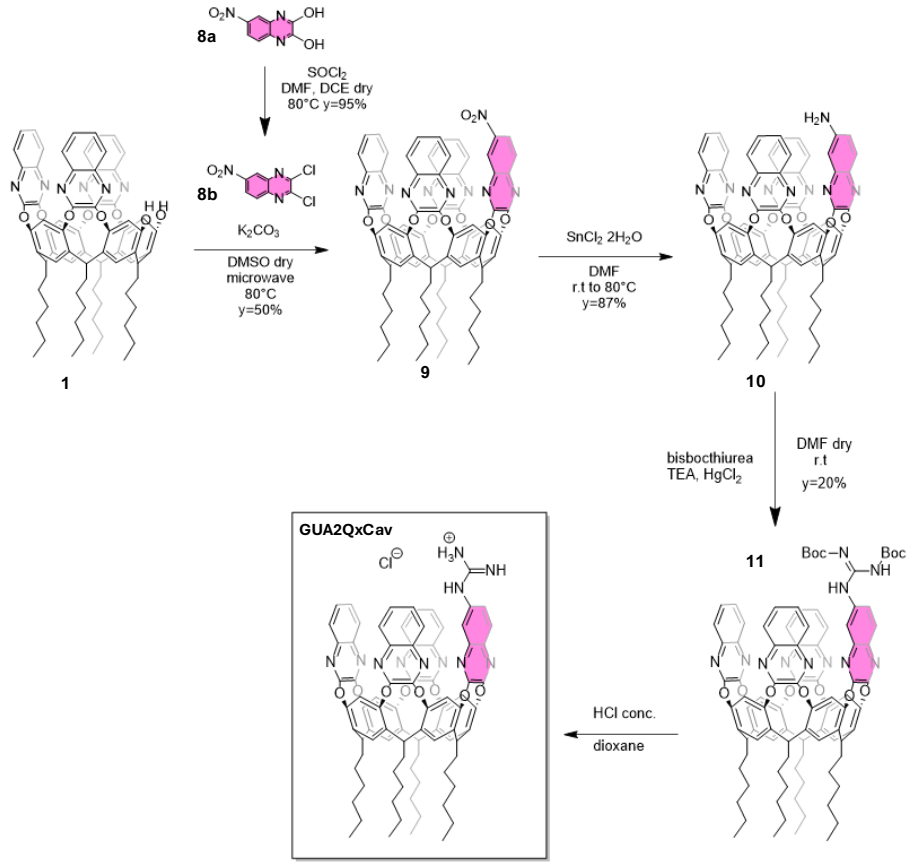

Figure 16. Synthetic pathway for the preparation of **GUA2QxCav**.

Starting from compound **1**, the first step involved a nucleophilic aromatic substitution to give the nitro-functionalized intermediate **9** by reaction with quinoxaline **8b**. Quinoxaline **8b** was obtained by chlorination of quinoxaline **8a** following the protocol already present in the literature[23]. The reaction was performed using microwave irradiation, which allows to lower the reaction time. The intermediate **9** was purified with flash column chromatography with a yield of 50% and characterized by NMR spectroscopy and mass spectrometry.

Subsequently, the aromatic nitro-group located of the upper rim of cavitand **9** was reduced with $SnCl_2 \cdot 2H_2O$ to give intermediate **10** with a yield of 87%. The intermediate **10** was characterized with NMR spectroscopy and mass spectrometry.

The successful reduction was evidenced by the upfield shift of the doublet **A** corresponding to the proton *ortho* to the nitro group, which was previously deshielded at lower field due to the electron-withdrawing effect of the nitro moiety. Furthermore, the formation of the aromatic amine moiety was confirmed by the appearance of a broad singlet at approximately 5.7 ppm: this chemical shift is consistent with literature values for the aromatic amines of quinoxalines[26].

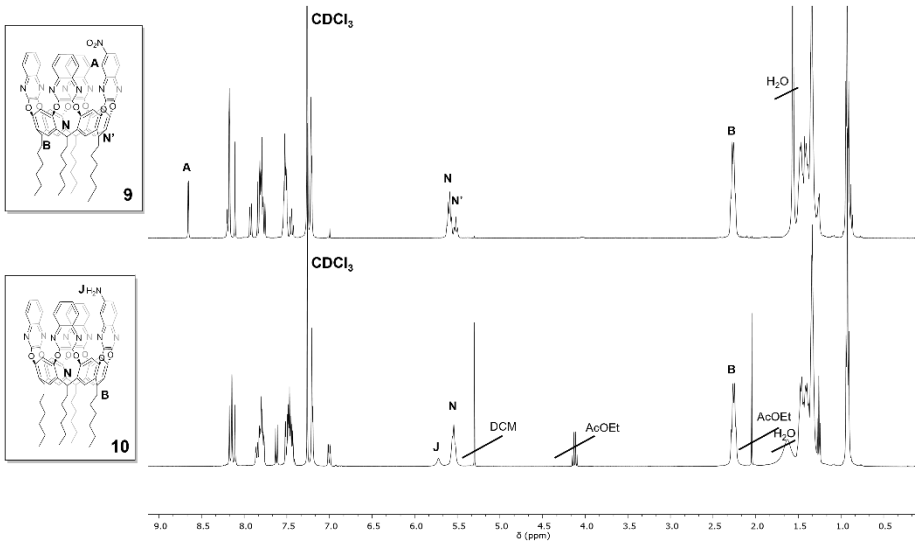

Figure 17. Stacking ^{1}HNMR (400 MHz, $CDCl_3$, 25 °C) of the reactant **9** and the reduced product **10**.

The intermediate **10** was then reacted with bis-bocthiorea, with triethylamine and mercury chloride to give the intermediate **11**, that carries the Boc-protected guanidinium group directly bonded to the upper rim of the cavitand. This

product was purified with flash column chromatography and obtained with a yield of 20%. The proton spectra in deuterated acetone (**Figure 18**) confirmed the presence of the product, in particular the singlets **G** and **F** corresponding to the methyl groups of the Boc groups, the singlets **J** and **K** corresponding to the amine protons of the guanidinium moiety and the upfield of the aromatic proton of the quinoxaline rim **D**, that confirm the functionalisation of the amino group with a more electro-withdrawing moiety.

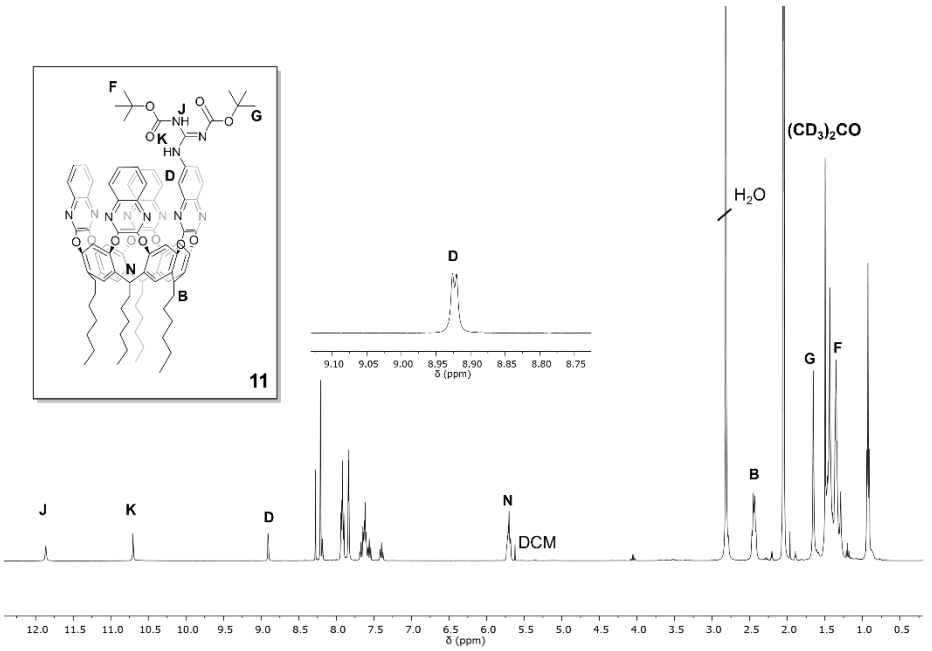

Figure 18. ^{1}HNMR (400 MHz, acetone-d_6, 25 °C) of the intermediate **11**.

The deprotection of the intermediate **11** to obtain the final molecule **GUA2QxCav** is currently ongoing in our research group.

4. Conclusions

In this chapter, we detailed the synthetic approach toward two quinoxaline-based cavitands functionalized with a guanidinium moiety to target anionic surfactants.

The synthesis of the second target cavitand **GUAQxCav**, where the guanidinium group is separated from the quinoxaline wall by a methylene spacer, was successfully completed. This compound was isolated in a satisfactory 65% of yield and thoroughly characterized by means of NMR spectroscopy and mass spectrometry confirming the structural integrity of the macrocycle. Given the prominent role of guanidinium receptors in host-guest chemistry and the established utility of quinoxaline cavitands as selective binding scaffolds, the synthesized molecule represents a highly promising candidate for supramolecular applications. By contrast, the second target compound **GUA2Qx**, featuring the guanidinium group directly coupled to the quinoxaline panel, proved synthetically challenging. The key step involving the formation of the Boc-protected precursor is currently under studying in our research laboratory. Effort focused on optimizing the final deprotection conditions necessary to liberate the cationic guanidinium group are currently underway in our laboratory.

We are currently engaged in evaluating the molecular recognition properties of **GUAQxCav**, focusing specifically on its binding capacity towards various anionic surfactants in solution. These studies are crucial for understanding the effect of the introduced positively charge guanidinium moiety on the overall binding mechanism and will lay the groundwork in selective extraction or anionic surfactants. Further work will focus on overcoming the synthetic challenges associated with the second target to allow for a direct comparison of the binding characteristics of these two distinct charged cavitands.

5. Experimental Part

Materials and methods

All substances were purchased from certified commercial sources and used as received, without further purification. The solvents designated as anhydrous are treated according to procedures well-established in the literature.

NMR spectra, including ^{1}H, COSY, ^{13}C, DEPT135, and HSQC, were recorded on a Bruker AVANCE 400 MHz or on a Jeol 600 MHz spectrometer using $CDCl_3$, DMSO-d_6, or acetone-d_6 as solvents.

All chemical shifts (δ) are reported in parts per million (ppm), referenced either to the residual proton resonances from incomplete deuteration of the NMR solvents or to the solvent's ^{13}C resonance. The abbreviations: s, d, dd, t and m indicate the spectrum peaks referred to: singlet, doublet, doublet of doublets, triplet and multiplet, respectively. The b that eventually precedes the abbreviations means broad.

Electrospray ionization mass spectrometry (ESI-MS) analyses were performed using either an Infusion Waters Acquity Ultra Performance LC HO6UPS-823M instrument equipped with an electrospray ionization (ESI) source operating in positive mode or an Agilent 1260 Infinity II system with an ESI source also configured in positive mode.

Gas chromatography-mass spectrometry (GC-MS) analyses were conducted using an Agilent Technologies 6890N Network GC System, ensuring precise and reliable performance.

Ultra-high-performance liquid chromatography-high-resolution mass spectrometry (UHPLC-HRMS) analyses were performed using a Phenomenex Luna Omega PS C18 column.

5.1 Synthetic strategy 1

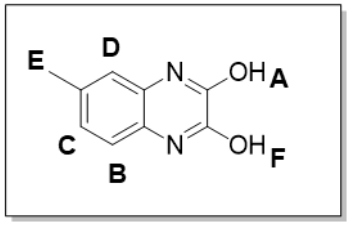

Synthesis of 2,3-dihydroxy-6-methylquinoxaline **2**: 3,4-diaminotoluene (3.00 g, 24.0 mmol. 1.0 eq.) and oxalic acid (2.65 g, 29.0 mmol, 1.2 eq.) were dissolved in 45 mL of HCl 4N. The mixture was heated under stirring at for hours, after which the formation of a gray precipitate was observed. The suspension was allowed to cool to ambient temperature, and the solid was filtered and washed with water until the washings were neutral. The product was obtained as a grey solid in quantitative yield.

^{1}H NMR (400 MHz, DMSO-d_6, 25 °C): δ 11.87 (s, 1H, H_A), 11.84 (s, 1H, H_F) 7.01 (d, J = 8.0 Hz, H_B), 6.93-6.86 (m, 2H, H_C e H_D), 2.27 (s, 3H, H_E). ^{13}C NMR (DMSO-d_6): δ 155.10, 154.47, 142.21, 130.10, 128.69, 124.05,117.70,111.60,20.31.

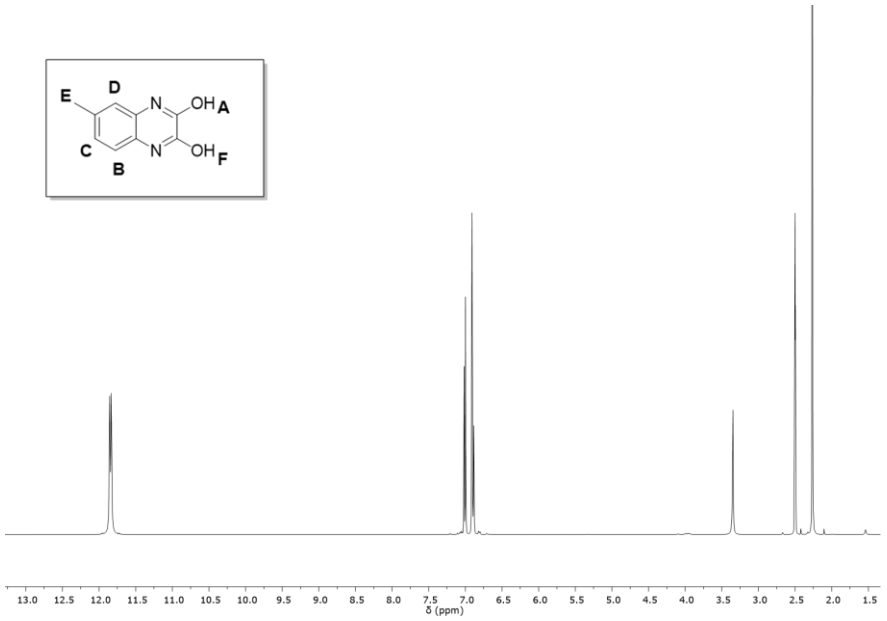

Figure 19: ^{1}HNMR (400 MHz, CDCl3, 25 °C) of 2,3-dihydroxy-6-methylquinoxaline **2**.

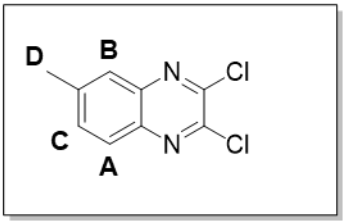

Synthesis of 2,3-dichloro-6-methylquinoxaline 3: under anhydrous conditions, quinoxaline **2** (600.0 mg, 3.41 mmol, 1.0 eq.) was dissolved in 3mL of DMF. Then, $POCl_3$ (3 mL, 32.08 mmol, 9.4 eq.) was added, and the mixture was heated under stirring until disappearance of the reagent. The mixture was then allowed to cool to ambient temperature, then water was added to hydrolyze the residual $POCl_3$ and the solvent was evaporated under reduced pressure. The resulting solid was washed with water, filtered, and extracted with and water. After removing the solvent from the organic phase, quinoxaline **2** was obtained as a white solid with a 91% yield.

^{1}H NMR (400 MHz, $CDCl_3$, 25 °C): δ ppm = 7.92 (d, 1H, H_A, J = 8.6 Hz), 7.80 (s, 1H, H_B), 7.64 (dd, J = 8.6 Hz, 1.9 Hz, 1H, H_C,), 2.60 (s, 3H, H_D). ^{13}C NMR (DMSO-d_6) d 144.27, 143.39, 142.33, 139.97, 138.34, 133.72, 127.30, 126.54, 21.30.
GC-MS $[M + H]^+$ $(C_9H_9N_2O_2)^+$ theoretical m/z: 177.07 Da, experimental: 177.07 Da.

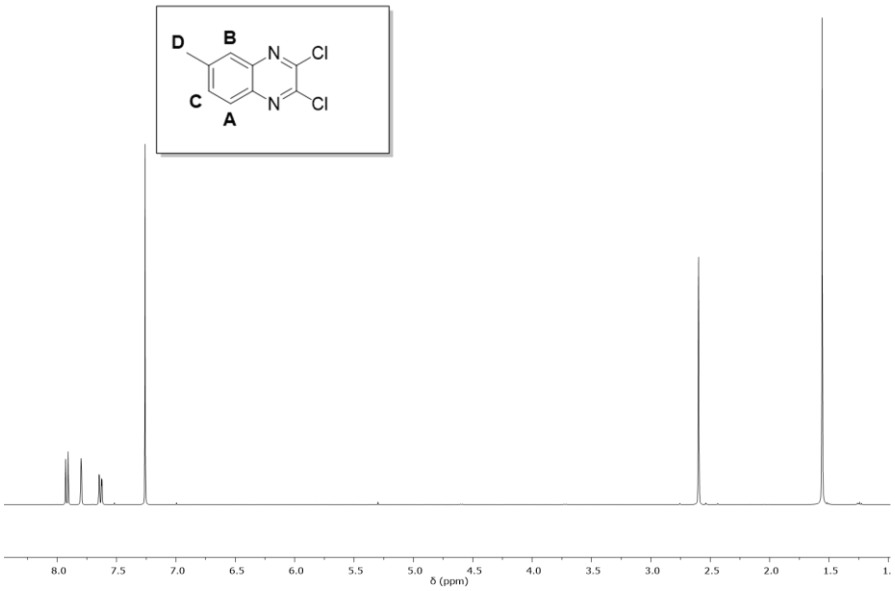

Figure 20: ^{1}HNMR (400 MHz, $CDCl_3$, 25 °C): of 2,3-dichloro-6-methylquinoxaline **3.**

Synthesis of 2,3-dichloro-6-bromo-methylquinoxaline 4: In a microwave reactor, 2,3-dihydroxy-6-methylquinoxaline (300 mg, 1.70 mmol, 1eq) and NBS (275mg, 1.55 mmol, 0.907 eq) are dissolved in 10 mL of acetonitrile. Then, a catalytic amount of AIBN is added and the reaction vessel is placed inside the LED reactor and allowed to react, under stirring, for a couple of hours, monitoring the progress by TLC using hexane/ethyl acetate 11:1 as the eluent. The reaction is quenched with water, and the precipitate is filtered on a Büchner funnel. 360 mg of crude product are obtained.

^{1}H-NMR ($CDCl_3$, 400 MHz, 25°C): δ ppm= 8.02 (d, 1H, H_B), 8.01 (bs, 1H, H_A), 7.84 (dd, 1H, H_D, J=8.6, 2,1 Hz), 4.66 (s, 2H, H_C).

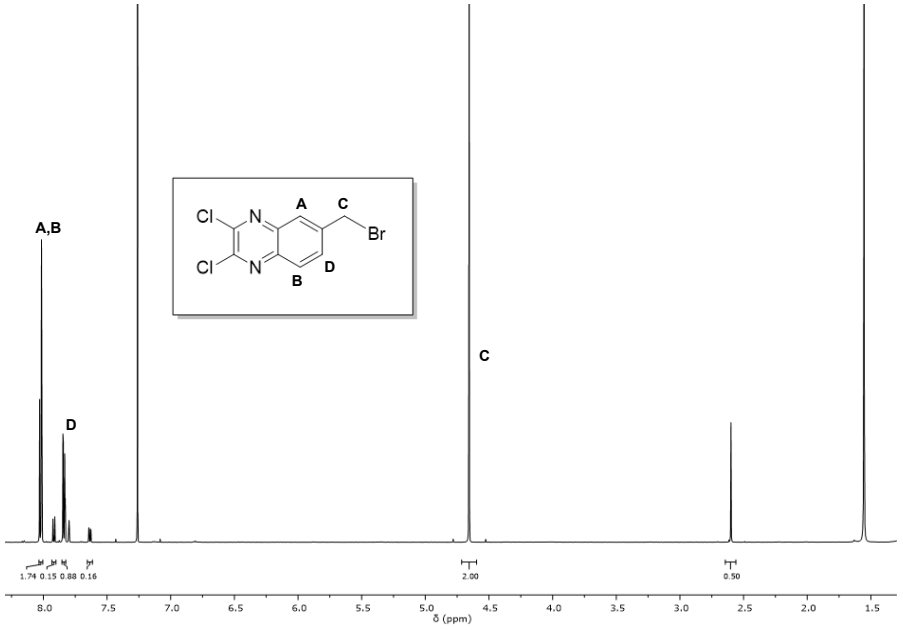

Figure 21: ^{1}HNMR (400 MHz, $CDCl_3$, 25 °C) of the crude of the mixture of **3** and **4**.

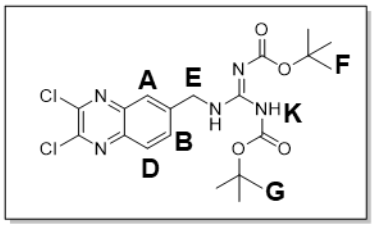

Synthesis of 2,3-dichloro-6-bis-Boc-guanidin-methylquinoxaline 5: a solution of bis-Boc guanidine (457 mg, 1.76 mmol, 1 eq) with NaH (25.7 mg, 9.7 mmol, 1 eq) in 6 mL of dry DMF is added dropwise to a solution of 2,3-dichloro-6-bromo-methylquinoxaline **4** (468 mg, 1.60 mmol, 1 eq) dissolved in 12 mL of dry DMF. The reaction was monitored by TLC using Hex:AcOEt 9:1 as the eluent. Once the reaction reached complete conversion, organic phase is extracted with ethyl acetate, washed with water to remove DMF and dried with sodium sulphate.

The crude product was purified by gradient column chromatography using hexane/ethyl acetate 9:1 as the initial eluent to separate the quinoxaline **3** then switching to 8:2. The product is isolated as a light green solid (692 mg, 92%).

^{1}H-NMR ($CDCl_3$, 600 MHz, 25°C): δ ppm= 9.53 -9.32(bs, 1H, H_K), 7.98(d, 1H, H_B, J=8.6 Hz), 7.84 (bs, 1H, H_A), 7.72 (dd, 1H, H_D, J=8.7, 2.0 Hz), 5.40 (bs, 2H, H_E, J=32,3 Hz), 1.48 (s, 9H, H_F), 1.30 (s, 9H, H_G).

^{13}C NMR ($CDCl_3$, 600 MHz, 25°C): δ 154.46, 145.65, 145.12, 140.51, 139.71, 130.70, 128.07, 125.11, 47.53, 28.26, 27.86.

ESI-MS positive ions, theoretical m/z: 470.14 $[M+H]^+$ $(C_{20}H_{25}Cl_2N_5O_4)^+$; 492.12 $[M+Na]^+$ $(C_{20}H_{25}Cl_2N_5O_4Na)^+$; 963.36 $[2M+Na]^+$ $(C_{40}H_{50}Cl_4N_{10}O_8Na)^+$; Experimental (MeOH) m/z: 470.2 $[M+H]^+$; 492.2 $[M+Na]^+$; 963.4 $[2M+Na]^+$

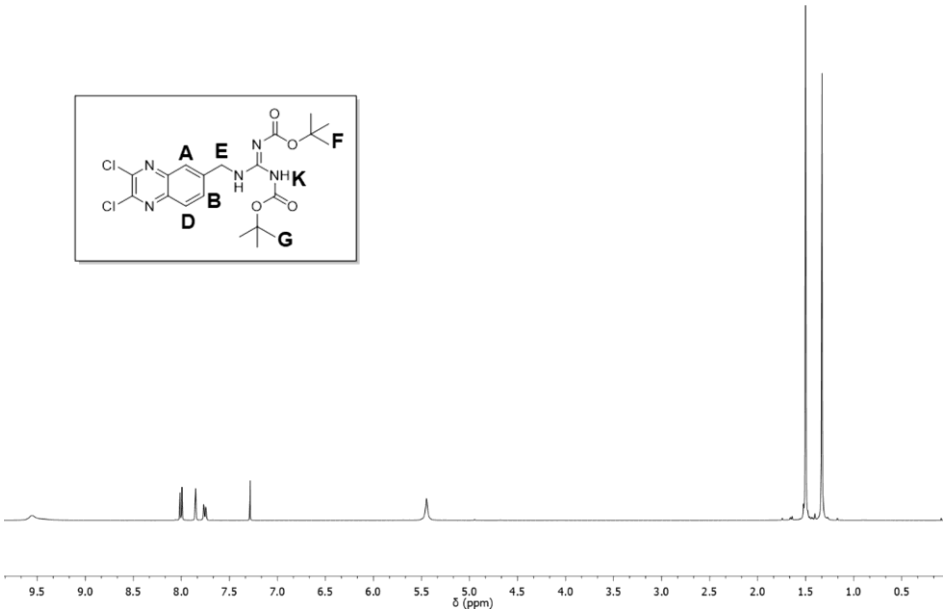

Figure 22: ^{1}HNMR (400 MHz, $CDCl_3$, 25 °C) 2,3-dichloro-6-bis-Boc-guanidin-methylquinoxaline **5.**

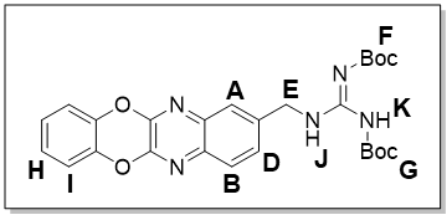

Synthesis of 2,3-catechol-6-bis-Boc-guanidin-methylquinoxaline 5a: Under argon conditions, catechol (12 mg, 0.11 mmol, 1eq) and K_2CO_3 (29mg, 0.21 mmol, 1eq) were solubilized in 6mL of

anhydrous DMSO, followed by the addition of 2,3-dichloro-6-bis-Boc-guanidin-methylquinoxaline (50 mg, 0.11 mmol, 1 eq). The reaction was monitored by TLC using hexane/ethyl acetate, quenched with water and extracted with DCM. The crude product was purified by column chromatography using hexane/ethyl acetate 8:2 as the eluent. The purification afforded 36 mg of product corresponding to a yield of 67%.

^{1}H-NMR ($CDCl_3$, 600 MHz, 25°C): δ ppm= 9.52 (s, 1H, H_J), 9.33 (s, 1H, H_K), 7.74 (d, 1H, H_B, J=1.6 Hz), 7.63 (bs, 1H, H_A), 7.51 (dt, 1H, H_D, J=8.5, 1.9 Hz), 7.12 (m, 2H, H_H), 7.08 (m, 2H, H_I,), 5.34 (s, 2H, H_E), 1.49 (s, 9H, H_F,), 1.32 (s, 9H, H_G).

^{13}C NMR ($CDCl_3$, 600 MHz, 25°C) δ 163.77, 160.82, 154.84, 145.04, 144.74, 140.54, 140.45, 139.04, 138.18, 128.37, 127.18, 125.35, 125.31, 124.95, 117.28, 84.52, 79.14, 47.40, 28.38, 27.95.

ESI-MS positive ions, theoretical m/z: 530.20 $[M+Na]^+$ $(C_{26}H_{29}N_5O_6Na)^+$; 1037.47 $[2M+Na]^+$ $(C_{32}H_{58}N_{10}O_{12}Na)^+$. Experimental (MeOH) m/z: 530.3 $[M+Na]^+$; 1037.6 $[2M+Na]^+$.

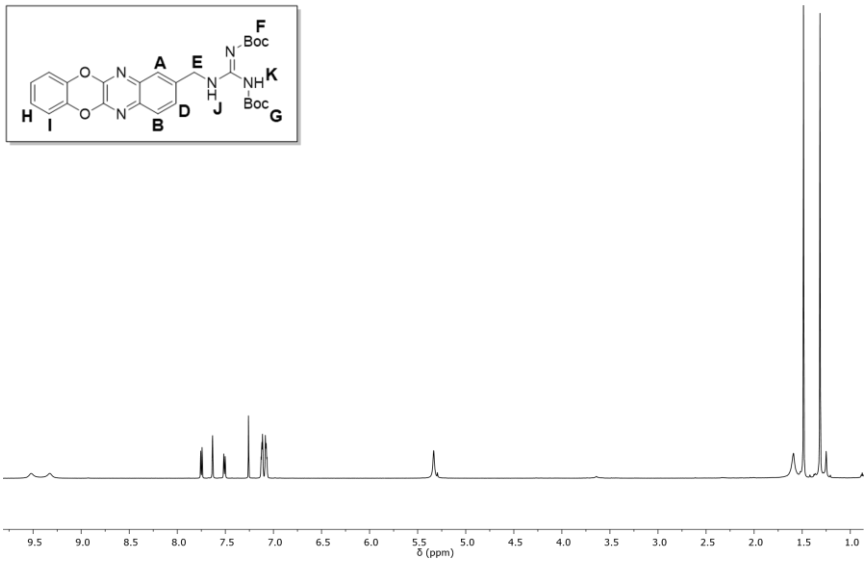

Figure 23: ^{1}HNMR (400 MHz, $CDCl_3$, 25 °C) of 2,3-catechol-6-bis-Boc-guanidin-methylquinoxaline **5a.**

Synthesis of 2,3-Catechol-6-(guanidinomethyl)quinoxaline **5b**:

Synthetic Strategy 1: Deprotection with $SnCl_4$

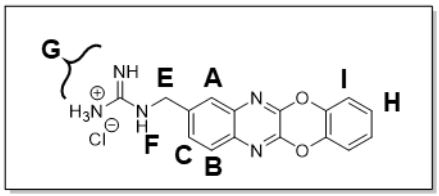

To a solution of 2,3-catechol-6-bis-Boc-guanidine-methylquinoxaline **5a** (50 mg, 0.0985 mmol, 1 eq.) in of ethyl acetate (65 mL) $SnCl_4$ (0.5 mL, 394 µmol, 4 eq.) was added. The reaction was monitored by using a gradient eluent (Hex/AcOEt 8:2 and DCM/MeOH 95:5). Upon completion, the solvent was removed *in vacuo* using a rotary evaporator. The resulting product was subsequently precipitated as a white solid using a mixture of MeOH/Diethyl ether and filtered via a Büchner funnel. The product was isolated as a white solid (22 mg, y=65%). ESI-MS positive ions, theoretical $[M+K]^+$: 346.96 m/z, experimental 346.1 m/z.

^{1}H NMR (600 MHz, Acetone-d_6, 25°C) δ 7.89-7.83 (broad triplet, 1H, H_F), 7.82 – 7.77 (m, 2H, H_A e H_B), 7.65 (dd, 1H, H_C, J=8.5, 1.9 Hz), 7.25 (bs, 4H, H_G), 7.18 (m, 4H, $H_{H,I}$), 4.86 (s, 2H, H_E).

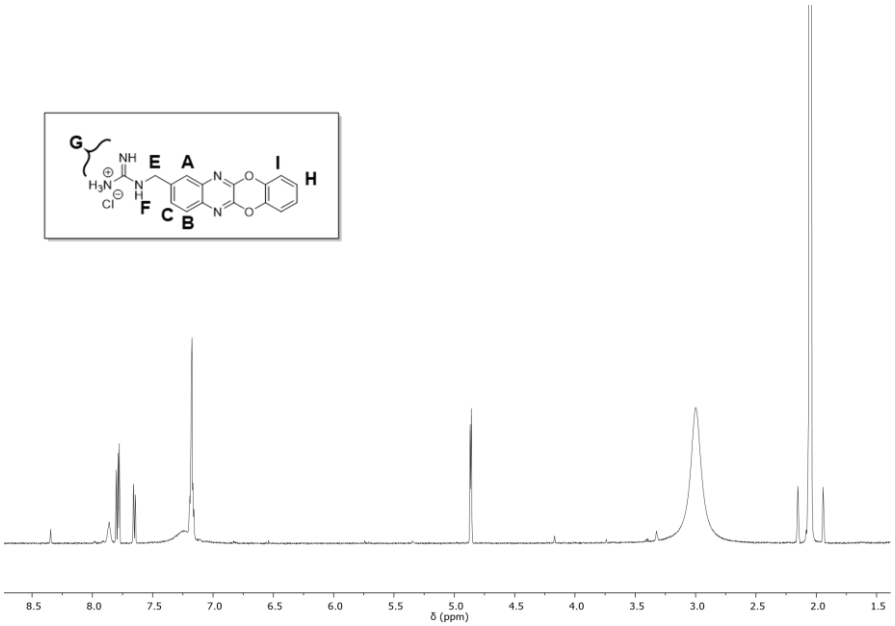

Figure 24: ^{1}HNMR (400 MHz, acetone-d_6, 25 °C) of quinoxaline **5b**.

Deprotection reaction with concentrated HCl in Dioxane*

To a solution of 2,3-catechol-6-bis-Boc-guanidine-methylquinoxaline (X) (76 mg, 0.150 mmol, 1eq, $5x10^{-3}$) in dioxane (5 mL), HCl 1 M (1 mmol per Boc group) was added. The solution was left to stir at room temperature for 24 hours. The dioxane was evaporated *in vacuo* using a rotary evaporator. The resulting solid was then dissolved in ethanol, precipitated in diethyl ether, and weighed. Proton NMR analysis indicated the cleavage of the ethereal bond between the quinoxaline aromatic fraction and the catechol moiety.

**Note: This synthetic procedure did not yield the desired product.*

Synthesis of compound 1. In anhydrous conditions, 500 mg (0.376 mmol) of QxCav is suspended in 80 mL of DMF. CsF (1.14 g, 7.52 mmol) is added to the suspension, and the resulting mixture is stirred and heated at 80 °C. Separately, pyrocatechol (45.5 mg, 0.414 mmol) solubilized in anhydrous DMF (20 mL) is added dropwise to the reaction mixture. The reaction mixture is maintained at 80 °C under continuous stirring for an additional 30 min. The mixture is then poured into 500 mL of ice-cold saturated aqueous NaCl solution, a white precipitate is formed. The suspension is filtered to separate the solid, which is washed with water and purified by flash chromatography using a gradient elution from pure DCM to DCM-EtOAc (95:5). After solvent evaporation, 270 mg (0.376 mmol, 60 % yield) of pure **1** is obtained as a white solid. The NMR analysis is in accordance with the literature[22].

^{1}H NMR (400 MHz, $CDCl_3$, 25 °C): δ ppm = 8.27 (s, 2H, H_A), 7.96 (dd, 2H, H_B, J = 8.3, 1.4 Hz), 7.85 (m, 2H, H_C), 7.71 (dd, 2H, H_D, J = 8.4, 1.4 Hz), 7.59 (m, 2H, H_E), 7.51 (m, 4H, H_F e H_G), 7.28 (s, 2H, H_H), 7.16 (s, 2H, H_I), 7.11 (s, 2H, H_J), 5.62 (t, 1H, H_K, J = 8.1 Hz), 5.54 (t, 2H, H_L, J = 8.1 Hz), 4.29 (t, 1H, H_M, J = 7.7 Hz), 2.26 (m, 8H, H_N), 1.34 (m, 32H, H_O, H_P, H_Q e H_R), 0.93 (m, 12H, H_S).

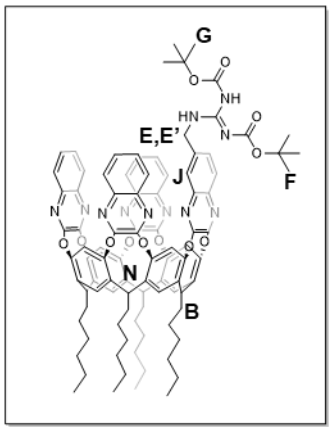

Synthesis of cavitand 6. The synthetic procedure is adapted from reference[27]. Under argon conditions, compound **1** (202 mg, 168 µmol, 1 eq.) and K_2CO_3 (30 mg, 218 µmol, 1.30 eq) were mixed in dry DMSO under stirring at 60°C . Subsequently, quinoxaline **5** (93 mg., 197 µmol, 1.18 eq.) was added. The mixture was left to react until TLC (eluent 8:2) showed the disappearance of the reagent, then it was quenched with acidic water and the precipitate was filtered using a Büchner funnel. The crude product was purified by flash chromatography with gradient eluent (Hex: AcOEt 9:1 to 8:2), yielding 143 mg of pure product, corresponding to a yield of 53%.

^{1}H NMR (400 MHz, acetone-d_6, 25°C) δ 9.47 (bs, 1H,H_J), 8.23 (s, 1H, Ar-*H*), 8.22 (bs, 2H, Ar-*H*), 8.20 (s, 1H, Ar-*H*), 8.04-7.77 (m, 13H, Ar-*H*), 7.71-7.54 (m, 6H, Ar-*H*), 5.76-5.68 (m,4H,H_N), 5.62 (d, *J* = 16.3 Hz, 1H, H_E), 5.16 (d, *J* = 16.2 Hz, 1H, $H_{E'}$), 2.52-2.40 (m, 8H, H_B), 1.52-1.21 (m, 41H, CH_2-CH_3 alifatic chain + H_G), 1.03 (s, 9H, H_F), 0.92-0.81 (m, 12H,CH_3 alifatic chain).

^{13}C NMR (400 MHz, DMSO-d_6, 25°C) δ ppm 158.58, 153.88, 148.25, 144.87, 129.93, 129.53, 129.06, 127.74, 123.58, 123.23, 118.43, 47.19, 34.44, 32.44, 32.32, 31.60, 28.35, 27.86, 22.67.

ESI-MS $[M+H]^+$ $[C_{96}H_{101}N_{11}O_{12}Na]^+$ 1623.93 found 1623.1 m/z.

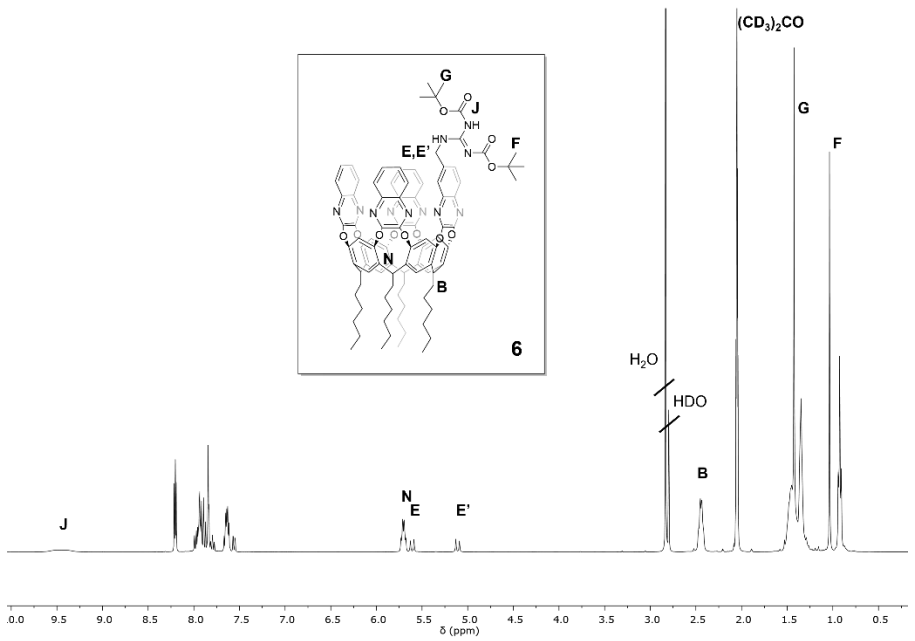

Figure 25: [1]HNMR (400 MHz, acetone-d_6, 25 °C) of cavitand **6**.

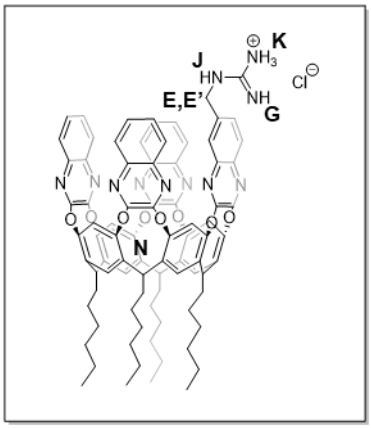

Synthesis of cavitand GUAQxCav. In a flask were placed cavitand 6 (20 mg, 12 µmol, 1 eq) dissolved in 20 mL of AcOEt (conc. 1.2 mmolar). $SnCl_4$ (2.9µL, 6.5 mg, 25µmol, 2 eq.) is added dropwise using an ice bath. The reaction is monitored by TLC using a gradient starting with Hex/AcOEt 8:2, then switching to DCM/MeOH 95:5. The mixture is left to reacting 4 hours. The product was precipitate in ice with a yield of 65% as a white solid.

[1]H-NMR (Acetone d_6, 600 MHz, 25°C): δ ppm= 9.17-9.05 (bs, 1H, H_K), 8.27 – 8.16 (m, 4H, Ar-*H*), 8.00 – 7.82 (m, 11H, Ar-*H* and H_J), 7.79-7.54 (m, 7*H*, Ar-H), 7.42-7.28 (bs, 1H, H_G), 5.70-5.62 (m, 4H, H_N), 4.85 (dd, 1H, H_E), 4.65 (dd, 1H, $H_{E'}$), 2.61-

2.35 (m, 8H, CH_2- $CH_2CH_2CH_2CH_2CH_3$ aliphatic chain), 1.68-1.18 (m, 32H, CH_2-$CH_2CH_2CH_2CH_2CH_3$ aliphatic chain) 1.00-0.78 (m,CH_3 aliphatic chain).
MALDI TOF positive ions, theoretical m/z: 1400.67 $[M+H]^+$; Found m/z: 1400,56 $[M+H]^+$;

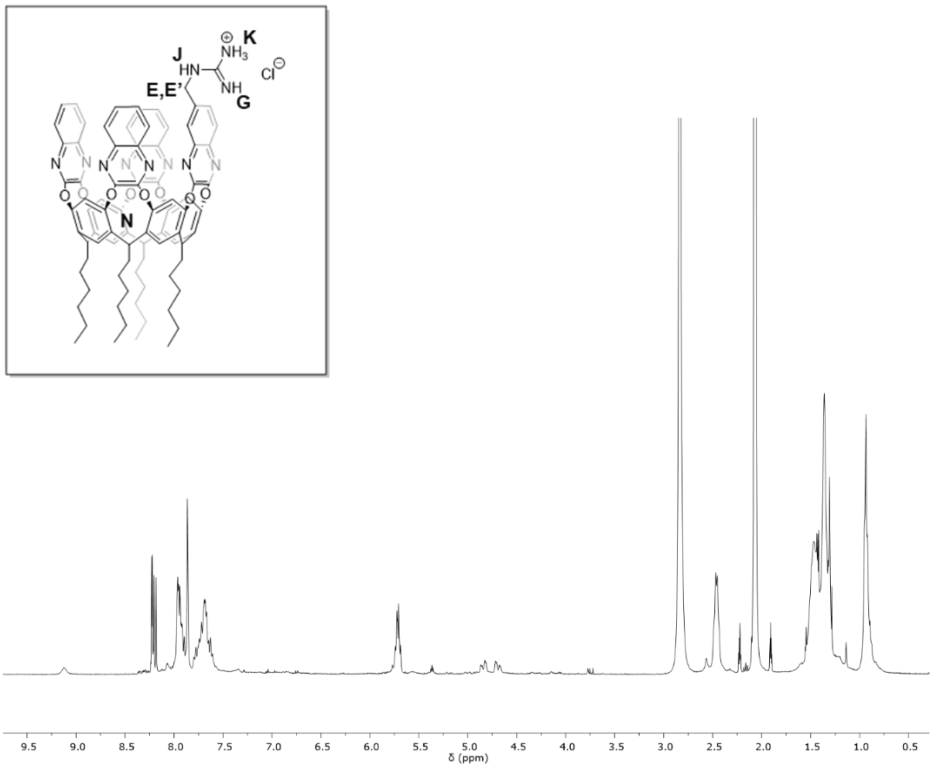

Figure 26: ^{1}HNMR (400 MHz, acetone-d_6, 25 °C) of cavitand **7**.

5.2 Synthetic strategy 2

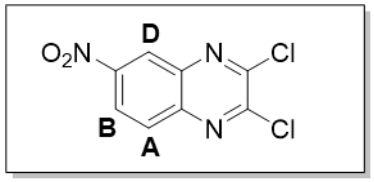

Synthesis of 2,3-Dichloro-6-nitroquinoxaline (8b). Under argon atmosphere, 2,3-dihydroxy-6-nitroquinoxaline (383 mg, 1.85 mmol, 1eq) was solubilized in 5 mL of DCE, then a catalytic amount of DMF dry (2 drops) is added. Then, thionyl chloride (0.935 mL, 10.2 mmol, 5.53 eq.) was added dropwise. After completion of the reaction checked

with TLC (Hex:AcOEt 9:1) the solvent was removed under vacuo. The product was purified by silica gel flash chromatography (eluent Hex:AcOEt 9:1) and obtained as a white solid (y=95%) yield. ^{1}HNMR (DMSO-d_6): 8.21 (d, J=2.4Hz, 1H, H_A), 8.57 (dd, J=9.2, 2.5 Hz, 1H, H_B), 8.28 (d, J=9.2 Hz, 1H, H_D). The proton analysis is in correspondence of the one present in literature[23].

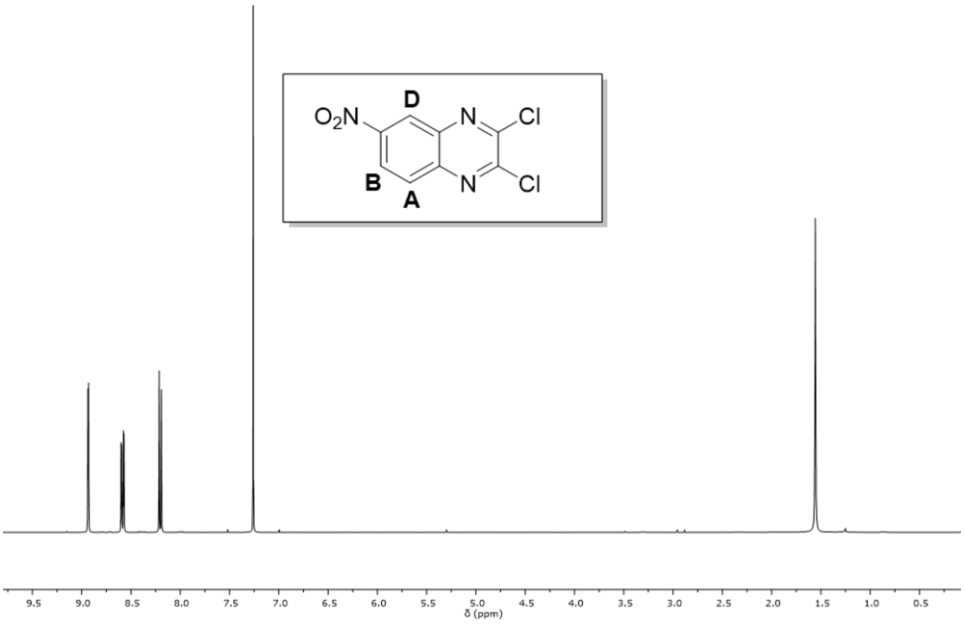

Figure 27: ^{1}HNMR (400 MHz, acetone-d_6, 25 °C) of quinoxaline 8b

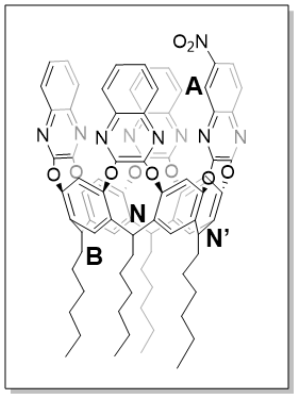

Synthesis of cavitand 11. Under argon conditions, cavitand **1** (257 mg, 214 µmol, 1 eq) and K_2CO_3 (38 mg, 278 µmol, 1.30 eq) were mixed in dry DMSO under stirring at 80°C in a microwave reactor. Subsequently, quinoxaline **8b** (63 mg., 258 µmol, 1.20 eq.) was added. The mixture was left to reacting (80°C, 200 W) until TLC (eluent 8:2) showed the disappearance of the reagent, then it was quenched with acidic water, and the precipitate was filtered using a Büchner

funnel. The crude product was purified by flash chromatography with gradient eluent (Hex: AcOEt 9:1 to 8:2), yielding 147 mg of pure product, corresponding to a yield of 50%.

^{1}H NMR (400 MHz, $CDCl_3$, 25 °C) δ 8.66 (d, *J* = 2.5 Hz, 1H, H_A), 8.21 – 8.15 (m, 3H, Ar-H), 8.11 (s, 1H, Ar-H), 7.92 (dd, *J* = 8.4, 1.4 Hz, 1H, Ar-H), 7.85 – 7.74 (m, 6H, Ar-H), 7.56 – 7.41 (m, 6H, Ar-H), 7.23 – 7.19 (m, 4H, Ar-H), 5.62 (s, 1H), 5.59 (q, *J* = 7.16Hz, 3H, H_N), 5.52 (t, *J* = 8.0 Hz, 1H, $H_{N'}$), 2.37-2.27 (m, 8H, H_B), 1.51 – 1.19 (m, 32H, -$CH_2CH_2CH_2CH_2CH_3$), 0.97 – 0.82 (m, 12H, $CH_2CH_2CH_2CH_2CH_3$). ESI (MS) positive ions, theoretical $[C_{84}H_{79}N_9O_{10}$+MeOH]+: 1407.65 m/z. Found: 1407.03 m/z.

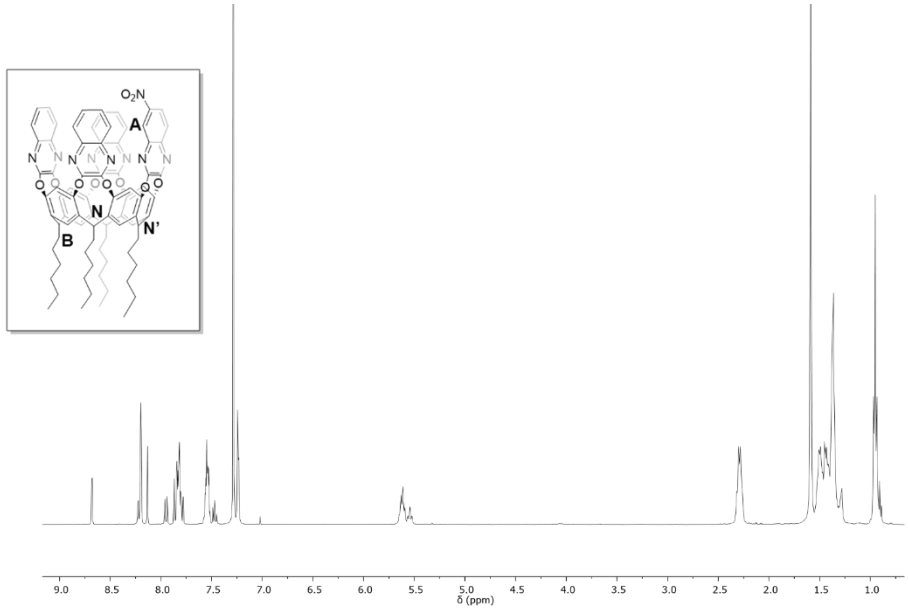

Figure 28: ^{1}H NMR (400 MHz, $CDCl_3$, 25 °C): of cavitand **11**.

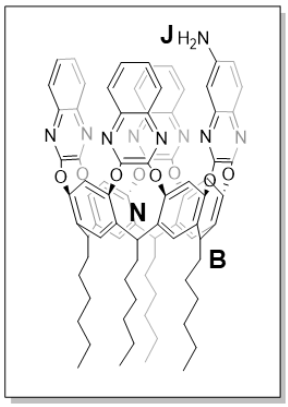

Synthesis of cavitand 12. The synthetic procedure is adapted from reference[28]. Cavitand **11** (59 mg, 43 µmol, 1 eq.) was solubilized in 10 mL of DMF. Then $SnCl_2$ $2H_2O$ (11 mg, 0.47 mmol, 11 eq.) is added. The mixture was left stirring at room temperature and then heated to 80°C until disappearance of the reagent. The reaction is quenched by addition of a solution of sodium bicarbonate 5%. Then, the organic phase was extracted with DCM and washed with distilled water to remove DMF. The product was purified via flash column chromatography (eluent Hex:AcOEt 7:3), that afforded 50 mg of pure product corresponding to a yield of 87%.

^{1}H NMR (400 MHz, $CDCl_3$, 25 °C): δ 8.17 (s, 1H, Ar-H), 8.14 (s, 2H, Ar-H), 8.11 (s, 1H, Ar-H) 7.90 – 7.74 (m, 7H, Ar-H), 7.62 (d, J = 9.0 Hz, 1H, Ar-H), 7.54-7.40 (m, 8H, Ar-H), 7.23-7.16 (m, 4H, Ar-H), 7.00 (dd, J = 9.0, 2.5 Hz, 1H), 5.72 (bs, H_J), 5.61 – 5.48 (m, 4H, H_N), 2.35-2.18 (m, 8H, H_E), 1.54 – 1.22 (m, 32H, -C*H*$_2$C*H*$_2$C*H*$_2$C*H*$_2$CH$_3$), 1.01 – 0.82 (m, 12H, $CH_2CH_2CH_2CH_2CH_3$).

ESI-MS positive ions, theoretical $[C_{84}H_{81}N_9O_8+K]^+$: 1384.59 m/z; Experimental 1384.05 m/z.

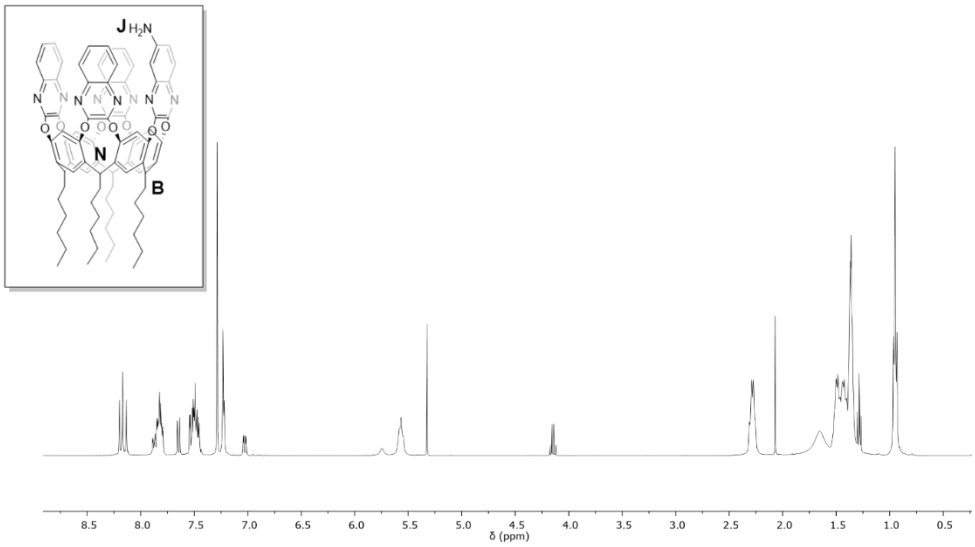

Figure 29: ^{1}H NMR (400 MHz, $CDCl_3$, 25 °C): of cavitand **12**.

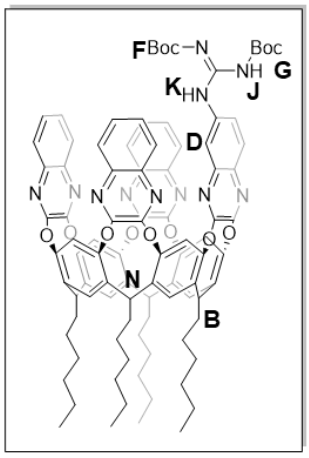

Synthesis of cavitand 13. Under argon conditions, cavitand **12** (33 mg, 24.8 µmol, 1 eq.) is solubilized in 3 mL of dry DMF. Then, mercury chloride (8 mg, 30 µmol, 1.2 eq.) is added, followed by triethylamine (0.01 mL, 71 µmol, 2.9 eq.) and bis-Boc-thiourea (8.21 mg, 30 µmol, 1.2 eq.). The reaction is stirred for two days, then the catalyst is filtered. The organic phase is extracted with DCM, washed with distilled water and dried with sodium sulphate and under vacuum. The product is isolated via flash column chromatography (eluent Hex:AcOEt 7:3) as a light green solid (7 mg, y =20%).

^{1}H NMR (400 MHz, Acetone-d_6, 25°C) δ 11.87 (s, 1H, H_J), 10.70 (s, 1H, H_K), 8.91 (d, *J* = 2.4 Hz, 1H,H_D), 8.27 (s, 1H, Ar-H), 8.22– 8.17 (m, 4H, Ar-H), 7.69-7.52 (m, 6H, Ar-H), 7.87-7.80 (m, 4H, Ar-H), 7.70 – 7.52 (m, 6H), 7.40 (m, 1H, Ar-H), 5.75-5.65 (m, 4H, H_N), 2.44 (q, *J* =

7.8 Hz, 8H, H_B), 1.65 (s, 9H, H_G), 1.53 – 1.25 (m, 41H, H_F+-$CH_2CH_2CH_2CH_2CH_3$) 0.97– 0.87 (t, J= 6.72, 12H, $CH_2CH_2CH_2CH_2CH_3$).

ESI-MS positive ions, theoretical $[C_{95}H_{99}N_{11}O_{12}$-2Boc+H$]^+$: 1388.68 m/z; Experimental (MeOH) 1388.96 m/z.

^{13}C NMR (400 MHz, Acetone-d_6, 25°C) δ 152.41, 152.39, 140.46, 136.35, 136.30, 136.27, 135.93, 129.53, 129.36, 129.12, 128.16, 127.88, 127.64, 124.81, 124.06, 118.57, 118.55, 117.22, 34.32, 31.84, 28.37, 27.42, 22.47, 13.48.

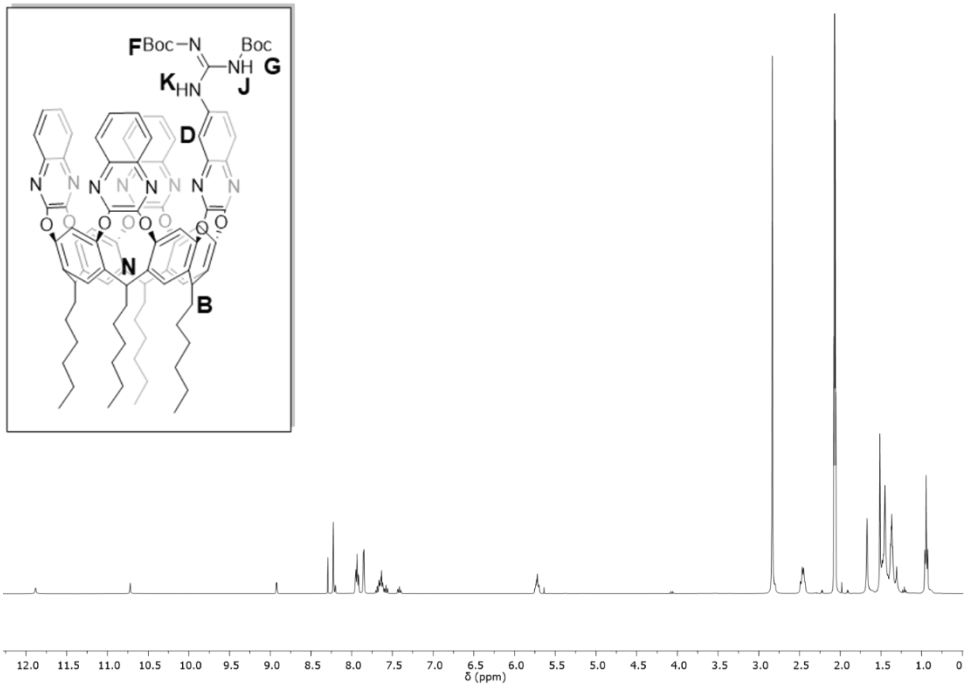

Figure 30: ^{1}H NMR (400 MHz, Acetone-d_6, 25°C) of cavitand **13**.

6. References

[1] Tamjidi, S.; Moghadas, B. K.; Esmaeili, H.; Shakerian Khoo, F.; Gholami, G.; Ghasemi, M. Improving the Surface Properties of Adsorbents by Surfactants and Their Role in the Removal of Toxic Metals from Wastewater: A Review Study. *Process Saf. Environ. Prot.* **2021**, *148*, 775–795. https://doi.org/10.1016/j.psep.2021.02.003.

[2] Beer, P. D.; Gale, P. A. Anion Recognition and Sensing: The State of the Art and Future Perspectives. *Angew. Chem. Int. Ed.* **2001**, *40*, 486–516.https://doi.org/10.1002/1521-3773(20010202)40:3<486::AID-ANIE486>3.0.CO;2-P.

[3] Gregory, K. P.; Wanless, E. J.; Webber, G. B.; Craig, V. S. J.; Page, A. J. The Electrostatic Origins of Specific Ion Effects: Quantifying the Hofmeister Series for Anions. *Chem. Sci.* **2021**, *12*, 15007–15015. https://doi.org/10.1039/D1SC03568A.

[4] Patrick, S. C.; Beer, P. D.; Davis, J. J. Solvent Effects in Anion Recognition. *Nat. Rev. Chem.* **2024**, *8* , 256–276. https://doi.org/10.1038/s41570-024-00584-4.

[5] Mao, L.; Li, G.; Zhang, B.; Wen, K.; Wang, C.; Cai, Q.; Zhao, X.; Guo, Z.; Zhang, S. Functional Hydrogels for Aqueous Zinc-Based Batteries: Progress and Perspectives. *Adv. Mater.* **2024**, 2416345. https://doi.org/10.1002/adma.202416345.

[6] Surina, A.; Čejka, J.; Salvadori, K.; Lhoták, P. Anion Recognition Using Meta - Substituted Ureidocalix[4]Arene Receptors. *Org. Biomol. Chem.* **2024**, *22*, 8669–8678. https://doi.org/10.1039/D4OB01441C.

[7] Gale, P. A. Anion Receptor Chemistry. *Chem. Commun*. **2010**, *47*, 82–86. https://doi.org/10.1039/C0CC00656D.

[8] Moran, J. R.; Karbach, S.; Cram, D. J. Cavitands: Synthetic Molecular Vessels. *J. Am. Chem. Soc.* **1982**, *104*, 5826–5828. https://doi.org/10.1021/ja00385a064.

[9] Bianchi, F.; Pinalli, R.; Ugozzoli, F.; Spera, S.; Careri, M.; Dalcanale, E. Cavitands as Superior Sorbents for Benzene Detection at Trace level *New J. Chem.* **2003**, *27*, 502–509. https://doi.org/10.1039/b210942e.

[10] Rozzi, A.; Pedrini, A.; Pinalli, R.; Cozzani, E.; Elmi, I.; Zampolli, S.; Dalcanale, E. Cavitand Decorated Silica as a Selective Preconcentrator for BTEX Sensing in Air. *Nanomaterials* **2022**, *12*, 2204. https://doi.org/10.3390/nano12132204.

[11] A New, Deep Quinoxaline-Based Cavitand Receptor for the Complexation of Benzene. *Acta Crystallogr. Sect. E Crystallogr. Commun.* **2019**, *75*, e7500103. https://doi.org/10.1107/S2056989018017784.

[12] Moran, J. R.; Ericson, J. L.; Dalcanale, E.; Bryant, J. A.; Knobler, C. B.; Cram, D. J. Vases and Kites as Cavitands. *J. Am. Chem. Soc.* **1991**, *113*, 5707–5714. https://doi.org/10.1021/ja00015a026.

[13] Torelli, M.; Domenichelli, I.; Pedrini, A.; Guagnini, F.; Pinalli, R.; Terenziani, F.; Artoni, F.; Brighenti, R.; Dalcanale, E. pH-Driven Conformational Switching of Quinoxaline Cavitands in Polymer Matrices. *Synlett* **2018**, *29*, 2503–2508. https://doi.org/10.1055/s-0037-1610219.

[14] Frei, M.; Marotti, F.; Diederich, F. ZnII-Induced Conformational Control of Amphiphilic Cavitands in Langmuir Monolayers. *Chem. Commun.* **2004**, No. 12, 1362–1363. https://doi.org/10.1039/B405331A.

[15] Pochorovski, I.; Diederich, F. Development of Redox-Switchable Resorcin[4]Arene Cavitands. *Acc. Chem. Res.* **2014**, *47*, 2096–2105. https://doi.org/10.1021/ar500104k.

[16] Skinner, P. Cheetham, A. Beeby, A. Gramlich, V. and Diederich, F. Conformational Switching of Resorcin[4]arene Cavitands by Protonation, Preliminary Communication *Helvetica Chimica Acta* **2001**,*84:2146-21523*.https://doi.org/10.1002/1522-2675(20010711)84:7<2146::AID-HLCA2146>3.0.CO;2-K

[17] Roncucci, P.; Pirondini, L.; Paderni, G.; Massera, C.; Dalcanale, E.; Azov, V. A.; Diederich, F. Conformational Behavior of Pyrazine-Bridged and Mixed-Bridged Cavitands: A General Model for Solvent Effects on Thermal "Vase–Kite" Switching. *Chem. – Eur. J.* **2006**, *12*, 4775–4784. https://doi.org/10.1002/chem.200600085.

[18] Schneider, H.-J. Hydrogen Bonds with Fluorine. Studies in Solution, in Gas Phase and by Computations, Conflicting Conclusions from Crystallographic Analyses. *Chem. Sci.* **2012**, *3*, 1381–1394. https://doi.org/10.1039/C2SC00764A.

[19] Baldini, L.; Cacciapaglia, R.; Casnati, A.; Mandolini, L.; Salvio, R.; Sansone, F.; Ungaro, R. Upper Rim Guanidinocalix[4]Arenes as Artificial Phosphodiesterases. *J. Org. Chem.* **2012**, *77* , 3381–3389. https://doi.org/10.1021/jo300193y.

[20] Zheng, Z.; Yu, H.; Geng, W.-C.; Hu, X.-Y.; Wang, Y.-Y.; Li, Z.; Wang, Y.; Guo, D.-S. Guanidinocalix[5]Arene for Sensitive Fluorescence Detection and Magnetic Removal of Perfluorinated Pollutants. *Nat. Commun.* **2019**, *10*, 5762. https://doi.org/10.1038/s41467-019-13775-1.

[21] Shi, Q.; Mower, M. P.; Blackmond, D. G.; Rebek, J. Water-Soluble Cavitands Promote Hydrolyses of Long-Chain Diesters. *Proc. Natl. Acad. Sci. USA* **2016**, *113*, 9199–9203. https://doi.org/10.1073/pnas.1610006113.

[22] Castro, P. P.; Zhao, G.; Masangkay, G. A.; Hernandez, C.; Gutierrez-Tunstad, L. M. Quinoxaline Excision: A Novel Approach to Tri- and Diquinoxaline Cavitands. *Org. Lett.* **2004**, *6*, 333–336. https://doi.org/10.1021/ol036045x.

[23] Romer, D.R., Synthesis of 2 3-dichloroquinoxalines via Vilsmeier Reagent Chlorination. *Journal of Heterocyclic Chem* **2009**, 46, 317-319. https://doi.org/10.1002/jhet.56.

[24] Carlos F., M.Ana G., NeoJesùs D., Sonia M.C. A Safe and Green Benzylic Radical Bromination Experiment *J.Chem.Educ.***2020**,97,2,582585.https://pubs.acs.org/doi/10.1021/acs.jchemed.9b00020.

[25] Cantillo, D.; De Frutos, O.; Rincon, J. A.; Mateos, C.; Kappe, C. O. A Scalable Procedure for Light-Induced Benzylic Brominations in Continuous Flow. *J. Org. Chem.* **2014**, *79*, 223–229. https://doi.org/10.1021/jo402409k.

[26] Kasparian, A. J.; Savarin, C.; Allgeier, A. M.; Walker, S. D. Selective Catalytic Hydrogenation of Nitro Groups in the Presence of Activated Heteroaryl Halides. *J. Org. Chem.* **2011**, *76*, 9841–9844. https://doi.org/10.1021/jo2015664.

[27] S. Y. Ko, J. Lerpiniere, A. M. Christofi. *An Efficient Synthesis of Internal Guanidines.* **1996** *ChemInform Wiley Online Library*. 27: no-no. https://doi.org/10.1002/chin.199602254.

[28] Bellamy, F. D.; Ou, K. Selective Reduction of Aromatic Nitro Compounds with Stannous Chloride in Non Acidic and Non Aqueous Medium. *Tetrahedron Lett.* **1984**, *25*, 839–842. https://doi.org/10.1016/S0040-4039(01)80041-1.

Chapter 3

"Synthesis of functionalized sulfopillar[6]arene for grafting on silica nanoparticles"*

*Part of this activity has been carried out during my secondment in professor Hof's group at University of Victoria.

1. Introduction

1.1 Post-translational modification (PTMs)

Biologically relevant post-translational modifications of proteins (PTMs) are acetylation, methylation, phosphorylation, and ubiquitination after their translation has occurred in ribosomes (Figure 1). PTMs are often observed many proteins, they can be reversible or irreversible and act as molecular switches and signals that fine-tune protein structure and function across a variety of biological contexts such as gene expression, DNA repair, and cell cycle regulation[1,2].

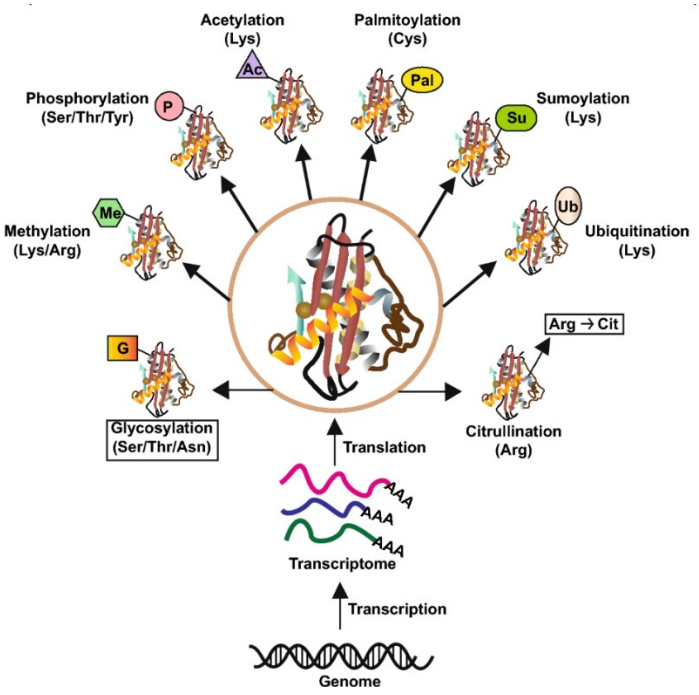

Figure 1. The most frequent post-translational modification of proteins[3].

Histones are cationic proteins that form complexes with anionic DNA to form chromatin in eukaryotic cells. The structure and dynamics of chromatin are greatly influenced by histone tails, which are very rich in lysines and arginines. Lysine (K, Lys) and arginine (R, Arg) methylation play a crucial role

in gene regulation, epigenetic inheritance and other cellular processes associated with complex pathologies, including cancer and neurodegenerative disorders[4].

Selective recognition of these modifications is therefore of great interest. Currently, mass spectrometry represents the gold standard for detecting these modifications, particularly using high-resolution instruments such as Orbitrap and Q-TOF. This approach enables the identification of specific methylated residues by analysing the peptide fragments generated after enzymatic digestion of histones.

Moreover, this method provides not only the localisation of the modified sites but also the exact methylation state, including mono-, di-, or trimethylation of lysine as well as mono-methylation, asymmetrical and symmetrical demethylation of arginine.

The addition of a methyl group on the side chain of these amino acids affects both the steric hindrance and the electronic distribution of the amino group. These subtle chemical changes lead to an increase of its hydrophobicity and change its ability to form hydrogen bonds, determinants of the interaction of histone tails with other proteins and chromatin-associated factors leading to a cascade reaction with implications in human diseases such as cancer, schizophrenia and diabetes.

However, the antibodies used for detection of methylated lysine or arginine are expensive, unstable and show low batch to batch reproducibility[5]. In this context, supramolecular chemistry offers an efficient and cost-effective way to surmount these challenges. The synthetic design of macrocycles that interact with methylated states of lysine and arginine is inspired by molecular reader proteins. These proteins are characterized by an aromatic cage that is able to recognize the methylated residues through cation-π interaction and H-bonds with the cationic carbocation and secondary interactions with the peptide

backbone. Understanding these natural mechanisms has inspired the design of synthetic receptors capable of mimicking such interactions, acting like "artificial antibodies" for the selective recognition of histone PTMs.

Among the explored supramolecular systems, macrocycles have proven particularly effective due to their preorganized architectures and the possibility of fine-tuning cavity size, shape, and functionalization to enhance water solubility, stabilize the receptor-amino acid complex, and potentially engage secondary interactions with neighbouring residues in the peptide[6].

Notably, cucurbiturils, calixarenes, pillararenes, and cavitands have demonstrated the ability to complex methylated residues, showing both affinity and, in some cases, selectivity for specific methylation states[7].

1.2 Complexation of methylated amino acids with pillar[6]arene

Pillar[n]arenes (P[n]s), introduced by Ogoshi and coworkers in 2008[8], are constituted by hydroquinone units linked by methylene bridges at para positions. Their synthesis is based on the acid catalysed cyclisation of hydroquinone ethers with paraformaldehyde (Figure 2).

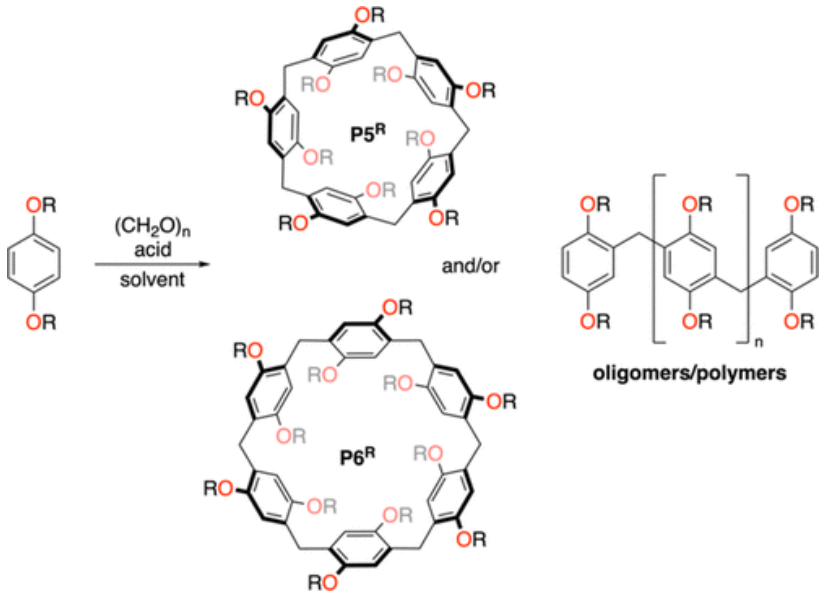

Figure 2. General synthesis of pillar[5]arene and\or pillar[6]arene with the structure of possible oligomeric or polymeric side products. R= alkyl group[9].

In particular, the synthesis of pillar[5]arene[10] is achieved with the yield of 71% by condensation of 1,4 dimethoxybenzene and paraformaldehyde in the presence of $BF_3O(C_2H_5)_2$ using methylene chloride (DCM) or dichloroethane (DCE) as reaction solvent.

There are several synthetic methods for obtaining pillar[6]arene: I) solvent-free conditions[11], II) using deep eutectic solvents[11], III) employing polar solvents

like acetonitrile for template cyclization[13], and IV) using chloroform as a template in combination with either a Brønsted or Lewis acid. However, not only these methods were not scalable but in most of the cases both pillar[5]- and pillar[6]arene are obtained, requiring a separation by column chromatography. Recently Hof's group published a paper[14] describing a method to synthetize exclusively ethoxypillar[6]arene using BF_3OEt_2 as catalyst and chlorocyclohexane as templating agent. The synthesis leads to the formation of oligomers and ethoxypillar[6]arene that can be obtained pure with a yield of 34% with a simple precipitation.

P[n]s have immediately garnered a lot of interest in host-guest chemistry because they can include complex neutral species in organic solutions and possess a more rigid and symmetrical structure compared to those of calix[n]arenes. In contrast to other non-aromatic macrocycles, such as cucurbiturils, they are readily soluble in organic solvents and are relatively simple to functionalize with various substituents, selectively on one, two, or all of the aromatic units.

The cavity of pillarenes can vary ranging from 4.7 Å for P[5], 7.5 Å for P[6] (Figure 3)[15], and 8.2 Å for P[7], depending on the number of constituent monomers. The cavity size of pillar[6]arene (7.5 Å) has almost equal size to those of cucurbit[7]uril (7.3 Å) and γ-cyclodextrin (7.5 Å), for these reasons their scope in host-guest chemistry has attracted a lot of attention.

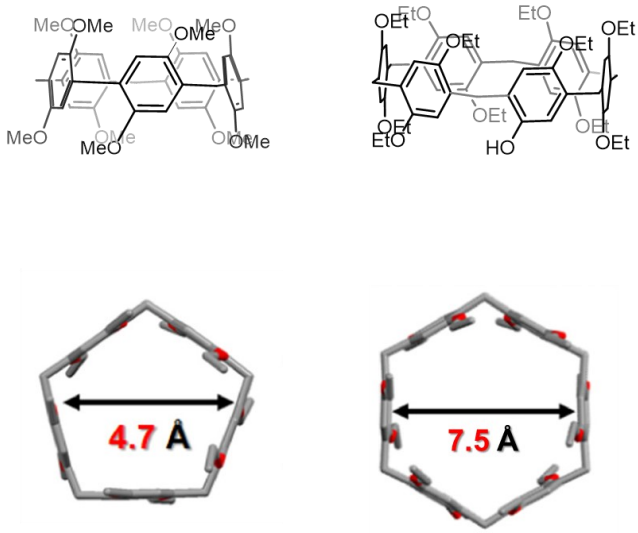

Figure 3. Chemical structure (top) and crystal structure (bottom) of pillar[5]arene and pillar[6]arene. Figure adapted from reference[15].

In 2013 Jian Li and Xueshun Jia's groups[16] showed the host-guest recognition properties of a novel, negatively charged carboxylatopillar[5]arene (CP5A), in an aqueous solution (Figure 4).The authors investigated its binding selectivity towards various native L-α-amino acids, and related metabolites included trimethyl-lysine using ^{1}H NMR spectroscopy and isothermal titration calorimetry (ITC). CP5A shows binding abilities towards basic amino acids such as Lys and Arg, with association constants of (1.8±0.2) $\times 10^{3}$ M^{-1} and (5.9±0.4) $\times 10^{3}$ M^{-1} respectively. The driving forces for the binding are electrostatic interactions between the negatively charged carboxylate groups of the host and the cationic side chains of amino acids. Instead, the affinity towards trimethyl-lysine is lower due to the steric hindrance of the three methyl-groups of the amino acid.

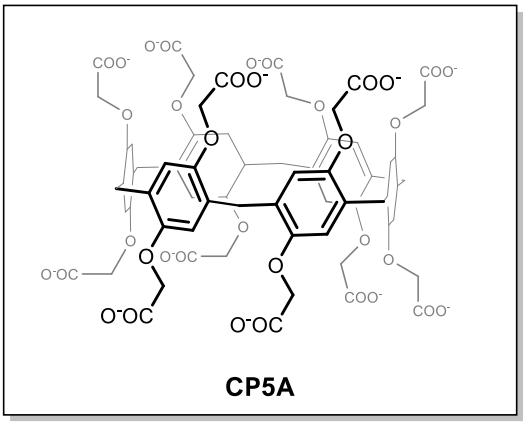

Figure 4. The electron-rich cavity of carboxylatopillar[5]arene (CP5A) has higher affinity towards lysine than trimethyl lysine.

Building upon prior research[17] of Isaacs' group, in 2022 Isaac's and Hof's groups[18] showed an interesting study on the binding properties of sulfonated pillar[5]arene and pillar[6]arene towards a series of methylated amino acids by isothermal titration calorimetry (Figure 5). They demonstrated that sulfopillar[6]arene prefers binding quaternary over primary diammonium ions thanks to an higher hydrophobic effect and cation-π interaction.

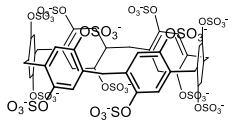

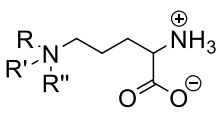

H-K-OH R=R′=R′′=H
H-K(Me)-OH R=Me, R′=R′′=H
H-K(Me_2)-OH R=R′=Me, R′′=H
H-K(Me_3)-OH R=R′=R′′=Me

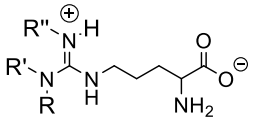

H-R-OH R=R′=R′′=H
H-R(Me)-OH R=Me, R′=R′′=H
Sym-H-R(Me_2)-OH R=R′′=Me, R′=H
Asym-H-R(Me_2)-OH R=R′= Me R′′=H

Figure 5. Chemical structure of sulfopillar[6]arene (left) and of lysine derivatives and arginine derivatives studied[17].

By comparing the association constants towards lysine salts and arginine salts, they enucleated the following major factors affecting complexation: I) ion-ion interactions; II) degree of methylation. The data demonstrate that favourable electrostatic cation-anion interaction is the critical driving force for complexation, whereas unfavourable electrostatic anion-anion interactions ($COO^{-}\cdots{}^{-}O_3OS$) impose a large free energy penalty on binding stability. Secondly, the study highlights a dramatic increase in binding affinity for the sulphated pillar[6]-and pillar[5]arene hosts as the degree of methylation increases: for example the association constant of sulphated pillar[6]arene for monomethylated lysine is $(9.19\pm0.18)\times10^{3}$ M^{-1}, for di-methylated lysine is $(2.52\pm0.05)\times10^{5}$ and for try-methylated lysine is to $(2.89\pm0.13)\times10^{6}$ M^{-1} (Table 1). This increased affinity is attributed to the fact that the more hydrophobic the guests' ammonium group is, this significantly enhances the hydrophobic effect and the cation- π interaction of the binding.

This enhancement allows the complex to adopt a more favourable geometry (Figure 6) which in turn reduces the energetic penalty from the unfavourable anion-anion electrostatic interaction ($COO^{-}\cdots{}^{-}O_3OS$) upon binding.

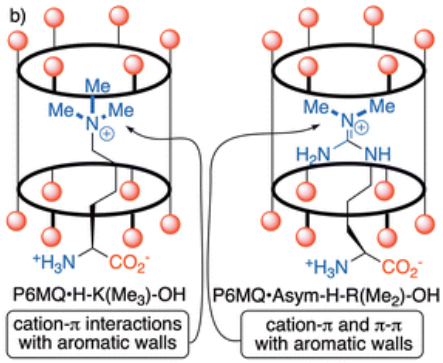

Figure 6. Illustration of the proposed geometries of the P6MQ·H–K(Me_3)–OH and P6MQ·Asym-H–R(Me_2)–OH complexes.

This effect is higher in sulfopillar[6]arenes: for example sulfopillar[5]arene binds tri-methylisine with an association constant of $(1.76\pm0.07)\times10^{4}$ M^{-1}, while

the association constant of sulfopillar[6]arene for the same guest is two orders of magnitude higher (Table 1). The two macrocycles differ for mainly in cavity size, charge density arrangement, and consequently in binding strength and selectivity. According to Isaacs[17], the six-unit macrocycle adopts an "alternating lean" conformation that packs the twelve sulfate groups around a triangular antiprism, giving a very high charge density at the cavity mouth (~12 SO_3^- within a small volume). In contrast, sulfopillar[5]arene has a smaller, more rigid cavity; its sulphate groups are spaced farther apart, resulting in lower electrostatic attraction and weaker overall binding. The reduced cavity size also limits the range of compatible guest dimensions, so sulfopillar[5]arene binds narrower guests inside the cavity and forces wider guests to interact only at the portals, yielding lower affinity and a broader, less discriminating binding pattern.

	P5MQ		***P6MQ***	
Guest	K_a [M^{-1}]	ΔH [Kcal mol^{-1}]	K_a [M^{-1}]	ΔH [Kcal mol^{-1}]
H-K-OH	$(9.26\pm2.67)\times10^{2}$	−1.70±0.38	$(1.74\pm0.09)\times10^{3}$	−4.84±0.14
H-K(Me)-OH	$(1.24\pm0.23)\times10^{3}$	−4.79±0.61	$(9.19\pm0.18)\times10^{3}$	−5.13±0.03
H-K(Me_2)-OH	$(6.13\pm0.18)\times10^{3}$	−7.31±0.20	$(2.52\pm0.05)\times10^{5}$	−8.10±0.04
H-K(Me_3)-OH	$(1.76\pm0.07)\times10^{4}$	−10.8±0.30	$(2.89\pm0.13)\times10^{6}$	−6.44±0.02
H-R-OH	$(3.77\pm0.24)\times10^{3}$	−6.57±0.18	$(5.85\pm0.13)\times10^{3}$	−6.65±0.06
H–R(Me)–OH	$(5.87\pm0.17)\times10^{3}$	−5.50±0.19	$(1.15\pm0.04)\times10^{4}$	−5.42±0.05
Sym-H–R(Me_2)–OH	$(5.35\pm0.16)\times10^{3}$	−4.84±0.05	$(6.45\pm0.36)\times10^{4}$	−4.78±0.10
Asym-H–R(Me_2)–OH	$(3.25\pm0.34)\times10^{3}$	−3.36±0.16	$(1.71\pm0.06)\times10^{5}$	−6.64±0.12

Table 1. Thermodynamic parameters (K_a [M^{-1}] and ΔH [Kcal mol^{-1}] determined by ITC for the complexes of sulfopillar[5] and sulfopillar[6]arene with diffent methylated state of arginine and lysine and their protic salts. Conditions: 25°C, PBS buffered H_2O, pH 7.4.

However, these studies were conducted in solution. Our goal is to assess the affinity of sulfopillar[6]arene toward proteins bearing trimethyl-lysine and arginine residues at the solid-liquid interphase.

1.3 Multivalency and grafting on silica nanoparticles (SiNPs)

Multivalency refers to the simultaneous weak and reversible interactions between multiple binding sites on one entity and complementary functionalities on another, referred as host and guest[19].

The requirement for a multivalent scaffold (i.e., multiple host macrocycles immobilized on a surface) when targeting amino acid side chains on histone proteins is driven by the need to overcome the inherent limitations of monovalent recognition in an aqueous biological environment. Individual non-covalent interactions between a single macrocycle and a single amino acid are typically characterized by low affinity (the dissociation constant is in the mM range) and rapid dissociation (k_{off}). Instead, when a multivalent receptor binds a multivalent ligand a strong increase in effective molarity (EM) is observed. This large increase in EM leads to an exponential enhancement of the apparent affinity (K_{app}) and a substantial decrease in the dissociation rate (the new complex's stability is not determined by the break of a single interaction, but by the simultaneous breaking of all interactions formed).

In a previous work conducted in our research group by Orlandini and al.[20] ferromagnetic nanoparticles decorated with tetraphosphonate cavitands showed selective enrichment of mono-methylated lysins present on histone tails with performances comparable with the commonly used antibodies (Figure 7). The magnetic nanoparticles were synthetized through co-precipitation method and were coated through non-covalent interaction with the carboxylate units present at the lower rim of the tetraphosphonate cavitand.

However, the degree of functionalisation of the nanoparticles is low due to the non-covalent nature of the carboxylate interaction which is labile to protic

environment. For this reason, we decided to exploit covalent binding to functionalized silica nanoparticles.

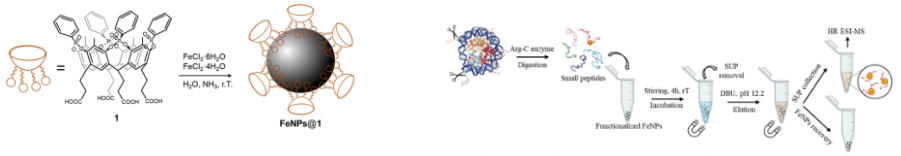

Figure 7. Ferromagnetic nanoparticles were anchored through non-covalent interaction via carboxylate anions. The cavitands separate the PTM-peptides target from the rest of the mixture, representing a promising alternative to commercial antibodies.

Empirical case studies on covalently functionalized silica nanoparticles with pillarenes are sparse. In 2015 Zhou et al.[12] introduced an innovative class of pillar[5]arene and pillar[6]arene-functionalized silica adsorbents that showed high affinity towards the herbicide paraquat using siloxane chemistry to ensure a stable covalent bond (Figure 8). The study showed that pillar[6]arene-modified material was more effective than the pillar[5]arene counterpart, reaching a saturation uptake of approximately 0.20 mmol paraquat per gram.

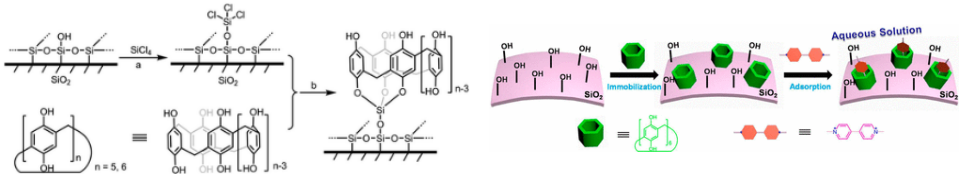

Figure 8. Schematic illustration of the immobilization of pillar[6]Arenes onto silica surfaces via prior surface activation with $SiCl_4$ and the adsorption of paraquat in an aqueous solution.

In 2024 Funda Ulusu and al.[21] synthetized silica gel nanoparticles functionalized with APTMS (3-aminopropyltrimethoxysilane) and

pillar[5]arene units (Si-APTMS-pillar[5]arene) with strong antimicrobial, antioxidant, and anticancer properties (Figure 9).

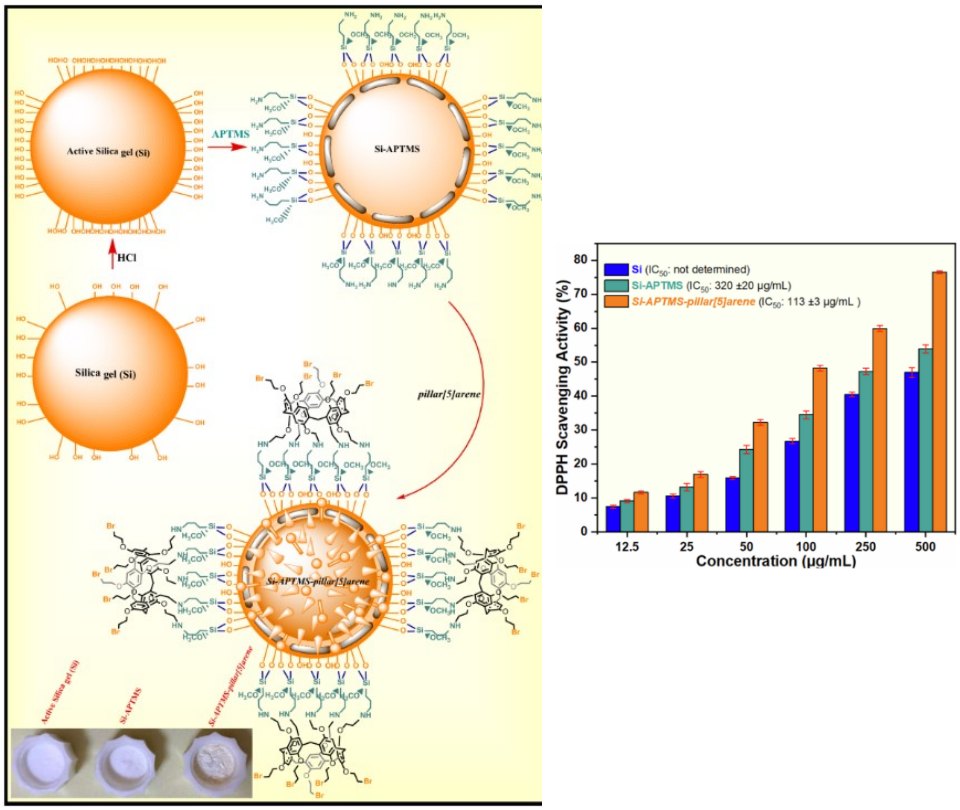

Figure 9. Schematic illustration of the synthesis of Si-APTMS-pillar[5]arene (left) and antioxidant activities of the activated silica gel (Si), Si APTMS, and Si-APTMS-pillar[5]arene materials (right). The data are means of triplicate (n = 3) ± standard error, $p < 0.05$.

Another method to functionalize silica gel nanoparticles is via Karstedt's catalyzed hydrosilylation between a terminal double bond and an excess of triethoxysilane as shown in a recent paper published by Dalcanale group[22] (Figure 10), where silica nanoparticles were decorated with a tetraquinoxaline

cavitand for detecting BTEX compounds (Benzene, Toluene, Ethylbenzene, and Xylene) in the air.

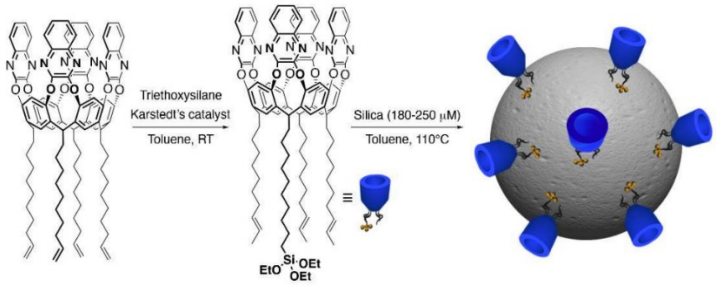

Figure 10. Schematic illustration of the covalent grafting of QxCav derivative on the silica surface.

In 2019 David Sánchez-García and al.[23] described a method for synthesizing isothiocyanate-functionalized Mesoporous Silica that served as drug delivery systems. The synthetic procedure involves simply exposing aminated nanoparticle to a "thiocarbonyl transfer reagent", (like 1,1-thiocarbonyldi-2(1H)-pyridone, as shown in Figure 11) which introduces the highly reactive isothiocyanate (NCS) moiety. The advantage of having such functionality is that the isothiocyanate group readily reacts with primary amines to form thioureas, is chemically stable and not prone to hydrolysis (unlike the highly reactive isocyanate group) and does not require toxic metal catalysts or complex activating agents.

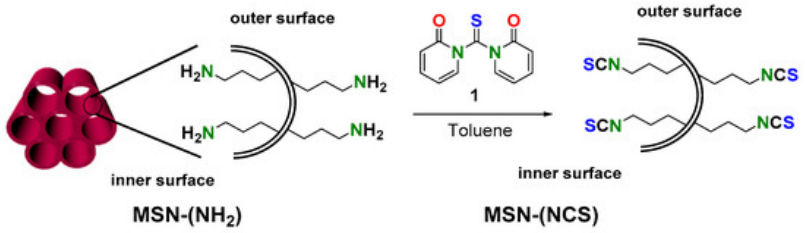

Figure 11. Preparation of decorated mesoporous silica nanoparticles (MSN)–(NCS).

2. Aim of the project

This chapter describes the synthesis of a monofunctionalized sulfo-pillar[6]arene whose specific linker enables the macrocycle to be covalently attached to silica nanoparticles using two alternative grafting strategies: I) hydrosilylation, leveraging the terminal double bond on the linker (Figure 12) II) thiourea bond formation, exploiting the terminal amino group of the macrocycle that will react with the isothiocyanate group on present on the silica's surface (Figure 13).

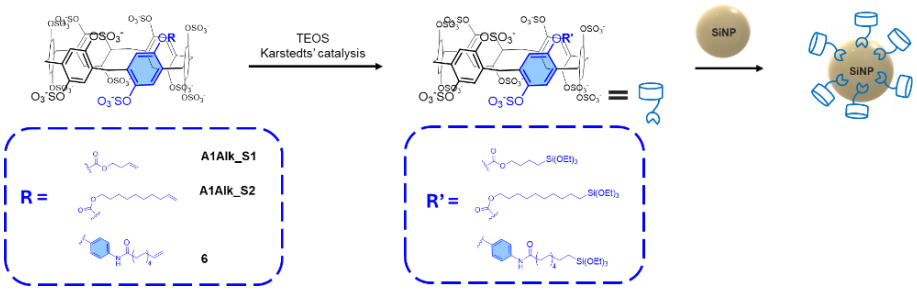

Figure 12. Illustration of the grafting method of the macrocycles A1Alk_S1, A1Alk_S2 and macrocycle 6 on silica nanoparticle trough functionalisation with TEOS and subsequent grafting on silica NP via hydrosililation with Karstedt's catalyst.

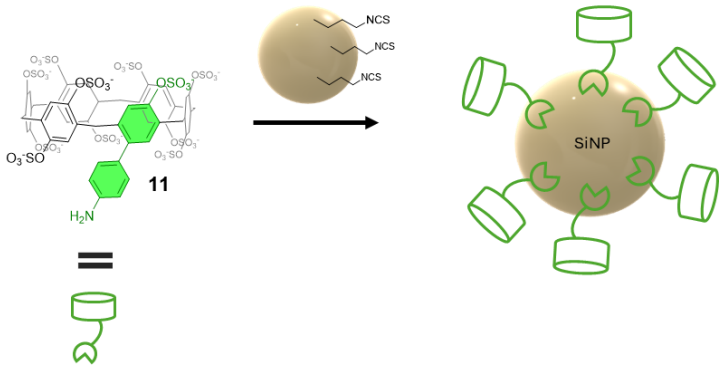

Figure 13. Schematic representation of the grafting strategy of the macrocycle 11 that present an aromatic amino group on the surface of a silica nanoparticle that present terminal thiourea groups.

3. Results and Discussion

The chosen approach to synthesize a monofunctionalized pillar[6]arene involves the selective deprotection of a single ethoxy group. The co-cyclization of different monomers is generally not the preferred method for obtaining mono-functionalized pillar[n]arenes due to the inherent formation of different compounds and the difficulties of the consequent purification[24]. Mono-functionalization is strategically important as it allows at the same time the macrocycle to be securely grafted onto the nanoparticle surface, while retaining sufficient mobility—a factor crucial for ensuring high binding efficiency toward its target.

In this chapter all the synthetic procedures start from the from the mono-deprotected ethoxypillar[6]arene **A1Dep** (Figure 14) obtained by selective deprotection of one ethoxy group of **EtOP6** with boron tribromide. Boron tribromide (BBr_3) is the preferred reagent for the cleavage of aromatic methoxy and ethoxy ethers due to its ability to perform the reaction under mild conditions and simple purification.

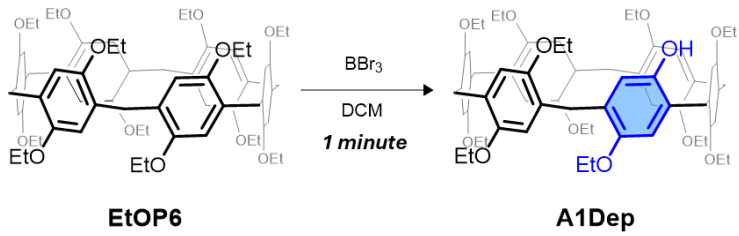

Figure 14. Reaction scheme to obtain mono-deprotected pillar[6]arene A1Dep.

The reaction of mono-deprotection of ethoxypillar[6]arene **EtOP6** is very quick: it is preferable to have low conversion but higher selectivity for the mono-deprotected product and recover the starting material. Since **EtOP6** is not soluble in acetone, it is easily recovered from the crude with a simple trituration. The mono-deprotected is purified via column chromatography as a white solid with a yield of 15%.

3.1 First synthetic route

In the first synthetic route, the mono-deprotected pillar[6]arene **A1Dep** was alkylated with two different bromo acetyl bromide derivatives **3a** and **3b** to obtain the neutral target molecules **A1Alk_1** and **A1Alk_2**. The two synthesized macrocycles differ in spacer length; this choice was made to subsequently investigate whether the length of the alkyl spacer might influence the functionalization efficiency of the coated silica nanoparticles to target the selected PTMs. The two macrocycles are the precursors of the polar target molecules, **A1Alk_S1** and **A1Alk_S2** to be obtained via total de-ethoxylation with boron tribromide and sulfation with sulphur-pyridinium complex (Figure 15).

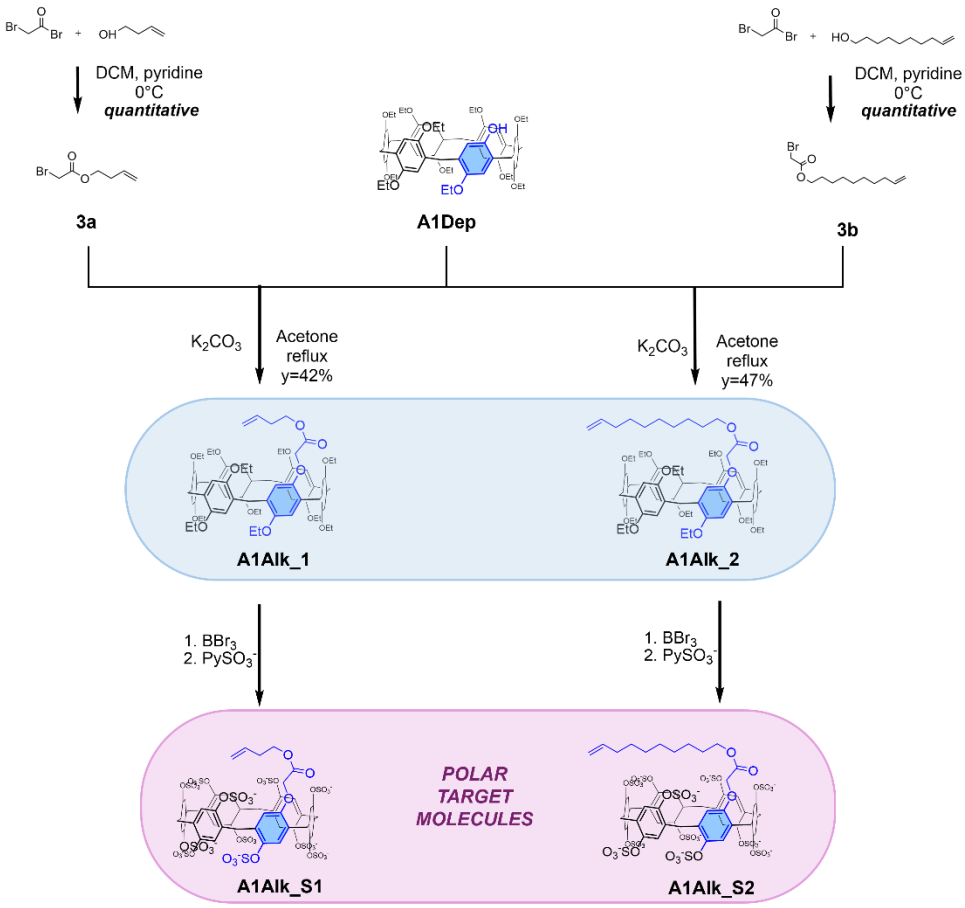

Figure 15. Synthetic strategy for A1Alk_1 and A1Alk_2 and A1Alk_S1 and A1Alk_S2.

The two alkylated pillar[6]arene **A1_Alk1** and **A1_Alk2** were successfully synthetized by reacting mono-deprotected pillar[6]arene **A1Dep** in an SN_2-type reaction with the bromo acetate derivative **3a** and **3b.** The two intermediates **A1_Alk1** and **A1_Alk2** were isolated by column chromatography respectively with a yield of 42% and 47%. The precursors **3a** and **3b** were obtained by reacting bromo acetyl bromide with 3-buten-1-ol and 9-decen-1-ol respectively in dichloromethane with pyridine and used without further purification.

The success of the alkylation reaction is proven by ^{1}HNMR. The stacking NMR data for starting material and the final product **A1_Alk1** in Figure 16 shows the appearance of characteristic vinyl signals **D** and **E** . Moreover, the success of the alkylation is evidenced by the shift in the signal patterns around 4 and 1.2 ppm: specifically, the alkylation of the phenolic oxygen restored the symmetry of the system due to the chemical shift similarity between the new substituent and the ethoxy ethyl moieties.

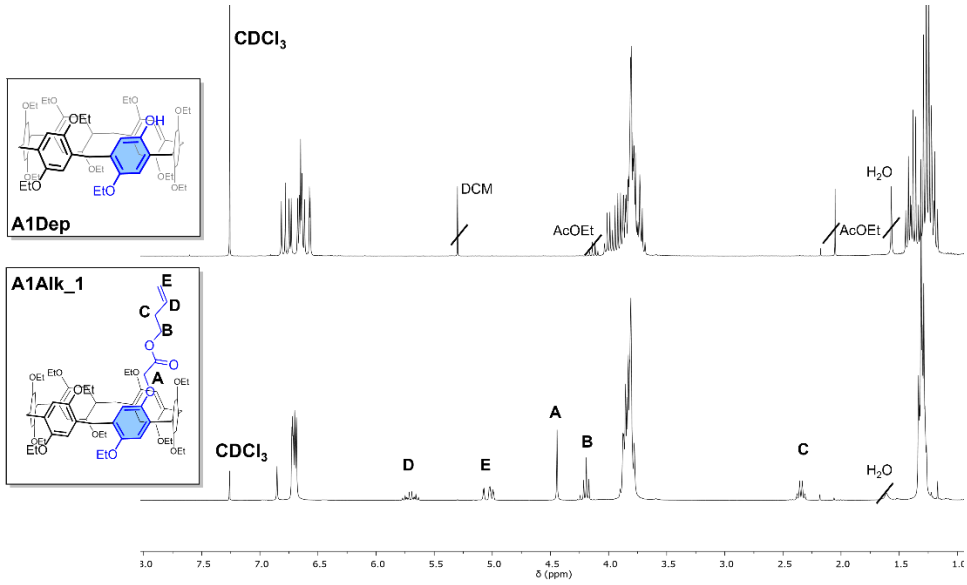

Figure 16. Stacking of the ^{1}HNMR ($CDCl_3$, 300MHz, 25°C) of the A1Dep and the product of alkylation A1Alk_1.

The same pattern is present also in the ^{1}HNMR spectra of **A1_Alk2** that features a longer linker chain (Figure 17).

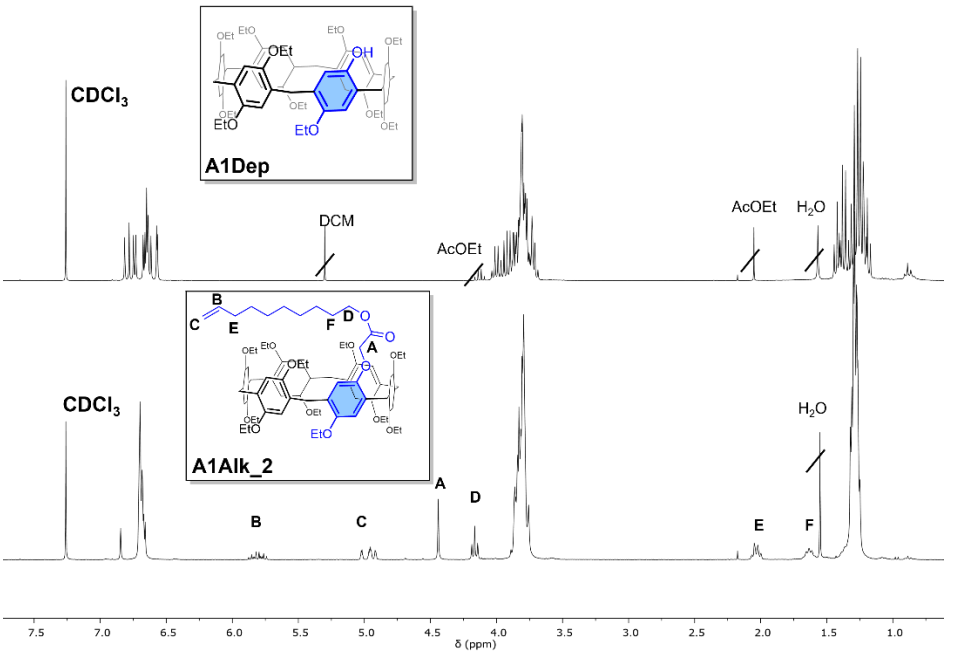

Figure 17. Stacking of the ^{1}HNMR ($CDCl_3$, 300MHz, 25°C) of the A1Dep and the product of alkylation A1Alk_2.

Two different attempts were made to deprotect the residual 11 ethoxy groups of the pillar[6]arene. In the first trial, following the procedure of Hof's group present in literature[27], the per-hydroxylated pillar[6]arene is obtained[28]. In the second attempt, the reaction time was shortened to 40 minutes but there was no control of the selectivity on the alkylation and only partial dealkylation was obtained. The linker group was labile to the boron tribromide deprotection and it is cleaved by the reactant.

3.2 Second synthetic route

In view of the negative results of the above synthetic procedure, a new synthetic approach is pursued: the ester bond was replaced by a more robust amide moiety, which is known to be stable under boron tribromide promoted deprotection.

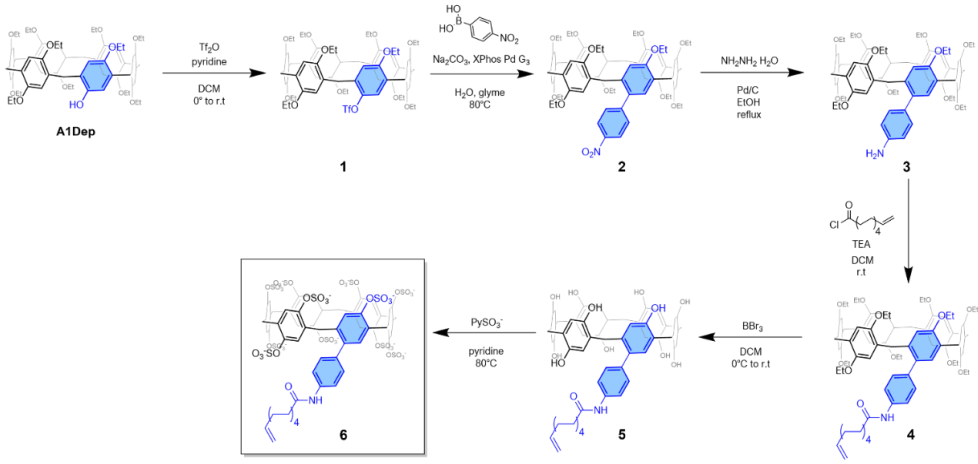

Figure 18. Synthetic strategy to obtain sulfonated pillar[6]arene 6.

Instead of introducing the linker group through alkylation, in the second synthetic procedure a Suzuki coupling is used to introduce a nitro-aromatic group following the procedure of Hof's group[27]. The mono-functionalized **A1Dep** is triflated with triflic anhydride to get the intermediate **1** in a 91% of yield. Then **1** is reacted with an aromatic 4-nitrophenyl boronic acid to get intermediate **2** with a yield of 82%. The product was fully characterized by NMR (Figure 19), and by ESI-MS.

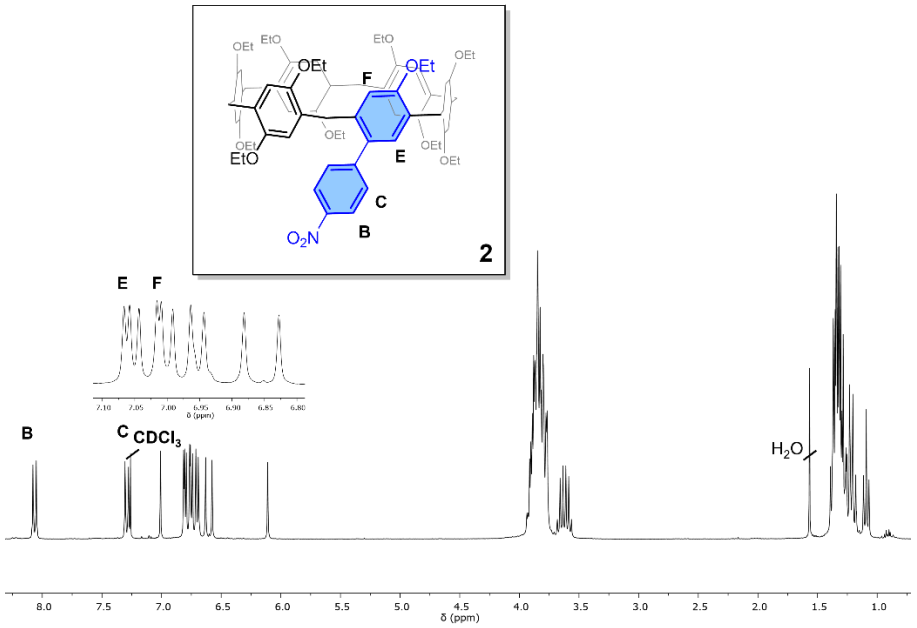

Figure 19. ^{1}HNMR ($CDCl_3$, 300MHz, 25°C) of the intermediate **2**. The protons **B** and **C** correspond to the signals of the aromatic ring carrying the nitro group.

This nitro group was then reduced to amine with hydrazine forming the intermediate **3** in 94% of yield. The linker was then connected through formation of an amide bond[29] forming the compound **4** in a 72% yield. In the subsequent reaction of de-ethoxylation with BBr_3 de-ethoxylation is accompanied by the disappearance of the double bond, while the amide bond isn't affected by boron tribromide. This can be seen in the proton NMR where the multiplets at 5.74 ppm and 4.89 ppm corresponding to the protons **B** and **C** of the terminal double bond are absents (Figure 20). The amide NH labelled as X' is still present.

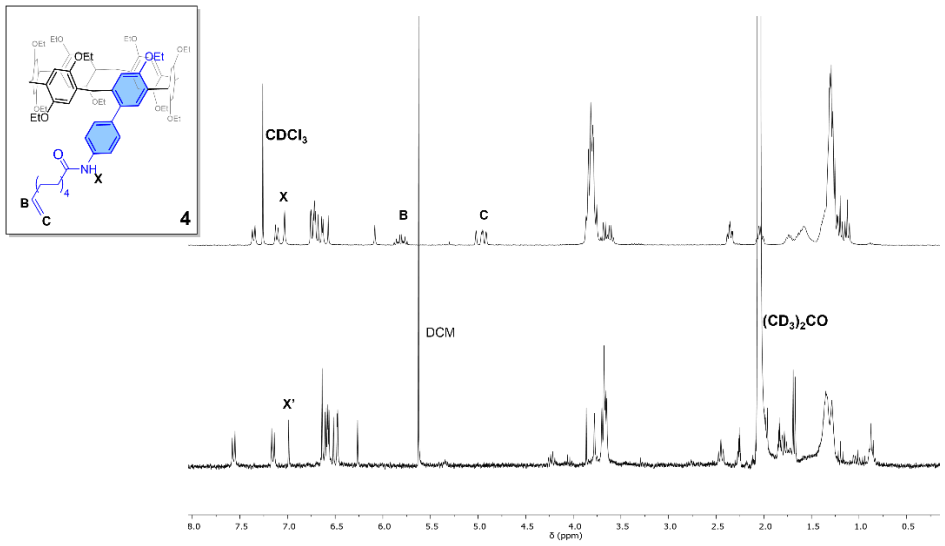

Figure 20. Stacking of ^{1}HNMR ($CDCl_3$, 300MHz, 25°C) of the intermediate 4 and ^{1}HNMR (acetone-d_6, 300MHz, 25°C) of the product of the de-ethoxylation reaction.

The disappearance of the vinylic protons **B** and **C** is attributed to the bromination of the terminal double bond by BBr_3. Considering this outcome, the synthetic design of the macrocycle was immediately revised. The anchoring group is then incorporated directly with the Suzuki coupling and the deprotection step is moved at the beginning of the synthesis.

3.3 Third synthetic route

After facing these challenges with the deprotection reaction, the synthesis of the target molecule was approached with a new strategy, as showed in the (Figure 21).

The target molecule is a totally sulfonated pillar[6]arene with an aromatic amino group that will be grafted covalently through thiourea bond formation on silica nanoparticles decorated with terminal isothiurea group (see Figure 13).

In this synthetic strategy the intermediate **2**, obtained by Suzuki coupling in the previous synthetic strategy, is deprotected with BBr_3 and then sulfonated to get the intermediate **10**. At this level, the nitro group is reduced to amine to be grafted on silica nanoparticles forming a thiourea bond. Currently this synthesis is under study in our research lab.

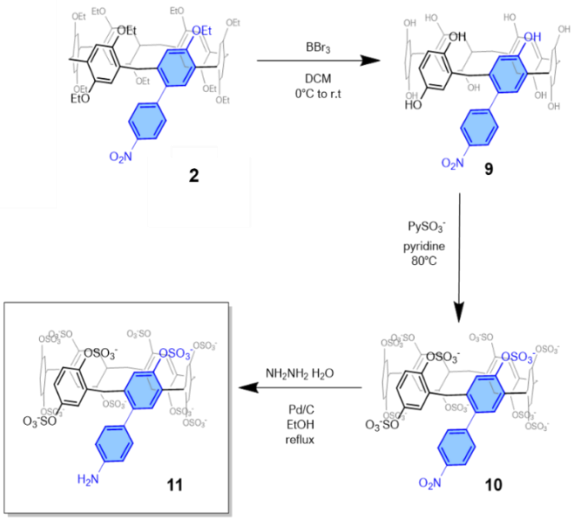

Figure 21. Third synthetic route to achieve the target molecule 11.

4. Conclusions

This chapter focused on establishing a viable synthetic route for mono-functionalized sulfopillar[6]arenes suitable for subsequent covalent functionalization on silica nanoparticles. The goal of this approach is to exploit the multivalency effect for enhanced affinity and specificity toward two epigenetic targets: methylated lysine and arginine residues in histones.

Three distinct synthetic pathways were systematically investigated to achieve the required mono-functionalization.

The first synthetic route yielded two monofunctionalized pillar[6]arene **A1Alk_1** and **A1Alk_2** where a linker of variable chain length is connected to the macrocycle with an ester bond. However, the synthesis revealed a significant chemical incompatibility: the ester bond was cleaved under the boron tribromide mediated deprotection conditions. To address this challenge, the second synthetic route was developed, replacing the ester moiety with a more robust amide bond. While the amide bond successfully survived to the boron tribromide deprotection, the terminal vinyl functionality necessary for subsequent surface grafting was found to react under these conditions, preventing the isolation of the desired functionalized product,

These issues required a strategic alternative in choosing the anchoring group to bypass the inherent incompatibility of the alkene moiety. This methodology involves the reaction between an amine-functionalized and an isothiocyanate-functionalized silica nanoparticles, providing a robust coupling method that is orthogonal to the final deprotection steps.

5. Experimental Part

5.1 Materials and methods

All substances were purchased from certified commercial sources and used as received, without further purification. The solvents designated as anhydrous are treated according to procedures well-established in the literature.

NMR spectra, including ^{1}H, COSY, ^{13}C, DEPT135, and HSQC, were recorded on a Bruker AVANCE 300 MHz spectrometer using $CDCl_3$ or acetone-d_6 as solvents.

All chemical shifts (δ) are referred in parts per million (ppm) and referenced either to the residual proton resonances from incomplete deuteration of the NMR solvents or to the solvent's ^{13}C resonance. The abbreviations: s, d, dd, t

and m refer to the spectrum signals: singlet, doublet, doublet of doublets, triplet and multiplet, respectively. The letter "b" that eventually precedes the abbreviations means broad.

Electrospray ionization mass spectrometry (ESI-MS) analyses were performed using either an Infusion Waters Acquity Ultra Performance LC HO6UPS-823M instrument equipped with an electrospray ionization (ESI) source operating in positive mode or an Agilent 1260 Infinity II system with an ESI source also configured in positive mode.

Synthesis of A1Dep: This method was adapted from literature[27]. An oven-dry flask is charged with EtOP6 (2.75 g, 1 eq., 2.57 mmol) and purged and backfilled with argon 3 times. Anhydrous DCM (300 mL) was added with a syringe. BBr_3 (0.537 mL, 5.6 mmol, 2.20 eq) was added via syringe using a disposable long needle all at once. The reaction was stirred for 1 minute then was quenched by adding H_2O. The organic layer was washed with H_2O (x2), the combined aqueous layer was washed with DCM (x1). The combined organic layer was dried over $MgSO_4$ and concentrated to dryness on a rotary evaporator. Unreacted EtOP6 (792 mg) was recovered by washing the crude solid with acetone and vacuum filtering. The filtrate was crude product and the remaining solid was EtOP6. The filtrate was then concentrated to dryness on a rotary evaporator and purified via flash column chromatography (eluent Hex:AcOEt from 100% of Hexane to 8:2). The product is obtained as a white solid with a yield of 15%. The ^{1}HNMR is in accordance with the literature[27].

Synthesis of 3a: An oven dry round flask is charged with 3-buten-1-ol (208 µL, 2.42 mmol,1.05 eq) and pyridine (599 µL, 7.44 mmol, 3.23 eq) diluted in 5 mL of dry dichloromethane. The solution is cooled at 0°C when bromoacethyl bromide (300 µL, 3.45 mmol) is added via syringe over 5 minutes. The reaction is stirred for 15 minutes, then is diluted with Et_2O (30 mL) and and allowed to warm at room temperature. The organic phase is washed with HCl 1M and

saturated $NaHCO_3$. Then it is dried with Na_2SO_4 and concentrated in vacuo to give the crude bromo acetate **3a** as a clear yellow oil (400mg). The product is used immediately without further purification.

Synthesis of 3b: An oven dry round flask is charged with 9-decen-1-ol (647 µL, 3.63 mmol,1.05 eq) and pyridine (599 µL, 7.44 mmol, 3.23 eq) diluted in 5 mL of dry dichloromethane. The solution is cooled at 0°C when bromoacethyl bromide (300 µL, 3.45 mmol) is added via syringe over 5 minutes. The reaction is stirred for 15 minutes, then is diluted with Et_2O (30 mL) and and allowed to warm at room temperature. The organic phase is washed with HCl 1M and saturated $NaHCO_3$. Then it is dried with Na_2SO_4 and concentrated in vacuo to give the crude bromo acetate **3b** as a clear yellow oil (900mg). The product is used immediately without further purification.

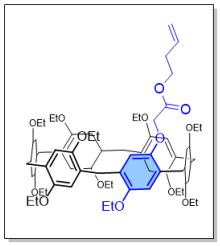

Synthesis of A1Alk_1: In an oven-dry flask A1Dep (150 mg, 142 µmol, 1 eq) is suspended in 1mL of dry acetone with potassium carbonate (39 mg, 283 µmol, 2 eq). Then, but-3-en-1-yl 2-bromoacetate **3a** (41 mg, 212 µmol, 1.5 eq) and KI (2.35 mg, 0.1 eq) are added, and the mixture is refluxed for 24 h. After checking the disappearance of the reagent with TLC, the organic phase is washed with a solution of HCl 1M and extracted with ethyl acetate. The product purified via flash column chromatography (petroleum ether: AcOEt 95:5 to 8:2) to obtain **A1Alk_1** as a white solid (70 mg, 42% yield).

^{1}H NMR (300 MHz, $CDCl_3$, 25°C) δ 6.85 (s, 1H, Ar-*H**), 6.76 – 6.61 (m, 12H, Ar-*H*), 5.78 – 5.61 (m, 1H, H_D), 5.12 – 4.92 (m, 2H, H_E), 4.44 (s, 2H, H_A), 4.19 (t, *J* = 6.8 Hz, 2H, HB), 3.93 – 3.72 (m, 34H, CH_2CH_3), 2.35 (q, *J* = 7.5Hz, 2H, H_c), 1.39-1.21 (m, CH_2CH_3 ,36H).

ESI-MS: theoretical $[C_{70}H_{106}O_{14}+Na]^+$: 1194.76 m/z; Found ESI-MS (MeOH): 1194.00 m/z

^{13}C NMR (300 MHz, $CDCl_3$, 25°C) δ 133.52, 117.48 (terminal C of the insaturation), 116.86 – 113.75 (phenyl groups of pillar[6]arene), 66.60 (C in alfa of the carbonyl group), 63.92 (C in alfa of the esther group), 32.95 (C in alfa of the insaturation), 32.65 – 30.58 (CH_2CH_3), 15.19 (CH_3).

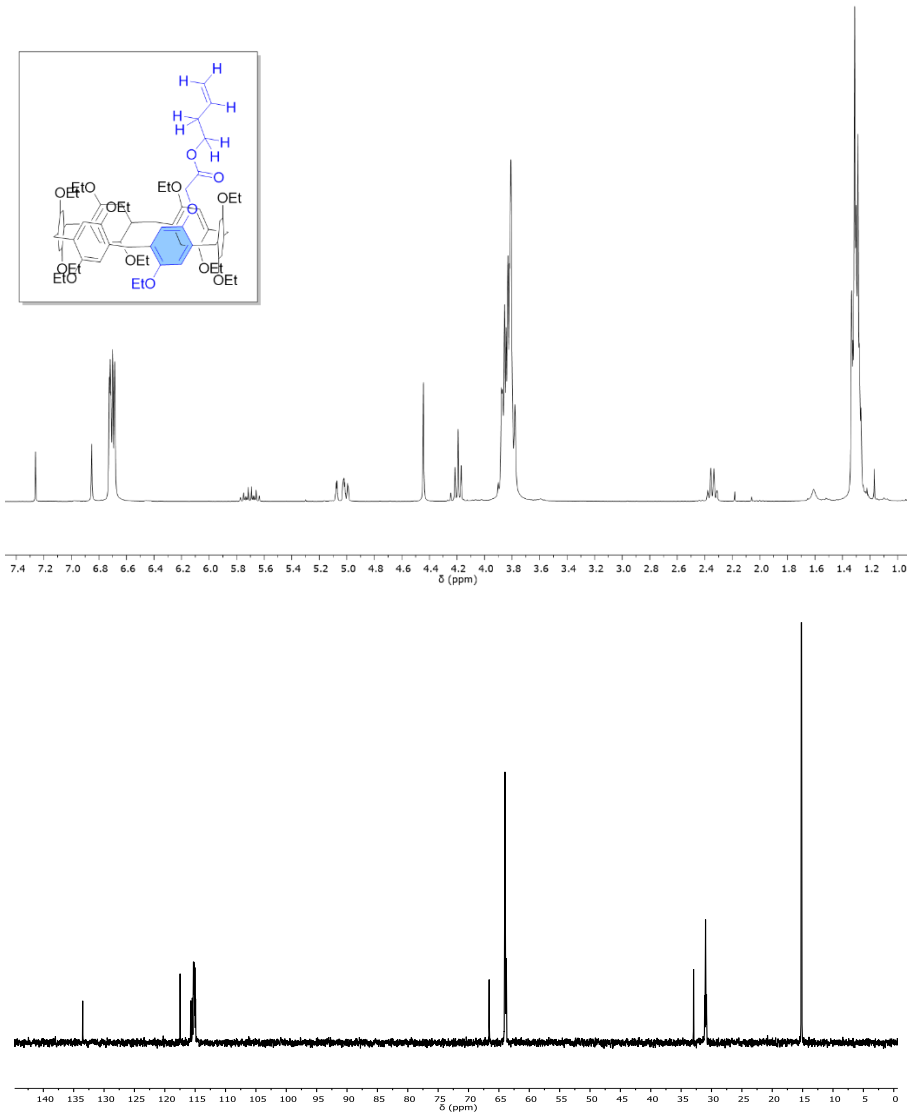

Figure 22. ^{1}H-NMR characterization of A1Alk_1 (300 MHz, $CDCl_3$, 25°C).

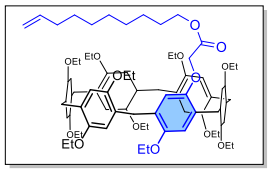

Synthesis of A1Alk_2: In an oven-dry flask **A1Dep** (265 mg, 250.1 µmol, 1 eq) is suspended in 1mL of dry acetone with potassium carbonate (69 mg, 500.2 µmol, 2 eq).Then, dec-9-en-1-yl 2-bromoacetate **3b** (104 mg, 375.2 µmol, 1.5 eq.) and KI (2 mg, 0.1 eq) are added and the mixture is refluxed for 24 h. After checking the disappearance of the reagent with TLC, the organic phase is washed with a solution of HCl 1M and extracted with ethyl acetate. The product purified via flash column chromatography (petroleum ether: AcOEt 95:5 to 8:2) to obtain **A1Alk_2** as a white solid (149 mg, 47% yield).

^{1}H NMR (300 MHz, $CDCl_3$, 25°C) δ 6.85 (s, 1H), 6.74 – 6.60 (m, 15H), 5.81 (ddt, *J* = 16.9, 10.2, 6.7 Hz, 1H), 5.04 – 4.88 (m, 2H), 4.44 (s, 2H), 4.16 (t, *J* = 6.8 Hz, 2H), 3.90 – 3.73 (m, 46H), 2.08 – 1.97 (m, 2H), 1.62 (q, *J* = 6.7 Hz, 2H), 1.28 (qd, *J* = 6.9, 3.9 Hz, 55H).

ESI-MS positive ions: theoretical $[C_{70}H_{106}O_{14}+H]^+$: 1256.77 m/z; Found ESI-MS (MeOH): 1256.0 m/z

^{13}C NMR (300 MHz, $CDCl_3$, 25°C) δ 115.21, 114.90, 114.17, 66.71, 65.11, 63.99, 63.88, 63.68, 33.77, 31.25, 30.94, 29.18, 29.03, 28.88, 28.58, 25.80, 15.18.

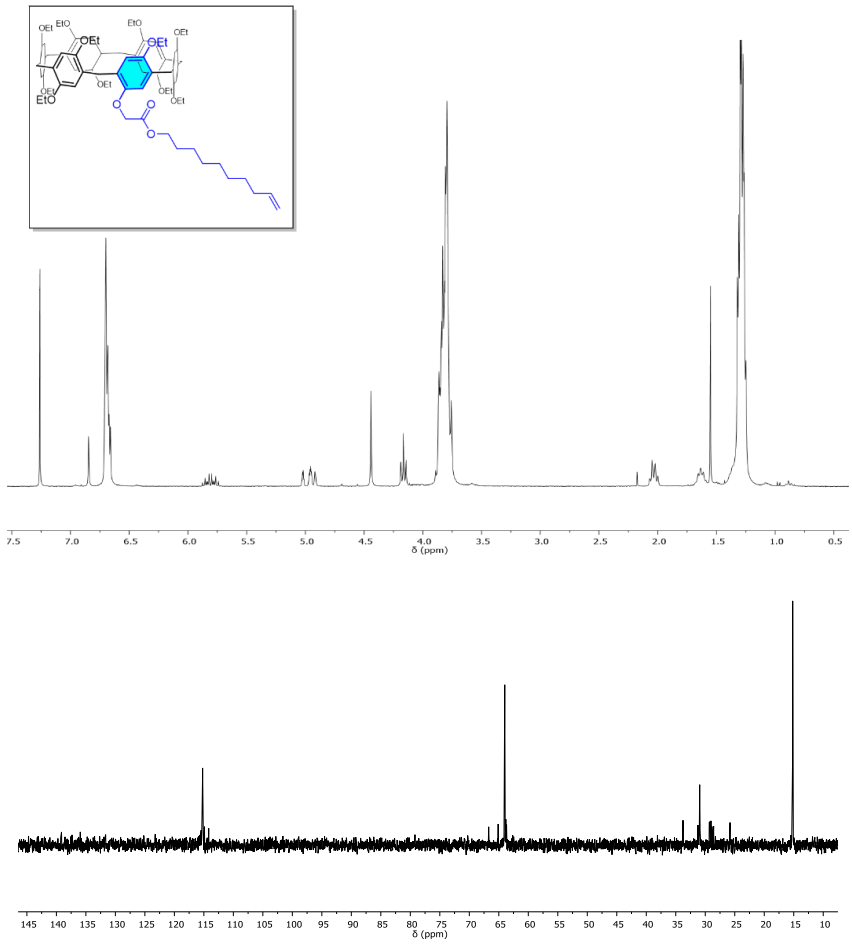

Figure 23. ^{1}H-NMR characterization of A1Alk_2(300 MHz, $CDCl_3$, 25°C).

Synthesis of A1_AlkS1. Under argon conditions, **A1_Alk1** (30.0 mg, 25.61 µmol, 1 eq) is dissolved in 1mL of dry DCM. Then, using an ice bath, BBr_3 (0.05 mL, 564 µmol, 22 eq.) is added dropwise (waiting until the green color disappears before adding more) using a liquid nitrogen bath. The mixture is left stirring at room temperature either for 24 hrs or for 40 min. Then, the reaction is quenched by adding water. The precipitate is washed with a solution of HCl 1M. The procedure didn't lead to the formation of the desired product.

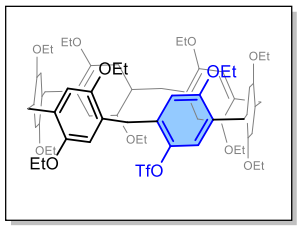

Synthesis of 1: In a dry flask **1** (440 mg, 0.42 mmol, 1 eq.) and pyridine (170 µL, 2.11 mmol, 5 eq.) were dissolved in 75 mL of DCM dry. Trifluoromethanesulfonic anhydride solution (1 M in methylene chloride) (1.3 mL, 1.3 mmol, 3.1 eq.) was slowly added dropwise using an ice bath. The reaction was left to stir 5hrs from 0°C to room temperature until the disappearance of the reagent checked with TLC (Hex:AcOEt 9:1). The reaction was quenched with H_2O and the organic layer was washed with H_2O (x3) and brine (x3). The organic layer was dried over MgSO4 and vacuum filtered. The filtrate was concentrated to dryness on a rotary evaporator and purified via flash column chromatography (eluent Hex:AcOEt 9:1). **1** was obtained (450 mg, 91% yield) as a white solid. HR-ESI-MS: m/z $[M+Na]^+$ theoretical 1195.50404; found: 1195.50359.

^{1}H NMR (300 MHz, $CDCl_3$, 25°C) δ 7.11 (s, 1H), 6.77 (s, 1H), 6.75 (s, 1H), 6.71 – 6.69 (m, 7H), 6.64 (s, 1H), 6.60 (s, 1H), 3.94 – 3.75 (m, 32H), 3.72 (q, J = 7.0 Hz, 2H), 1.39 – 1.22 (m, 30H), 1.18 (t, J = 7.0 Hz, 3H).

^{13}C NMR (300 MHz, $CDCl_3$, 25°C) δ 155.9, 150.7, 150.7, 150.6, 150.6, 150.6, 150.5, 150.5, 150.5, 150.4, 141.1, 132.3, 129.2, 129.0, 128.5, 128.3, 128.1, 128.1, 127.9, 127.7, 127.6, 126.1, 125.2, 123.6, 115.6, 115.5, 115.5, 115.4, 115.3, 115.2, 115.2, 115.0, 114.8, 114.8, 113.8, 64.3, 64.2, 64.2, 64.1, 64.1, 64.1, 64.0, 63.8, 63.8, 63.6, 31.8, 31.3, 31.1, 31.1, 30.7, 15.4, 15.4, 15.3, 15.3, 15.3, 15.3, 15.0, 15.0.

^{19}F NMR (283 MHz, CDCl3) δ -73.9.

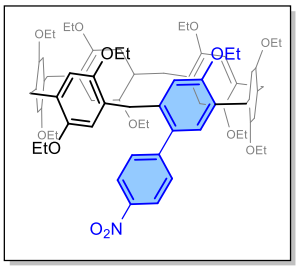

Synthesis of 2: Under a flow of argon an oven-dry microwave vial equipped with a stir bar was charged with **1** (263 mg, 0.22 mmol, 1 eq.), Na_2CO_3 (140 mg, 1.32 mmol, 6 eq.), (4-nitrophenyl)boronic acid (184 mg, 1.10 mmol, 5 eq.) and XPhos Pd G3

(56 mg, 0.06 mmol, 0.3 eq.). Glyme (degassed via sparging with argon for 1 hour, 8 mL) was added, the microwave vial was closed and placed in a pre-heated 84°C oil bath. An argon balloon was added. Water (degassed via sparging with argon for 1 hour, 2 mL) was added via syringe and the reaction was stirred under argon at 84°C for 18 hours. The vessel was removed from heat and let cool to room temperature. Water and DCM were added, and the organic layer was extracted and washed with water (x2). The organic layer was dried over Na_2SO_4 and vacuum filtered. The filtrate was concentrated to dryness on a rotary evaporator. Crude **2** was purified via flash column chromatography with DCM. **2** was obtained as a bright yellow solid (212 mg, 82% yield).

^{1}H NMR (300 MHz, $CDCl_3$, 25°C) δ 8.00 (d, *J* = 8.7 Hz, 2H), 7.22 (d, *J* = 8.6 Hz, 2H), 6.74 (d, *J* = 2.6 Hz, 2H), 6.72 (s, 1H), 6.69 (d, *J* = 2.1 Hz, 2H), 6.67 (s, 1H), 6.64 (s, 1H), 6.62 (s, 1H), 6.56 (s, 1H), 6.51 (s, 1H), 6.04 (s, 1H), 3.78 (m, 33H), 3.55 (q, *J* =6.9 Hz, 2H), 1.36 – 1.10 (m, 30H), 1.02 (t, *J* = 6.9 Hz, 3H).

ESI-MS positive ions $[C_{70}H_{101}NO_{13}+H]^+$ theoretical: 1165.57 m/z; found (MeOH) 1165.9 m/z.

^{13}C NMR (300 MHz, $CDCl_3$, 25°C) δ 132.23, 130.53, 122.82, 115.59, 115.39, 115.05, 114.99, 114.94, 114.88, 114.37, 113.20, 64.15, 64.06, 64.02, 63.94, 63.89, 63.82, 63.79, 63.27, 33.99, 31.19, 30.93, 30.75, 30.65, 30.56, 15.27, 15.23, 15.21, 15.13, 14.99, 14.95, 14.93.

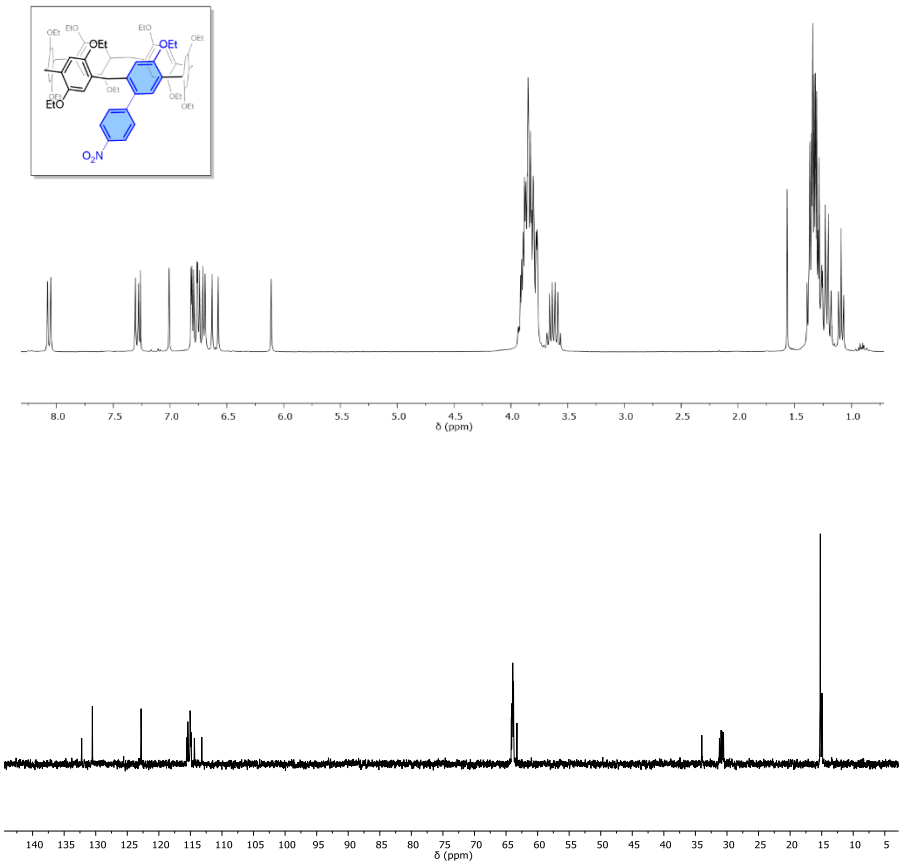

Figure 24: ^{1}H-NMR characterization of 2 (300 MHz, $CDCl_3$, 25°C).

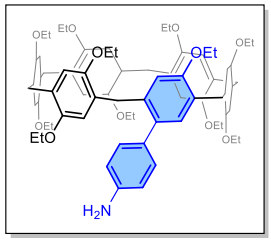

Synthesis of 3: In a round bottom flask 2 (212 mg, 0.18 mmol, 1 eq) is dissolved in 5 mL of EtOH together with hydrazine hydrate (0.170 mL, 30 eq) and Pd/C (1.86 mg, 0.1 eq). The mixture is left stirring at reflux temperature for 3 hours until the reagent disappears. Then the catalyst is filtered, and the organic phase is washed with water and dried with Na_2SO_4 and vacuum dried to obtain **3** as a white solid (194 mg, 94% yield).

^{1}H NMR (300 MHz, $CDCl_3$, 25°C) δ 7.09 (s, 1H), 7.02 (d, *J* = 8.3 Hz, 2H), 6.78 – 6.54 (m, 11H), 6.15 (s, 1H), 3.91 – 3.59 (m, 34H), 1.40 – 1.07 (m, 33H).

ESI-MS positive ions: $[C_{70}H_{103}NO_{11}+H]^+$ 1135.01 m/z; Found (MeOH) 1135.3 m/z.

^{13}C NMR (300 MHz, $CDCl_3$, 25°C) δ 133.15, 130.57, 115.51, 115.33, 115.06, 114.87, 114.56, 112.80, 64.18, 64.09, 64.01, 63.84, 63.01, 33.73, 31.17, 30.95, 15.22, 15.19, 15.16, 15.10, 15.05, 14.98.

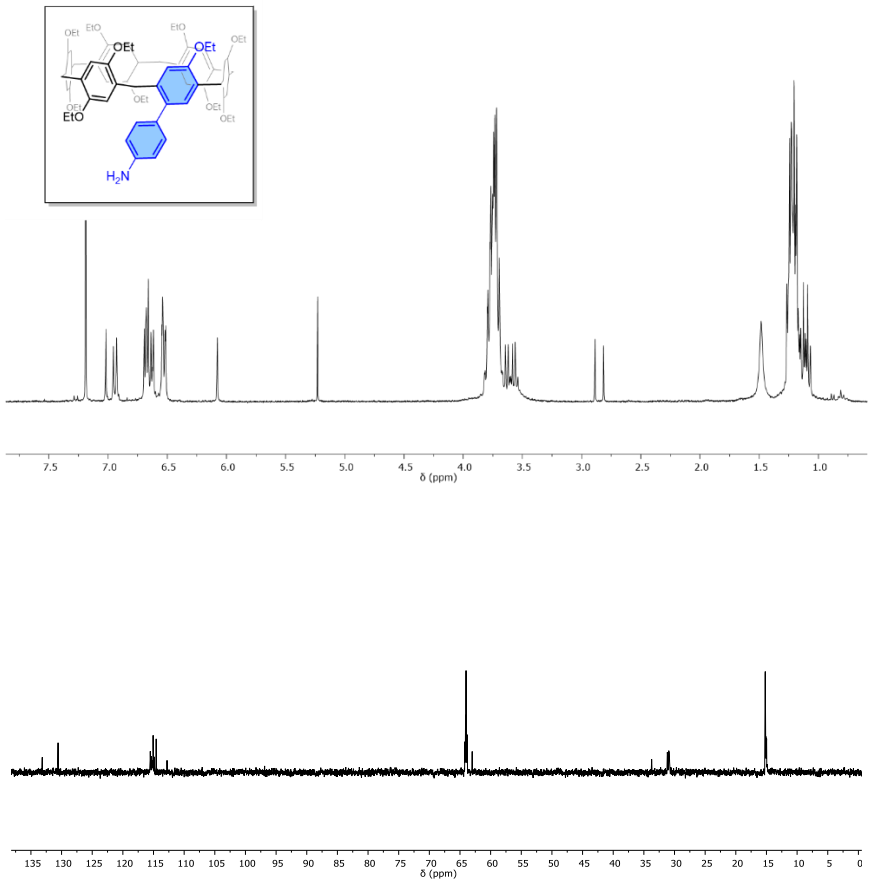

Figure 25. ^{1}H-NMR characterization of A1NH_2 (300 MHz, $CDCl_3$, 25°C).

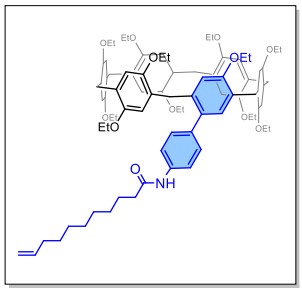

Synthesis of 4: Under argon conditions, **3** (110mg, 96.95 µmol, 1eq) and triethylamine (0.03 mL, 223 µmol, 2.30 eq) are dissolved in 1 mL of dry DCM. Then, undec-10-enoyl chloride (20.8 µL, 96.95 µmol, 1 eq) is added dropwise using an ice bath. The mixture is left reacting at room temperature until disappearance of the reagent on TLC. Then, the reaction is quenched with a saturated solution of $NaHCO_3$ and the organic fraction is extracted with ethyl acetate and dried over Na_2SO_4. The product **4** is purified via flash column chromatography (eluent Hex:AcOEt 8:2) and obtained as a white solid with a yield of 72%.

ESI-MS (MeOH). $[M+Na]^+$ Theoretical: 1322.99 m/z; Found: 1322.9 m/z.

^{1}H NMR (300 MHz, $CDCl_3$, 25°C) δ 7.35 (d, *J* = 8.2 Hz, 1H), 7.11 (d, *J* = 8.2 Hz, 1H), 7.03 (d, *J* = 2.4 Hz, 1H), 6.80 – 6.53 (m, 5H), 6.08 (s, 0H), 5.90 – 5.70 (m, 1H), 5.04 – 4.87 (m, 2H), 3.90 – 3.55 (m, 17H), 2.36 (td, *J* = 7.5, 2.8 Hz, 2H), 2.10 – 1.98 (m, 2H), 1.74 (t, *J* = 7.1 Hz, 1H), 1.61 (d, *J* = 17.6 Hz, 4H), 1.43 – 1.07 (m, 27H).

^{13}C NMR (300 MHz, $CDCl_3$, 25°C) δ 139.18, 138.64, 136.36, 132.85, 130.14, 118.90, 115.37, 114.16, 64.17, 63.98, 63.88, 63.04, 33.78, 31.04, 29.33, 29.03, 28.89, 15.19, 15.08, 15.01.

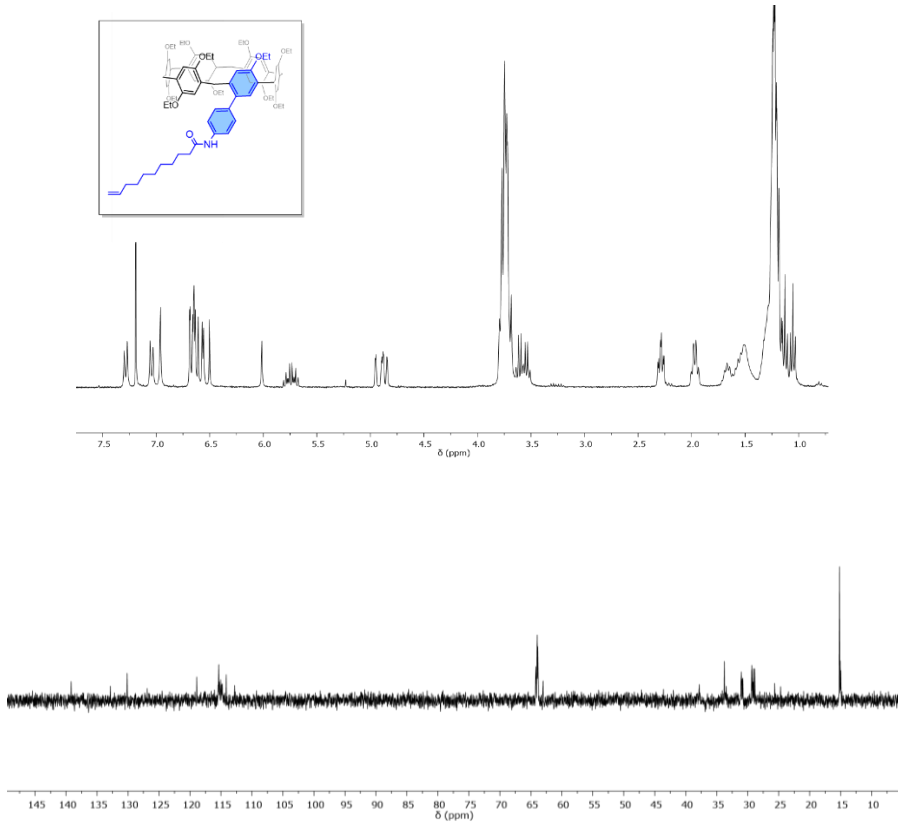

Figure 26. ^{1}H-NMR characterization of 4 (300 MHz, $CDCl_3$, 25°C).

Synthesis of 5. Under argon atmosphere, **4** (30.0 mg, 23.06 µmol, 1 eq) is dissolved in 1mL of dry DCM. Then, using an ice bath, BBr_3 (0.04 mL, 415 µmol, 18 eq.) is added dropwise (waiting until the green color disappears before adding more). The mixture is left stirring at room temperature for 24 hrs. Then, the reaction is quenched by adding water. The precipitate is washed with a solution of HCl 1M. This procedure didn't lead to the desired product.

6. References

[1] Ramazi, S.; Zahiri, J. Post-Translational Modifications in Proteins: Resources, Tools and Prediction Methods. Database **2021**, 2021, baab012. https://doi.org/10.1093/database/baab012.

[2] (Mann, M.; Jensen, O. N. Proteomic Analysis of Post-Translational Modifications. Nat. Biotechnol. **2003**, 21:255-61.

[3] Liu, J.; Wang, Q.; Kang, Y.; Xu, S.; Pang, D. Unconventional Protein Post-Translational Modifications: The Helmsmen in Breast Cancer. Cell Biosci. **2022**, 12, 22. https://doi.org/10.1186/s13578-022-00756-z.

[4] Scharf, A. N. D.; Imhof, A. Every Methyl Counts--Epigenetic Calculus. FEBS Lett. **2011**, 585, 2001–2007. https://doi.org/10.1016/j.febslet.2010.11.029.

[5] Berryhill, C. A.; Hanquier, J. N.; Doud, E. H.; Cordeiro-Spinetti, E.; Dickson, B. M.; Rothbart, S. B.; Mosley, A. L.; Cornett, E. M. Global Lysine Methylome Profiling Using Systematically Characterized Affinity Reagents. Sci. Rep. **2023**, 13, 377. https://doi.org/10.1038/s41598-022-27175-x.

[6] Pinalli, R.; Pedrini, A.; Dalcanale, E. Biochemical Sensing with Macrocyclic Receptors. Chem. Soc. Rev. **2018**, 47, 7006–7026. https://doi.org/10.1039/C8CS00271A.

[7] Gruber, T. Synthetic Receptors for the Recognition and Discrimination of Post-Translationally Methylated Lysines. ChemBioChem **2018**, 19, 2324–2340. https://doi.org/10.1002/cbic.201800398.

[8] Ogoshi, T.; Kanai, S.; Fujinami, S.; Yamagishi, T.; Nakamoto, Y. Para-Bridged Symmetrical Pillar[5]Arenes: Their Lewis Acid Catalyzed Synthesis and Host–Guest Property. J. Am. Chem. Soc. **2008**, 130, 5022–5023. https://doi.org/10.1021/ja711260m.

[9] Swirepik, O.; Smith, J. N.; White, N. G. Balancing on a Knife's Edge: Studies on the Synthesis of Pillar[6]Arene Derivatives. J. Org. Chem. **2023**, 88, 8310–8315. https://doi.org/10.1021/acs.joc.3c00305.

[10] Ogoshi, T.; Aoki, T.; Kitajima, K.; Fujinami, S.; Yamagishi, T.; Nakamoto, Y. Facile, Rapid, and High-Yield Synthesis of Pillar[5]Arene from Commercially Available Reagents and Its X-Ray Crystal Structure. J. Org. Chem. **2011**, 76, 328–331. https://doi.org/10.1021/jo1020823.

[11] Santra, S.; Kopchuk, D. S.; Kovalev, I. S.; Zyryanov, G. V.; Majee, A.; Charushin, V. N.; Chupakhin, O. N. Solvent-Free Synthesis of Pillar[6]Arenes. Green Chem. **2016**, 18, 423–426. https://doi.org/10.1039/C5GC01505G.

[12] Cao, J.; Shang, Y.; Qi, B.; Sun, X.; Zhang, L.; Liu, H.; Zhang, H.; Zhou, X. Synthesis of Pillar[n]Arenes (n = 5 and 6) with Deep Eutectic Solvent Choline Chloride $2FeCl_3$. RSC Adv. **2015**, 5, 9993–9996. https://doi.org/10.1039/C4RA15758C.

[13] Santra, S.; Kovalev, I. S.; Kopchuk, D. S.; Zyryanov, G. V.; Majee, A.; Charushin, V. N.; Chupakhin, O. N. Role of Polar Solvents for the Synthesis of Pillar[6]Arenes. RSC Adv. **2015**, 5, 104284–104288. https://doi.org/10.1039/C5RA19569A.

[14] Chelsea R. W. Evan F. W. C., Austia O. P., and Fraser H. Org. Synth. **2022**, 99, 125-138.

[15] Shixin F., Takahiro K., Tada-aki Y. and Tomoki O. CCS Chem. **2019**, 1, 50–63. https://doi.org/10.31635/ccschem.019.20180014

[16] Chunju L., Junwei M., Liu Z., Yanyan Z., Yihua Y. Xiaoyan S., Jian L. and Xueshun J. Chem. Commun., **2013**,49, 1924-1926.

[17] Xue, W.; Zavalij, P. Y.; Isaacs, L. Pillar[n]MaxQ: A New High Affinity Host Family for Sequestration in Water. Angew. Chem. Int. Ed. **2020**, 59 13313–13319. https://doi.org/10.1002/anie.202005902.

[18] King, D.; Wilson, C. R.; Herron, L.; Deng, C.-L.; Mehdi, S.; Tiwary, P.; Hof, F.; Isaacs, L. Molecular Recognition of Methylated Amino Acids

and Peptides by Pillar[6]MaxQ. Org. Biomol. Chem. **2022**, 20, 7429–7438. https://doi.org/10.1039/d2ob01487d.

[19] Huskens, J. Multivalent Interactions at Interfaces. Curr. Opin. Chem. Biol. **2006**, 10, 537–543. https://doi.org/10.1016/j.cbpa.2006.09.007.

[20] Orlandini, M.; Pedrini, A.; Marchetti, D.; Li, Y.; Aragay, G.; Dalcanale, E.; Ballester, P.; Pinalli, R. Binding of Acetylated Lysine by Using a Water Soluble Aryl Extended Calix[4]Pyrrole. Chem. – Eur. J. **2024**, 30. https://doi.org/10.1002/chem.202303715.

[21] Ulusu, F.; Bilgic, A. Preparation of Pillar[5]Arene Functionalized Silica Gel Hybrid Material: Investigation of Biological (Antimicrobial, Antioxidant and Anti-Cancer) Properties. J Sol-Gel Sci Technol. **2025**,116, 290–302. https://doi.org/10.1007/s10971-024-06580-w.

[22] Bianchi, F.; Pinalli, R.; Ugozzoli, F.; Spera, S.; Careri, M.; Dalcanale, E. Cavitands as Superior Sorbents for Benzene Detection at Trace level. New J. Chem. **2003**, 27, 502–509. https://doi.org/10.1039/b210942e.

[23] Martínez-Edo, G.; Llinàs, M. C.; Borrós, S.; Sánchez-García, D. Isothiocyanate-Functionalized Mesoporous Silica Nanoparticles as Building Blocks for the Design of Nanovehicles with Optimized Drug Release Profile. Nanomaterials **2019**, 9, 1219. https://doi.org/10.3390/nano9091219.

[24] Ogoshi, T.; Yamagishi, T.; Nakamoto, Y. Pillar-Shaped Macrocyclic Hosts Pillar[n]Arenes: New Key Players for Supramolecular Chemistry. Chem. Rev. **2016**, 116, 7937–8002. https://doi.org/10.1021/acs.chemrev.5b00765.

[25] Shurpik, D. N.; Aleksandrova, Y. I.; Makhmutova, L. I.; Akhmedov, A. A.; Nazarova, A. A.; Lodochnikova, O. A.; Ivshin, K.; Kataeva, O. N.; Islamov, D. R.; Huang, F.; Stoikov, I. I. Supramolecular Self-Assembly of Monosubstituted Pillar[5]Arenes Under the Control of the Nature of

the Amide Moiety. ChemistrySelect **2025**, 10, e202405414. https://doi.org/10.1002/slct.202405414.

[26] Yakimova, L.; Filimonova, D.; Nazarova, A.; Stoikov, I. Synthesis and Characterization of New Monosubstituted Pillar[5]Arene with Terminal Carboxyl Group. Molbank **2025**, 2025, M2004. https://doi.org/10.3390/M2004.

[27] Wilson, C. R.; Puckett, A. O.; Murray, I. M.; Oliver, A. G.; Hof, F. Extended Sulfo-Pillar[6]Arenes — a New Host Family and Its Application in the Binding of Direct Oral Anticoagulants. J. Am. Chem. Soc. **2024**, 146, 28005–28013. https://doi.org/10.1021/jacs.4c03905.

[28] Ma, Y.; Chi, X.; Yan, X.; Liu, J.; Yao, Y.; Chen, W.; Huang, F.; Hou, J.-L. Per-Hydroxylated Pillar[6]Arene: Synthesis, X-Ray Crystal Structure, and Host–Guest Complexation. Org. Lett. **2012**, 14, 1532–1535. https://doi.org/10.1021/ol300263z.

[29] Liu, Y.; Bai, Y.; Zhang, J.; Li, Y.; Jiao, J.; Qi, X. Optimization of the Conditions for Copper-Mediated N-Arylation of Heteroarylamines. Eur. J. Org. Chem. **2007**, 2007, 6084–6088. https://doi.org/10.1002/ejoc.200700577.